DETECTION OF WEATHERING SIGNATURES USING UAV PHOTOGRAMMETRY IN COMPARISON WITH GROUND-BASED SENSORS.

ATINUKE ADEOTI FAKUNLE
MARCH, 2016

SUPERVISORS:
Dr. R. (Robert) Hack
Dr. N. (Norman) Kerle

DETECTION OF WEATHERING SIGNATURES USING UAV PHOTOGRAMMETRY IN COMPARISON WITH GROUND-BASED SENSORS.

ATINUKE ADEOTI FAKUNLE
Enschede, The Netherlands, March, 2016

Thesis submitted to the Faculty of Geo-Information Science and Earth Observation of the University of Twente in partial fulfilment of the requirements for the degree of Master of Science in Geo-information Science and Earth Observation.
Specialization: Applied Earth Sciences- Engineering Geology

SUPERVISORS:
Dr. R. (Robert) Hack
Dr. N. (Norman) Kerle

THESIS ASSESSMENT BOARD:
Professor, Dr. V.G. Jetten (Chair)
Dr. Ir. (Siefko) Slob (External examiner)

ABSTRACT

The description of the weathering state of a rock mass is very crucial in characterizing and classifying rocks during geotechnical investigations and engineering geological surveys. This process is very important because of the chemical and physical changes caused by the weathering process on the properties of the rock mass during its engineering lifetime, as well as the susceptibility of the rock mass to future weathering processes. Engineering geological field investigation has been a methodology greatly relied upon to carry out the acquisition of primary data, that helps provide information about the probable occurrence of weathering process on a rock mass surface and the degree to which the weathering has taken place. Since the application of ground-based remote sensing techniques and photogrammetric applications, it has enabled the automated approach to the detection of weathering signatures such as vegetation, organic matter, location and orientation of the discontinuities. Applications using Terrestrial laser scanners (TLS) have been applied in rock engineering for the detection of certain weathering signatures like the discontinuity geometry but the advent of Unmanned Aerial Vehicles (UAVs) in the geological field suggests a likely alternative to the use of TLS.

This research addresses the comparison in the application of UAV-based and TLS point cloud datasets in the detection of weathering on a rock mass. The result from the cloud to cloud comparative analysis shows that there is a good agreement between the UAV-based and TLS datasets, with discrepancies in the range of >1m for regions at the toe of the rock mass, and the vegetations at the edges of the rock mass not captured in the TLS data. Analyses carried out, with the excess green algorithm, the RGB values and the RANSAC shape detection, were used to extract the weathering signatures detected in the UAV-based and TLS datasets for the whole slope exposure, and segmented points from each geotechnical units extracted from the datasets.

The results suggests that the UAV-based and TLS point cloud datasets can be used to detect and extract weathering signatures such as vegetation and organic matter, oxidized regions, total organic carbon regions, and the orientation of the discontinuities present in whole exposed slope. Further analysis using the segmented points, extracted from each of the geotechnical units in the rock mass, showed results that are quite comparable in the UAV-based and TLS datasets. In addition to the detection and extraction of the weathering signatures mentioned earlier, the discontinuity spacings between the bedding planes in each of the geotechnical units were estimated, while discontinuity spacings between the joint sets in unit A and B were also estimated. Integration of the point cloud datasets with the thermal imagery showed a good contrast between the weathered and non-weathered surfaces, resulting from differences in their radiant capacity and chemical composition. This is supported by the emissivity and X-ray diffraction analysis carried out on the rock samples, from each of the geotechnical units.

This research shows that the UAV-based point cloud data was more optimal in the detection of weathering signatures, in comparison with the TLS point cloud data. This is due to the advantage of the possible application of the UAV-based images during analysis. However, from the assessment analysis, it can be inferred that the field investigation is still the most practicable, detailed and viable methodology in the detection of weathering process on a rock mass. Its major advantage is that it enables the weathering grade, strength and reduction of strength, and the condition of the discontinuities of the rock mass to be properly described using recognised and accepted standards.

Key words: *Weathering, Terrestrial laser scanner, UAV, Point cloud, Thermal images*

ACKNOWLEDGEMENTS

I express gratitude to the Dutch government through the Netherlands Fellowship Programme (NFP), for the opportunity granted to me to pursue my MSc study at the University of Twente, Faculty of Geo-Information Science and Earth Observation (ITC). My sincere gratitude also goes to my mentor, Dr. Adedayo Adeyemi for nominating me for this fellowship and ensuring I was granted the study leave without hesitation.

My sincere and profound gratitude goes to my supervisors Dr. H. R. G. K. Hack and Dr. N. Kerle for their encouragement, guidance, vivid and critical comments and provision of scientific direction towards my thesis. To all the experts for their contribution and help by giving feedbacks during the course of this study, I say a big thank you.

I am grateful to Mr Watse Siderius for his assistance with the Terrestrial Laser Scanner and thermal camera and also for providing valued assistance to make my field and laboratory work go seamlessly. I appreciate the insight into the possible expected results from the thermal camera provided by Dr. Chris Hecker. My appreciation also goes to Drs B D smith and Dr Caroline Lievens for their help during the laboratory work and critical advice on the results. My appreciation goes to the all the staff of AES and ESA departments, my colleagues and the ladies in student affairs, for all the support they gave me during my stay and stride to achieve this goal. I will also like to warmly appreciate my friend and colleague, Femi Ojambati, a PhD student at the University of Twente for his assistance with writing the Matlab code and critical arguments during my analysis, I am so grateful to you.

Special thanks go to my Mother: Mrs Oluseyi Fakunle and my siblings: Adedayo, Olubunmi and Itunu who had given me so much encouragement, support, love, joy and lots of laughter throughout my period of study. I am forever indebted to you.

Above all, I am most grateful and forever thankful to the Almighty God and my Lord, Jesus Christ for enabling me to successful complete the programme. I give Him all the glory for giving me the strength, understanding and knowledge to execute this research.

TABLE OF CONTENTS

LIST OF FIGURES

LIST OF TABLES

LIST OF SYMBOLS AND ABBREVIATIONS

ϱ	Density
2D	Two-dimensional
3D	Three-dimensional
C	Thermal capacity
DN	Digital Number
DTM	Digital Terrain Model
E	Emissivity
Eq.	Equation
ExG	Excess Green
i	Intensity
ICP	Iterative Closest Point
K	Thermal conductivity
LiDAR	Light detection and ranging
Matlab	MATrix LABoratory (a programming language for technical computing)
NAN	Not a Number
PCD	Point cloud data
PXRD	Powder X-ray diffractometer
SRM	Slope Rock Mass
SSPC	Slope stability probability classification
SWE	Weathering intensity parameter (used in SSPC) for the SRM
TLS	Terrestrial laser scan or Terrestrial laser scanner
TH9100Pro	Infrared Thermal Imager Thermo Tracer
TIR	Thermal infrared
UAV(s)	Unmanned Aerial Vehicle(s)
WE	Degree of weathering for the exposure rock mass (used in SSPC)
XRD	X-ray diffraction
XRF	X-Ray Fluorescence

1. INTRODUCTION

1.1. Background on the research

Weathering is a process that implies decay and causes changes in the parent rock as a result of external processes (Price et al., 2009). Weathering is the chemical and physical change of the soil or rock mass under the effect of prevailing physical, chemical, and biological processes (Tating et al., 2013). It causes weakening, loosening and crumbling of the soil or rock mass under the influence of the atmosphere and the hydrosphere weathering agents (such as local climate, surface and groundwater conditions, chemicals dissolved in groundwater) and through the exertion of stress on the rock creating discontinuities. The discontinuities, which is a collective term for the bedding planes, joints, fractures, fissures, faults, foliation (Ismael et al., 2014), will develop as the weathering process continues; and will eventually lead to pieces of the rock face falling away due to spalling process or the dissolution of the soil or rock mass. Thus, weathering can be said to be a process of continuous disintegration and decomposition of a soil or rock mass (Jain, 2014).

1.1.1. Weathering and its engineering significance

In industries such as civil engineering, mining, heritage conservation as well as urban-planning, weathering is seen as a preparatory stage for soil or rock mass denudation (Dearman, 1974). Hack & Price (1997) attributed future weathering after construction of a slope or engineering works as the main cause of soil or rock mass deterioration and failure of a slope during its engineering life-time. It influences the engineering behaviour of the soil or rock mass used as construction materials (Price et al., 2009). Weathering results in changes in the geotechnical parameters of a soil or rock mass; it decreases the strength and reduces the rock blocks and grains of the soil or rock mass (Hack, 2012) which leads to increased engineering costs, and impingement on the operational and safety aspects of the engineering construction (Hagen, 2012).

Chandler & Apted (1988) concluded that some of the problems faced in the effect of weathering in soil or rock mass are the reduction of the apparent degree of over-consolidation- this is related to the mechanical behaviour of the soil or sedimentary deposit exhibiting stiffness and rigid properties and increased strength due to the inter-particle bonding between the sediment particles packing them tightly together, a higher water content ratio in the weathered soil or rock mass, increase in the number of mechanical discontinuities, formation of new discontinuities in the rock mass and a reduction in the overall strength of the soil or rock mass. While Miščević & Vlastelica (2014) stated the problem of instability and reduction of the shear strength over the engineering lifetime should be considered for the stability and behaviour of excavations in soil or rock masses and their surroundings, behaviour of foundations in soil or rock masses, slopes excavated in rock bodies, especially when they are not protected against weathering processes. In order to guarantee the serviceability state and safe design for the whole engineering lifetime, it is important to determine and estimate the susceptibility of the geotechnical properties of the soil or rock mass to weathering processes (Price et al., 2009), which consequently makes it very significant to detect its occurrence.

In addition, the range of projects concerned with the field of rock engineering has expanded greatly with the increase in the development of underground power plants, missile launch, control facilities, tunnels, radioactive stations (such as nuclear power stations, radioactive material storage sites to mention but a few) and other types of protective structures (Deere & Miller, 1966; Likar et al., 2014). These infrastructure projects regularly require the monitoring of the soil or rock mass in which they are built to determine possible instabilities and assess hazards (Lato & Vöge, 2012). These infrastructure projects and works are constructed or occur close to the surface, and the process of weathering has been established to have a great influence and effect on most soil or rock masses at the surface and at shallow depth (Shrivastava, 2014) as well as great depth in extreme conditions. The engineering and geological problems related to the weathering process have persuaded the scientific community to better comprehend both the mechanisms and the features of the weathering process (Calcaterra & Parise, 2010).

Dearman (1974) mentioned that soil or rock mass as an engineering material displays extreme variation in its engineering properties, namely strength, permeability, thermal and structural features which is for a large part attributable to weathering. Thus, a description of the weathering state of a soil or rock mass is very important in characterizing and classifying engineering rocks during ground investigations and geological surveys because of its profound effect on the properties of the rock mass (BS 5930:1999, 1999; Matula, 1981). This description of the weathering state of a soil or rock mass is used to establish the degree and extent of weathering in the rock mass, with reference to established schemes (Bell, 1992a; BS 5930:1999, 1999; Dearman, 1974). This helps to determine the suitability of a project site for the construction of soil or rock related engineering works during site investigation. The British Standard (BS) 5930:1999 is an established and normative reference which contains the code of practice for site investigation. It is used as a guideline for the acceptable assessment of project site to ensure their suitability for the construction of engineering and building works; and for acquiring information about the characteristics of the project site that may affect the design, construction and durability of the project.

Weathering may be divided into physical (mechanical) and chemical weathering and some researchers also differentiate biological breakdown as a form of weathering; however, this involves the same processes as in physical and chemical weathering (Heckes et al., 1988). Although all materials are susceptible to weathering, there is variation in the rate of weathering, defined as the rate at which parent material is converted to weathering products and residuals (Phillips, 2005), which is dependent on the temperature, the amount of moisture, climatic condition and the relief (Bell, 1992b). The rate of weathering is further influenced by the interaction with erosion processes, which displace the weathered materials to reveal fresh soil or rock surface to advance the continuing interaction with atmospheric conditions (Antoine et al., 1995).

1.1.2. Detection of weathering process

The typical weathering signatures for physical weathering are the discontinuity geometry and the shear strength dependent on the condition of discontinuity. The discontinuity properties important in relation to weathering are namely discontinuity spacing, persistence, roughness (ISRM, 1978; Otoo, 2012), aperture, the presence and character of weathering products (or infill materials) and variation in the strength of intact soil or rock from fresh to weathered mass (BS 5930:1999, 1999; Tating, 2015). Also, the degree of color and discoloration of the soil or rock mass is a good weathering indicator. However, there are other proxy signatures, that is the presence of certain features, on the rock mass that give an indirect hint or suggestion that can be used as an indication of the likely occurrence of weathering on a rock mass.

The proxy weathering signatures to focus on for this study are the presence of vegetation and organic activities such as the algae, moss, lichens on the soil or rock mass; soil or rock texture (fine grained or coarse grained) due to the boundaries between the crystals of rock minerals forming lines of potential weakness in fine grained soil or rock mass causing it to often weather quicker than coarse grained soil or rock mass; temperature of the soil or rock mass face with respect to its radiant temperature and emissivity due to the likely increase in the emissivity and radiant temperature of the weathered rock mass in comparison to a fresh or newly exposed rock mass surface. It is also an influencing parameter for chemical weathering as it is an indication of changes in the composition of the soil or rock mass from fresh to weathered state. For chemical weathering, typical signatures include the presence of clay minerals which are likely to increase as the weathering process progresses in the soil or rock mass; presence of Magnetite & Hematite & increase abundance of defected pure Quartz due to re-crystallization of quartz with other minerals; presence of carbonate compounds and oxides of Ca, Na, Mg and K with likely reduction in their concentrations in the soil or rock mass as weathering progresses; and the presence of water on the rock mass and in the residue material, thereby creating an hydration or hydrolysis reaction with certain minerals in the soil or rock mass leading to the formation of clay minerals. Table 1-1 gives an overview of the observable parameters as indicators for the different types of weathering. The weathering signatures mentioned above can be detected using geologic field investigation and possibly remote sensing applications coupled with photogrammetric processes to extract information from images acquired.

Table 1-1: Type of weathering and the observable parameters also known as signatures.

Type of Weathering	Observable parameters	Literature Support
Physical -		
Mechanical discontinuities: These have been opened as a response to stress or weathering process.	**Discontinuities geometry** i.e. persistence, spacing of the discontinuities, and newly developed discontinuity sets.	(Ceryan, Tudes, & Ceryan, 2008; Tating, 2015)
	Condition of discontinuity i.e. aperture, weathering products (gravel, sand sized & fine debris particles), and roughness.	„
Occurring features: faults, fractures, fissures, joints, cracks, bedding planes.	**Strength of intact soil or rock mass**	(Hack, 2012)
	Change in color from the fresh to the weathered rock mass	(Bell, 1992b; Shrivastava, 2014)
peeling, flaking, crumbling, breakage under pressure.	**Rock texture**.	(Bell, 1992b)
	Vegetation & **Organic activities**	„
	Temperature	„
Chemical -		
Major faults on the rock mass (Normal, Thrust, strike-Slip) allow for the infiltration of water to a depth within the rock mass.	**Clay minerals**.	(Arikan & Aydin, 2012; Ceryan, 2012)
	Presence of Magnetite	„
	Presence of Hematite	„
	Presence of Quartz.	„
	Presence of Carbonate compounds and	„
	Oxides of Ca, Na, Mg and K	„
	Presence of Water and Moisture (on the rock mass not as a result of precipitation).	(Bell, 1992b)
	Temperature.	(Drever, 2005)

1.1.3. Geologic field investigation

Field study is a traditional method involving visual assessment, tactual, as well as direct and contact measurement with field instruments. It is a methodology greatly relied upon to carry out the acquisition of primary data that can be used to provide information about the occurrence of weathering processes on a soil or rock mass surface and the degree of weathering (ISRM, 1978). It is of great importance in research works carried out in the geological field to provide ground truth; this implies a reference field data collected to aid remote sensing image interpretation and also to verify the results acquired. For this study, the geologic field study was carried out to provide ground truth and the likely scale of detection (small scale ranging from 0-50mm, while large scale is >50mm) of weathering signatures present on the rock mass. It was used to grade the application of the ground-based sensor and UAV-based datasets to estimate which application is more optimal. Terrestrial field surveys, as observed by most researchers and professionals, have three major disadvantages in common. They are the occurrence of large errors often introduced due to sampling difficulties and human bias, difficulty in accessing part of the rock mass surface, and risk to human life due to hazardous terrain (Slob, Hack, Van Knapen, & Kemeny, 2004).

Other factors affecting geologic field investigation are cost of investigation, date lag and labour intensive (Everton & Diffin, 2004). They further stated that despite knowing the benefits of good quality field investigation, majority of the consultants felt they were frequently inadequate due to insufficient time mostly allocated to carry it out and thus omitted. Others, especially the geotechnical consultants, expressed concern about the recent trend of using single and very simple field investigation methods to save cost and optimize time constraints which has been discovered to have an effect on the sample quality and therefore accuracy of results, although it might likely be the only possible option in confined sites with limited or no access of large instruments.

1.1.4. Remote-sensing based application

Over the years, a wide range of remote-sensing techniques, which includes ground-based remote sensing such as with standard cameras, terrestrial laser scanner (TLS) to mention a few, have been established to detect and monitor the weathering process (Moses, Robinson, & Barlow, 2014). Slob, Hack, & Turner (2002) applied an automated approach to derive the discontinuity measurements of rock faces captured using a TLS. Squarzoni et al. (2008) made use of 3D terrestrial laser scanning (TLS) technique and infrared thermography to obtain information about the discontinuities geometry and time variation of heating and cooling on a rock mass surface. Terrestrial laser scanning and close-range terrestrial digital photogrammetry has been used to characterise discontinuities on rock cuts as well as survey and model rock discontinuities for linear outcrop inspection (Assali et al., 2014; Sturzenegger & Stead, 2009). The advances made in technology in the development of sensors and software applications have further facilitated the improvement of methods which enables rock surface weathering to be examined remotely and at much higher spatial resolutions than previously (Moses et al., 2014). Due to the hazards and uncertainties on the project site as a result of natural and man-made processes as well as the possibilities of overcome cost and time constraints, it has encouraged the application of remote sensing application using imagery from various sensors and over the years, it has become a recognized technique in the study of rock weathering (Franklin et al., 1988; Slob et al., 2005). There are quite a number of photogrammetric processes but this study focuses on the application of photogrammetry using ground-based sensors in comparison with the UAV-based imagery in detecting weathering signatures.

1.1.4.1. Ground-based sensors

The ground-based remote sensing is the application of a measurement system relatively close to the subject of study. The measurement system is typically hand-held or placed on a tripod (it can be placed on a vehicle too). Various ground-based sensors have been used in the study of rock mass weathering. Standard digital camera, TLS and thermal infrared sensors has provided possibilities of detection of physical weathering signatures while thermal infrared sensors, multispectral and hyperspectral sensors have been used in the detection of chemical weathering signatures. For this research work, the focus is on the application of TLS and thermal cameras. A major advantage of using ground-based sensors over the traditional method is the possibility of combination of basic photogrammetric techniques with other applications that allows the user to create 3D models and to obtain discontinuity information as well as slope degradation from exposed rock mass (Pollefeys et al., 2000).

Infrared Thermography (IRT) also known as thermal imaging is the application of thermal radiation to remotely determine the temperature of an object and its emissivity. It allows for the determination of the variations in temperature resulting from the amount of radiation emitted by the object of study which increases with temperature rise. IRT application can be used to monitor and measure inaccessible or hazardous areas. It is a non-destructive test method that helps maintain the integrity of the rock mass and its most important advantage is the application in determining variations and progressive changes in the object of study, due to changes in its composition. Thermal infrared radiation of an object is a property characterized by a certain wavelength in the electromagnetic spectrum related to the degree of emission from the object of study, due to the vibration of its molecules at a given temperature (Liew, 2001). Generally, it refers to the infrared range of the electromagnetic spectrum with wavelength between 3-20 micrometers(um) but in terrestrial remote sensing, the preferred infrared range between 8-14um (Gupta, 2003). Thermal imaging has been used in military, security and industrial applications and also there has been various applications in the geological research using standard consumer thermal cameras. Limitations in the application of IRT are the high expense to acquire and process acquired imageries, difficulty in the calibration of the thermal imaging system resulting from the unpredictable interactions with atmospheric moisture as well as restriction in its operational and technical parameters due to the weakness of the emitted radiation. The thermal images acquired can be difficult to interpret compared with other types of imagery but the application of false color helps.

In recent years, LiDAR data, which can be used to generate in real time the 3D topographic profile of the object of study and rendering of the rock mass face, has been further developed to utilize its advantages over the earlier ground-based techniques (Tonon & Kottenstette, 2006; Yan et al., 2015). Despite the significant benefits, LiDAR is not always the ideal tool (Beasy, 2015). As is the case for all point-cloud generation methods, TLS generates very high point cloud densities but the density reduces with increasing distance to the sensor. The TLS covers a relatively small area (Fritz et al., 2013), and likely to lead to the occlusion of the uppermost part of the rock mass depending on the height of the rock face. Furthermore, the imagery of the study area is still needed for clear interpretation of the point cloud data from the laser scanners. In rock engineering and design requiring steep slope information of high resolution, the accuracy of LiDAR data and the reach of the laser beam are found to diminish. Also, the point cloud collected are not intelligently placed, as they are placed at a constant regular interval which may not fall on the object of study, thus, entailing the possibility of data gap due to the spacing between the scanning beam as well as making it difficult to use to accurately map ridgelines and dense vegetation (Beasy, 2015). LiDAR technology is still very expensive to use for areas with no direct access such as a high steep slope, thus requiring the use of scaffoldings to enable measurements to be acquired of rock mass, and it entails specialized skill to process.

1.1.4.2. UAV-based photogrammetry

An alternative to TLS application may be the use of close-range photogrammetry with standard consumer digital camera mounted on Unmanned Aerial Vehicles (UAVs) platform. UAVs can be flown in areas where minimum ground disturbance is required, are capable of flying very close to the object of study to obtain very detailed images for inspections and surveys, and can be used to capture the study area in multiple perspectives with little or no occlusion (Helipix UAV, 2015). UAVs have a major advantage over other platforms; they can be deployed and landed at almost any location quickly and repeatedly and also manoeuvred into positions (Hackney & Clayton, 2015), even in very remote or small areas surrounded by rugged terrain or dangerous to the human life. This makes its application very valuable to infrastructure projects maintenance as well as rock mass surface monitoring and investigation. There is the possibility of generating a flight plan and carrying out image acquisition for autonomous flight operation. Manual flight operations can also be used in infrastructure (e.g., bridge) monitoring and acquiring the facade information of an object or area. There is the option of using a live view system to see what the drone sees, to acquire lots of metric information (such as location, speed, etc.) of the study area– all that is needed for a decent survey. The UAV platform can be equipped with other types of sensor system but this is with some limitations as the sensor system are not readily available and are expensive. Another advantage is that they require a simple methodology to process the images acquired (Rango et al., 2009). These images may then be used to generate 3D imagery of the rock surface, ortho-photographs for spectral analysis, or create digital terrain models through the application of Structure from Motion (SfM) and dense image matching photogrammetric techniques (Hackney & Clayton, 2015).

Although limited to military applications in the past, there has been a very high increase in the application of UAV platforms fitted with various sensor systems in different domains, one of which is the geological field and rock engineering (Blyenburgh, 1999). Application of UAV photogrammetry is not without its own disadvantages. There is a limitation in generating point cloud data for the base of the vegetation to gain a more detailed understanding of the terrain below. There is a restriction on the size of sensor that can be placed on the UAV platform due to its payload limitations requiring the use of low weight navigation units, which implies less accurate results for the orientation of the sensors. But, with the increasing advancement in technology, there is a high possibility of eliminating this limitation. Presently, in many countries including the Netherlands and Nigeria, it is illegal to fly UAVs without proper documentation and licensing from the government. UAVs are dependent on the skill of the pilot to detect and follow the orientation of the UAV- system and this is the basic reason there needs to be a well-trained pilot, due to security issues. They are not equipped with collision avoidance systems, like manned aircrafts. Also important to note is that UAVs cannot react like human beings (in a manned aircraft) in unexpected situations, e.g. unexpected appearance of an obstacle, thus the pilot needs to be alert and monitor the flight during data acquisition.

1.2. Problem statement

There are existing limitations in the application of ground-based sensors to detect some of the weathering features and overcome the problem of occlusion of the rock mass face leading to loss of information about the upper part of the rock mass. The TLS data shows the possibility of 3D model of the point cloud but lacks information about the texture and color properties of weathered rock mass. Also, it is difficult to detect the presence of organic activities such as moss, lichen on the rock mass face which are proxies for the occurrence of weathering process. For the thermal camera, many models do not provide the irradiance measurements used to construct the output image, the loss of this information (such as emissivity, distance, ambient temperature and relative humidity) lead to the fact that the resultant images are inherently incorrect measurements of temperature. There is the possibility of differing emissivities of the object of study expected to exhibit a specific value and also influence of reflections from other surfaces. However, a combination of the two approaches will likely provide better detection of the weather signatures. Presently, the utility of UAV photogrammetry to detect weathering processes on a rock mass is still to be demonstrated. From literature, it shows the ability to provide spectral, texture and 3D model of the point clouds. It is therefore necessary to provide support for the application of UAV photogrammetry as an alternative for ground-based sensors. For this, the UAV-based data has been contrasted with the data from the ground-based sensors to detect and assess the weathering signatures on the rock mass. This is important to assess which application is the more optimal process for detecting weathering signatures.

1.3. Research objectives and questions

This research work addresses the following main and specific objectives using the research questions.

1.3.1. Main objective

To compare the application of ground-based sensors, TLS and thermal camera, and UAV-based photogrammetry in detecting rock mass weathering.

1.3.2. Specific objectives

1. To assess which weathering signatures can best be detected from the UAV-based data and the ground-based sensor, TLS.
2. To determine how well the weathering signatures can be detected by combining the UAV-based and TLS data with other sensors, e.g. thermal camera.

3. To develop a comparative scoring scale to evaluate the ground-based and UAV- based photogrammetry in the detection of weathering signatures.

1.3.3. Research questions

1. What is the degree of variation between the UAV-based and TLS 3D point cloud datasets?
2. How to assess the detectability of the weathering signatures from the UAV-based image and the ground-based sensor?
   - What are the weathering signatures that can be detected using the UAV-based or TLS data or both?
   - What are the possibilities of measuring the weathering signatures using the UAV-based or TLS data or both?
   - What is the effect of occlusion on the degree of weathering information detected using the UAV-based and TLS data?
3. What are the possibilities of improving the limitation of UAV- based and TLS sensor by correcting with additional data from the thermal camera sensor?
   - How can it improve the detectability of the weathering signatures?
4. How can the rate of weathering on a rock mass be assessed and estimated using ground-based, TLS and UAV- based data?

1.4. Datasets and study area

The major components of the research are image-based data acquired with a UAV system and ground-based sensors, terrestrial laser scanner data and thermal camera. Pix4DMapper and RiSCAN PRO software was used to generate point clouds from the UAV-based images and the TLS data using automatic processing. Cloud compare software was used to carry the detailed quality assessment of the point clouds generated from the UAV data using the TLS as a reference data. Image processing techniques was used to detect the weathering signatures from the UAV based and TLS point clouds. The data collection was carried out in Germany, where the law is less strict with regards to the UAVs flight. The study area was at the Quarry Gildehaus, Bad Bentheim, Germany, with a sedimentary sandstone rock mass outcrop of very fine grains, commonly known as the Bentheim sandstone. Its use as a construction stone spanning a long period and it has been known to be subject to the effects of weathering process (Dubelaaret al., (2015).

1.5. Thesis structure

This research study has the following structure -
Chapter one: Introduction - contains a brief background on the weathering process and the sensor systems to be used for its detection, the research problem to be addressed by this study and the research objectives and questions to be used, and a brief description of the study area.
Chapter two: Literature review - covers a more detailed description of the weathering signatures as well as the methods used in the detection of weathering process.
Chapter three: Description of the study area- contains a summary of the study area, the geological setting and a description of the studied slope.
Chapter four: Methodology - contains the designed approach adopted in this study to achieved the research objectives.
Chapter five: Results and Discussions - the results contains the findings and outcomes obtained from executing this study as well as the discussion of the results according to whether the purpose of the application of the methodology was accomplished or not, noting the limitations in the applications.
Chapter six: Conclusion and recommendations - contains a brief conclusion of the study and presentation of answers to the research questions. The recommendation section outlines possible research opportunities.

2. LITERATURE REVIEW

2.1. Weathering process

Weathering is a significant (Deere & Miller, 1966; Arikan & Aydin, 2012), crucial and fundamental process with diverse facets that has varying implications for a wide range of earth and engineering works (Patton & Deere, 1970; Saliu & Lawal, 2014). It is a process that occurs from the surface of the exposure of the soil or rock mass and also from the surface of discontinuities before penetrating the rock inside with time. Depending on the nature and composition of the rock mass, the weathering process can be very quick or very slow to occur or cause significant alteration of the rock mass (Schieber, 2007). Weathering affects the intact rock and also the discontinuities in the rock mass (Gupta & Rao, 2001).

- Intact rock (also known as rock material) is the cemented assemblage of mineral particles that form rock blocks between the discontinuities in a rock mass.
- Discontinuities referred to as the plane of weakness in the rock mass are the structural features (such as bedding planes, joints, fractures, fissures, faults, foliation) that separate the intact rocks within the rock mass.
- Soil mass refers to a natural occurring body consisting of layers or horizons of organic constituents of variable thicknesses, which may differ from the parent materials in their morphological, physical, chemical, and mineralogical properties and their biological characteristics (Joffe, 1949, modified by Birkeland, 1999).
- Rock mass is the in-situ rock rendered discontinuous by the structural features and failure within the rock mass is usually related to movement and loss of strength along the discontinuity surfaces. In this study, rock mass is used to refer to both the soil and ground mass, and also taken to mean both the intact rock as well as the network of discontinuities and weathered products (Hoek & Bray, 1981). ISO (2003) describes a rock mass as "rock together with its discontinuities and weathering profile". This is supported by Tating (2015) who defines a rock mass as consisting of a collection of rock blocks divided by various sets of discontinuities.

Weathering is defined as the gradual deterioration of a rock mass under surface conditions causing an alteration in the color, texture, composition or structure of the parent material. Dearman (1974) and Norbury et al. (1995) defined weathering as the process of alteration and breakdown of rock mass under the direct influence of the hydrosphere and the atmosphere at and near the Earth's surface by chemical decomposition and physical disintegration. Mackenzie & Fred (2006) define it as the processes occurring in any natural material whether soil or rock when in contact with the atmosphere and hydrosphere. Hack (1998) defines weathering as the in-situ breakdown of rock masses due to physical and chemical processes under the influence of atmospheric and hydrospheric factors. Hack & Price (1997) defines weathering as the process that causes the disintegration and decomposition of rock mass leading to the formation of residual soils which control surface morphology. While Price (1995) defined weathering as "the irreversible response of rock materials and masses to their natural or artificial exposure to the near-surface geomorphologic or engineering environment". This implies that weathering affects the durability and reliability of the rock mass during engineering works thus, the susceptibility of rock mass to weathering is of considerable importance in engineering (Dearman, 1974; Mohamed et al., 2007).

2.1.1. Physical weathering

Physical (also known as mechanical) weathering is generally defined as the disintegration and breaking apart of a rock mass with little or without any change in the original chemical composition and mineralogy of the rock mass. It occurs due to the influence of pressure and temperature fluctuation on the rock mass causing pressure changes within the rock mass as a result of the continuous expansion and contraction of the rock mass. Physical weathering leads to the creation of discontinuities and causes propagation of discontinuities into the ground mass, and it progressively breaks down the parent rock mass into residual material (Arikan & Aydin, 2012). It has the following four main forms of occurrence:

(i) Freeze-thaw (frost wedging) weathering - this occurs from the continual seepage of water into the discontinuities in the rock mass, which freezes and causes expansion with sufficient tensile stresses capable of fracturing the intact rock mass. Several cycles of freeze and thawing will eventually break the rock apart;
(ii) Wetting-Drying (slaking) weathering - occurs through the varying accumulation of water between the mineral grains of a rock mass. This results in the swelling and shrinkage of the mineral grains causing the rock material to fall apart in time (Day, 1994);
(iii) Thermal expansion and contraction (insolation) weathering - this occurs as a result of rapid heating and cooling of the rock mass which may cause cracking;
(iv) Exfoliation (spalling) - occurs as the development of cracks and opening of existing discontinuity which is a consequence of the increase and reduction of stress relief within the rock mass. This variation in stress relief can be triggered by the repeated heating and cooling, causing the outer surface of the rock to peel and flake away from the main rock mass.

2.1.2. Chemical weathering

Chemical weathering is the weakening and decomposition of a rock mass resulting in alteration of its chemical and mineralogical composition. It occurs mostly under the influence of water present and substances that have dissolved in it reacting with the mineral compounds of the groundmass to form new minerals such as clays and salts (Arikan & Aydin, 2012). There are different forms of chemical weathering but they generally involve three processes (Cowan & Huntington, 2011):

(i) Dissolution / Carbonation - occurs as a result of water mixing with carbon dioxide in the air to form carbonic acid, also known as acidic rainwater. This reacts with the minerals making up the rock composition, thereby dissolving them;
(ii) Hydration / Hydrolysis - occurs due to the capacity of the rock minerals to take up water. It is a result of water ionizing and reacting with the minerals making up the rock mass and breaking them down to form clay, soluble salts and causing surface flaking of the rock mass surface;
(iii) Oxidation - also known as rusting, is simply the breakdown of the rock mass by the presence of oxygen and water. It involves the reaction of certain metals with oxygen allowing the removal of an electron from the ion of the metal leading to the formation of very weak rocks (Price, 1995).

2.1.3. Biological weathering

Biological processes cause physical and chemical weathering (Gifford, 2005), but some literature distinguish biological weathering as a separate process. Biological weathering occurs as a result of the presence of vegetation through root wedging, production of organic acids (such as humic acid) and compounds (such as carbon dioxide reacting with water to form weak acid) from some organisms that enhance chemical weathering, and to lesser extent by animal activities. It is the weakening and subsequent disintegration of rock by plants, animals and microbes. Growing plant roots can exert stress or pressure on rock sufficient to break it apart and some certain species of lichens have been discovered to cause the inducing and acceleration of weathering process by dissolution and precipitation of secondary carbonates and oxides (Jie & Blume, 2002; Meunier et al., 2014). Although this weathering process can be categorised under the physical weathering, the pressure is exerted on the rock mass by a biological process.

2.2. Weathering process in a rock mass

2.2.1. Rock lithology and weathering

Turkington et al. (2005) mentioned that rock mass weathering is controlled by the rock lithology and structure. The weathering rate varies due to the geological complexity of the rock body as a result of different lithology and structure, which differ in terms of origin, that makes up the rock mass. Each lithological unit react differently to the local conditions on exposure to the surrounding environment, and will probably have rock material properties controlled by varying mineral composition, texture, fabric and the weathering state due to their formation at varying temperatures and pressure (Irfan, 1996). As a result of the conditions subjected to during formation and subsequent history, various rock types and their alteration products have inherently different weaknesses and strengths. The important aspect of rock characteristic is its natural inter-particle bonding and the strength of constituent minerals assemblage (Savanick & Johnson, 1974). A rock mass cannot be generally assumed as being strong if the bond between mineral constituent assemblages is weak. The inter-particle bonding between the rock material influences its susceptibility to weathering.

2.2.2. Rock mass susceptibility to weathering

In accordance to the rule of thumb, chemical weathering is more important in warm moist regions, whereas physical weathering is more important in cold dry areas. The susceptibility of a rock mass to weathering is mostly dependent on its composition as well as the prevailing environmental conditions, and mostly especially on the dissolution of carbonates, salts and sulphates of certain minerals (such as gypsum) and the clay content in the rock mass, thus in general, the more clayey the rock, the greater is its susceptibility to the weathering process. An illustration (see Figure 2-1) can be given of a shale and sandstones in an inter-layered rock mass exposure, where the shale is considered more susceptible than sandstone. There will be possibility of differential form of weathering occurring on such an exposure, as the weathering in shale region would be more than that of the sandstone layer in the rock mass (Hack, 1998). Susceptibility to weathering of newly exposed rock masses from engineering works or man-made slopes are further increased; this is because they are subject to accelerated deterioration as a result of release of confining pressure or stress relief, and general disruption of the equilibrium state which leads to intensified weathering right after excavation (Hack & Price, 1997; Huisman, 2006).

(a) 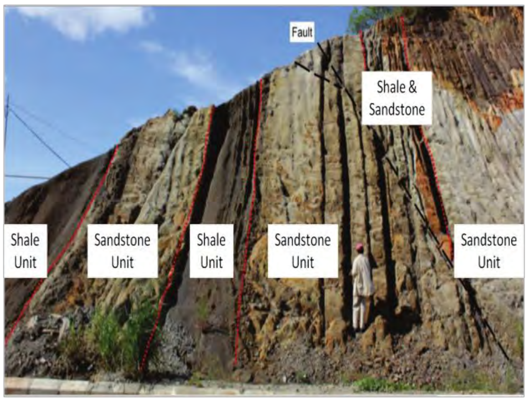

(b) 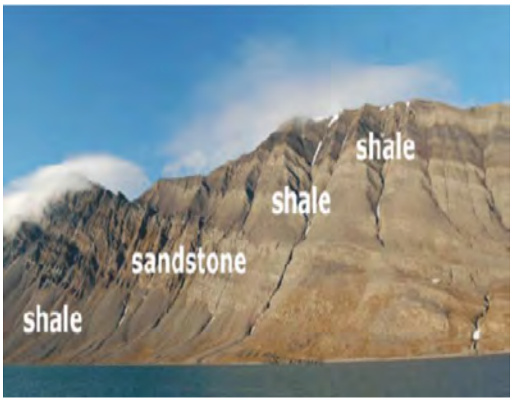

Figure 2-1: Rock mass exposure with interlaid sandstone and shale units.
Source- (a) modified after Tating, 2015; (b) after Jenssen, 2007

2.2.3. Influence of stress relief on rock mass weathering

During engineering works, applied load or a cut in the rock mass causes a change in stress regime within the rock mass. The variations in the stress regime of a rock mass influences the development of new discontinuities occurring as a result of stress increase and change in stress concentration while the occurrence of further opening of existing discontinuities present in the rock mass is related to the stress reduction (Tating, 2015; Miščević & Vlastelica, 2014). The development of the new and existing discontinuities creates room for an increased seepage of water into and flowing through the rock mass, plant roots to reach a larger area of the rock mass as well as the presence of organic matter which speeds up and increases the process of physical weathering and enables deeper penetration of chemical weathering effects on a rock mass (Huisman, 2006).

2.2.4. Rock mass weathering

For most naturally occurring rock masses, usually not all parts of the rock blocks are exposed to the atmosphere, mostly just part of the rock block if it is on the outside of an exposure. The deterioration and weathering in the rock mass cause by exposure to the atmosphere is usually transferred through other rock blocks and through the various network of discontinuities by water or air to a deeper depth of the rock mass. These have adverse effects on the rock strength, the shear strength along discontinuities and the spacing of the discontinuities. Weathering rate has been found to be reduced in a rock mass with the weathered products and residue staying on the surface of the rock mass. These have been discovered to protect the rock mass underlying the weathering residue. However, weathering process is expected to start again with a weathering rate comparable to the weathering rate of the original material when erosion processes remove the weathered residue (Tating, 2015).

The influence of weathering on a rock mass is usually first observable at the surface. In the subsurface, it is observed that the weathering processes are quite different from those at exposure on the surface of the rock mass. Mostly the weathering in the subsurface is governed by the influence of chemical weathering with the effect of physical weathering almost negligible. A rock mass surface exposed to the direct influence of atmospheric conditions, is mostly influenced by the physical weathering with a strong effect of stress relief, but generally it is subject to a combination of chemical and physical weathering (Tating et al., 2013). Although many studies have been conducted on the detection of weathering at surface, it is still mostly impossible to determine weathering in the subsurface without first carrying out an excavation process. There are the possibilities of core drills but these normally have small diameters and give limited information, or trenches but they can only be made to a limited depth. There will be difficulty in acquiring undisturbed sample using core drilling method due to the wearing effect of the drilling process or water as it comes into contact with the sample (Miščević & Vlastelica, 2014). Also, most rock mass weathering does not propagate in a uniform manner due to the variation in topography, quantity of discontinuities and drainage of moisture into the rock mass (St Clair et al., 2015), detailed investigation needs to be carried out since reported cases indicates the possibility of weathered rock at the surface and also to be found beneath the un-weathered rock mass. Thus, there is need to understand the indicators of the weathering process to be able to infer the classification characteristics of a rock mass at surface to larger depth.

Campbell & Claridge (1987) and Bockheim (2015) mention proposed weathering indicators that can be used to characterize the rock mass surface as follows;

a. The degree of oxidation and staining within the profile,
b. Development of horizons of salt accumulation,
c. Varying texture and colour along horizons,
d. Varying rock strength within the profile
e. Differences in consistence within the profile exhibited by the formation of fissures, joints or cracks (Sara, 2003), and
f. In the most favourable environments, accumulation of vegetation and organic matter.

2.2.5. Rock mass weathering signatures (indicators)

From the discussions above, it can be derived that a major and important observable parameter to be assessed for engineering construction in and on a rock mass is the "discontinuities". There are two basic types of discontinuities namely mechanical and integral (Price et al., 2009). Integral discontinuities are yet to be opened by movement or weathering and have the same shear strength as the surrounding rock materials without affecting the intact rock strength. They can change into mechanical discontinuities due to weathering processes that change the characteristics of the discontinuity, while mechanical discontinuities have been opened by movement, stress or weathering. They are the planes of weakness where the shear strength is significantly lower than the surrounding rock material. For this study, the focus is on mechanical discontinuities. These discontinuities (comprising of fractures, faults, joints, bedding planes, cracks and blasting cracks) are what determine the overall block characteristics and help to control the mechanical behaviour of a rock mass (Tating et al., 2014). With reference to ISRM (1978), Otoo (2012) Price (2015) among others,

(i) Fault- is described as a plane of a shear failure that exhibits clear signs of differential movement or recognisable displacement of the rock mass on either sides of the plane.
(ii) Joint- is a crack either planar, curved or irregular across which the rock has little tensile strength. It may be open and filled with air or water, or by soil residue and rock fragments which act as a cement.
(iii) Fracture- is defined as a discrete break in a rock to describe the cracks generated during rock material testing, blasting and brittle rock failure.
(iv) Bedding- is a surface created by a change in factors such as grain size, grain orientation and mineralogy during the deposition process of a sedimentary rock. It forms some of the most extensive discontinuities in a sedimentary rock mass and generally run parallel to one another.

From numerous studies carried out, weathering processes have been found to affect the number of discontinuities in a rock mass, the geometry and shear strength of the discontinuities and its geotechnical characteristics. The effects of weathering on discontinuities in and on a rock mass if properly understood can help improve the ability to better forecast the future geo-mechanical characteristics of the rock mass. These can be implemented into the design of structures in or on rock masses such that the structure will remain stable and serviceable over the full designed expected lifetime or allow for the application of suitable remedial measures to overcome adverse performance. This is very important especially in the case of finer-grained, sand-sized rock masses, whereby significant deterioration due to the rapid formation of mechanical discontinuities can occur within a period of weeks or months after excavation and engineering works. The features of a discontinuity geometry influenced by the weathering process are the spacing, persistence while that of the condition of discontinuity are surface roughness of the discontinuity walls, aperture, and the presence and type of weathering infill material or weathered product. According to ISRM (1978), Matula (1981), Price et al., (2009)and Tating (2015) among others (see Figure 2-2),

(i) Discontinuity spacing- is defined as the perpendicular distance between two adjacent discontinuities that belong to the same discontinuity set.
(ii) Persistence- is the extent of a discontinuity from its inception to its termination in the intact rock or against another discontinuity. It is the measure of the continuous length of the discontinuity.
(iii) Roughness- refers to the degree of irregularity of the discontinuity surface.
(iv) Aperture- is the perpendicular distance between adjacent rock walls of an open discontinuity, in which the intervening space is air or water filled.
(v) Weathering infill material or weathered products- refers to the material separating the walls of the discontinuity as well as the residual soil and debris at the bottom of the rock mass.
(vi) Discontinuity set- A set denotes a series of discontinuities with the same geological origin, orientation and mechanical characteristics (friction angle, roughness, infill material etc.) on the

rock mass including the same weathering degree and discontinuity patterns are broadly grouped as a geotechnical unit (Hack, 2006), otherwise it is a single discontinuity.

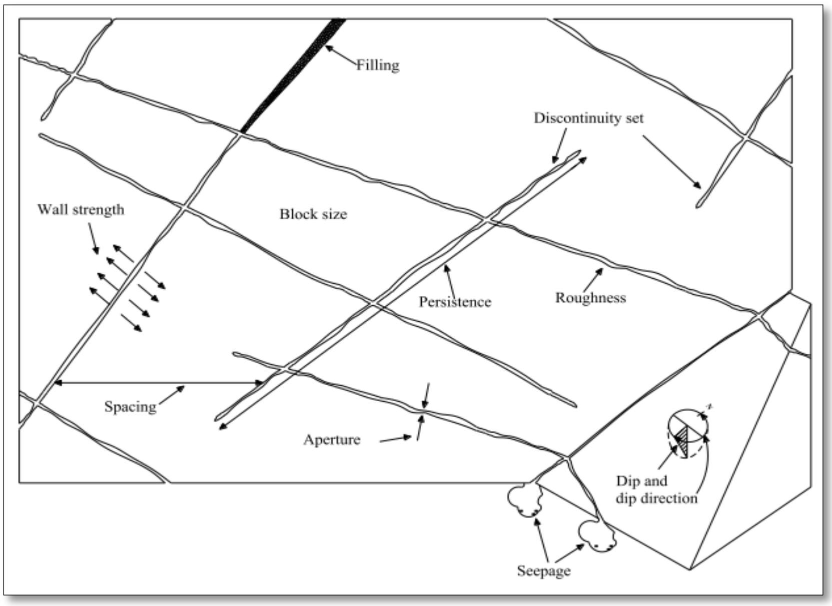

Figure 2-2: Schematic drawing of a rock mass illustrating the properties of discontinuities
Source- Modified after Hudson, 1989 cited in Otoo, 2012.

Various studies carried out have indicated that rock mass exposed to the atmospheric conditions exhibit a weathered surface whose colour and spectral properties differ from fresh bare rock mass surfaces. The surface texture of a rock mass and the various stages of the weathering products have been used to estimate the rate of weathering and to date lava flows of the same chemical and mineralogical composition using thermal infrared imagery (Kahle et al, 1988; Abrams et al, 1991 cited in Riaza et al., 2001). O'Neill (1994) mentioned that the presence of lichens, algae, moss and organisms cover on weathered rock surfaces. This is supported by Campbell & Claridge (1987) who stated that lichens and vegetation were found only on rock surfaces that has been exposed to weathering processes, and further went to state that lichens and vegetation cannot grow on fresh bare rock mass until it is sufficiently weathered. Butcher et al. (1992) remarked that lichens and organic matters are effective agents during the process of physical and chemical weathering. They stated that chemical weathering is more prominent in regions where there is much vegetation and it tends to increase the pores in the rock mass. They mentioned that two important classes of minerals, the silicates and the carbonates release alkali, namely Na^{+} and K^{+}, and alkaline earth cations, namely Ca^{2+} and Mg^{2+} during weathering process, there is also the synthesis of new clay and oxide minerals . The presence of these minerals and their released alkaline constituent as well as certain elements are sources used to detect ongoing and weathered rock masses. They further mentioned that though subtle, there is the influence of temperature variation on both physical and chemical weathering especially chemical weathering where it is seen to have a direct effect on the weathering rate.

2.2.6. Effect of weathering process on the weathering signatures

According to Price et al., (2009), weathering is seen to begin on the discontinuities that transmit water. They stated that the progression of the weathering process on the rock mass increases the number of discontinuities and the overall length of the persistence. This in turn, increases the susceptibility of the rock mass to slope instability and slide. They indicated that the surfaces of mechanical discontinuities may be smooth or exhibit varying degrees of roughness, but the effect of weathering on roughness is to reduce the degree of inherent surface waviness and undulation relative to the discontinuity. Weathering process influences the aperture of discontinuities by causing further opening of the discontinuities in the rock mass as a result of stress relief or plant root wedging. This creates room for the openings to be filled with weathering products such as clay or salt solution or debris from erosional processes. The weathering products consist of different types of material dependent on the type of weathering process. For physical weathering, the weathering products are rock fragments, residual soil materials, and debris at the base of the rock while for chemical weathering, the weathering products are new minerals, residual soil materials and salts in solution. The spacing of the discontinuities and bedding plane does not reflect the thickness of the geotechnical layers any longer due to the opening of the bedding planes by weathering process (Hack, 1998). This affects the shape and size of the rock blocks dependent on the spacing of the discontinuities holding them together. Weathering process causes a continuous reduction in the rock block size.

Colour variation is one of the primary indication of weathering. Thus, changes in the color of the fresh rock mass to the weathered rock mass surface is one of the likely obvious sign of weathering. A freshly cut rock mass surface will have a lighter and brighter color than a weathered surface. The most common is the brown staining by the oxidation of iron bearing minerals. This is supported by Fell et al. (2014), who stated that weathered rocks are usually yellow-brown or brown in color due to oxidation. He further stated that the deposition of certain minerals relating to the terrain and relief of the rock mass can be a good indicator for the occurrence of weathering. An example was given of iron oxide minerals having been leached out from one zone to produce weaker porous rock mass and re-deposited in another zone producing a stronger denser rock mass which in some cases is stronger than the fresh rock mass.

Another variable affecting the progress of weathering and to be used as an indicator for weathering is rock texture. Riaza et al. (2001) mentioned that fine-grained rocks are more susceptible to chemical weathering as a result of moisture attack than coarse-grained rocks when visualized. They stated that coarse rock textures, which will produce large grain sizes, are most likely to have low overall reflectance in a remote sensing imagery than fine-grained rocks. Thus an increase in the composition of fine-grained clays of the weathering product will result in increasing the overall reflectance. Butcher et al. (1992) remarked that plants and vegetation grow roots in rock crevices which eventually increased the pressure enough to break the rock mass apart. Also, the vegetation cause fracture, roughening and grinding down of individual grains or minerals in the rock mass. It is noted that as weathering increases, the growth of lichens and vegetation also increases on the rock mass.

The dark-coloured weathered region of a rock mass surface, as a result of changes to the composition of the parent rock mass as well as the presence of certain weathered products, will absorb and heat up rapidly causing it to have high surface temperature, thus emitting higher energy while a light-coloured fresh surface, with its low heat absorption, will emit low energy. Due to the high absorption of heat energy, a dark-coloured weathered surface is likely to fracture more easily as a result of thermal stresses (Clark and Small, 1982 cited in Hall et al., 2005). They also mentioned that absolute surface temperatures (alternatively known as the radiant temperature) are controlled by the density of the rock mass. A dense fresh rock mass with low porosity will have low temperature as it will require a longer period to heat up, while a less dense weathered rock mass with high pore space will have a higher temperature (Gupta, 2003). Alternatively, due to the dense packing of the grains in a fresh rock mass, it requires conduction for the heat to be transmitted from one heated grain to the other all through the rock mass, while a weathered rock mass, that is much less dense and filled with pores requires a convection process for heat transfer all through the rock mass. This process is much faster as it is aided by the presence of the air molecules between the grains always in constant movement, thus the weathered rock mass quickly heats up but also quickly losses it heat energy once the source is removed. Lastly, with increase in the moisture content of a rock mass, the greater the absorption & emission since it takes a longer time for the rock mass to heat up and to cool.

2.2.7. Weathering process in sandstone rock mass

The studies of weathering process in sandstone rock mass have been focused on the physical breakdown, with interest in the role of thermal expansion and contraction (insolation) temperature changes on the rock mass surfaces (Turkington & Paradise, 2005). They elucidated that sandstone rock mass shows significant moisture expansion because of the presence of active porosities within the rock mass of up to 35% by volume and high saturation coefficients, and that the thermal expansion in the rock mass is also significant in causing sandstone decay exhibiting a coefficient of volumetric expansion of 0.36 between 20 and 100^{O}C. McGreevy (1985) indicated that the surface temperatures and thermal gradients created by thermal expansion and contraction depend on the thermal characteristics of the rock and promotes micro-fracturing of surface grains.

Kumar & Kumar (1999) mentioned the effect of biotic contact on sandstone rock mass has been of great interest because it results to occurrence of bio-deterioration. They further explained that activities of living organisms has been viewed as deleterious on sandstone rock mass surfaces with attention focused on lower-order plants; this is a collective term used for plants such as mosses, liverworts and lichens which do not have roots and produce spores to reproduce, rather than flowers. In sandstone rock mass weathering, the effects of living organisms has been mentioned to promote salt and frost attack by increasing the pore volume and moisture content of the rock mass, cause the precipitation of the sulphates and oxalates minerals, as well as mineral alteration and alteration of the thermal characteristics and wetting times of rock mass.

2.3. Classification of weathered rock mass

Rock mass can be classified based on its degree of weathering and the main purpose of a rock mass classification scheme for engineering purposes is to provide the engineer with a qualitative information about the rock mass. Fell et al. (2014) mentioned that rock mass classification is used to provide a short-hand descriptions of the rock mass at different recognisable stages of change due to effect of the weathering process. They stated that it assists the site investigator in making sound correlations and predictions about the distribution of rocks in various weathered conditions of other part of the project site not directly explored. They further stated that it is a means of enabling unambiguous communication of the description of a rock mass. According to the Geological Society Engineering Group Working Party Report (Norbury et al., 1995), a conclusion was reached that no single classification scheme can encompass the complexity of weathering, all rock types nor can classification be made based on a single material attribute.

2.3.1.1. The British Standard (BS) 5930:1999 and ISO 14689-1:2003

One of the most commonly used weathering classification is the BS5930:1981 for rock mass classification schemes. Due to its being regarded as overly simplistic and inappropriate by many researchers, who further went to say that the classification scheme does not work well in practice and conflicts with other well-established classifications (Hencher, 2008). He also mentioned that the BS5930:1981 classification scheme lacks weathering classification on intact weathered rock samples. Meanwhile, it is supposed to be used in the geotechnical logging of boreholes. A revised version of the BS5930:1981 was developed to incorporate the weathering classification scheme. The new version namely BS5930:1999 consists of five different classification approaches that cover both uniform and heterogeneous materials, which makes it compatible with other schemes as any of the classification approaches can be used to suit the object of study.

The ISO 14689-1:2003 weathering classification scheme differentiated between the intact rock and rock masses. Although it adopted the BS5930:1981 weathering classification, modification was carried out for the notation of the weathering grades. An illustration of the modification carried out in this classification scheme is that the fresh rock which is noted as I in BS5930 is assigned a grade of 0 and the residual soil, which is noted as V in BS5930 is assigned a grade of 5. This modification was noted in the critique report carried out by Steve Hencher as not being very helpful and usable in practice (Hencher, 2008). He also mentioned that the adjustment of the weathering grade notation only presents more confusion for the users due to lack of standard uniformity.

For this study, Approaches 1 and 2 of the weathering classification scheme in BS5930:1999 in relation with the BS5930:1981 will be made use of, which is also in relation to the recommendation of the ISO 14689-1:2003 for rock mass classification systems using one or more descriptive parameters to suggest likely rock mass behaviour and classification as opposed to using just a single classification scheme, which does not give a good overview of the weathering classification.

2.4. Applications for the detection of weathering process in a rock mass

2.4.1. Application of geologic field investigation methods to detect weathering

Geologic field investigation differs from the ground-based remote sensing because of the application of direct and contact method with the object of study. This usually involves the use of visual observation, tactual, hand-held and contact instruments such as geological or Schmidt hammer, geological compass-clinometers, measuring tape, roughness profile-gauge, traversing micro-erosion meter for direct measurement (Reid & Harrison, 2000) on the rock mass. These tools are quite effective, but errors are introduced in their application as a result of human bias from either over or underestimation in the measurement (Hack, 1998; Slob et al., 2005). Currey (1977) mentioned the application of visual observations during field investigation to provide a qualitative information about the mechanisms of rock weathering. Herget (1982) cited in Palmström (1995) recommends the use of visual observation and suggested the assessment of the rock strength using simple hardness tests in the field with a geological or rebound hammer, as a rock mass in its fresh state is likely to be more stronger than when weathered. McCarroll (1990) cited in White, Bryant, & Drake (1998) recommended the use of a micro-roughness meter to estimate the surface roughness of a rock mass surface caused by uneven weathering by measuring the micro-relief at a horizontal spacing of 1mm along a 100 mm transect. Piteau (1970) cited in Palmström (1995) described a procedure using a straight edge placed across the discontinuity surface to measure the maximum amplitude and the length of the joint. The values of which are inputted into a standard formula to estimate the small scale roughness of the discontinuity surface. Palmström (1995) stated the touching with the fingers to the rock mass surface to determine the roughness of the discontinuity, and comparing with a reference surface of known roughness such as a sand paper using a standard description and classification scheme. He also suggested the use of geological compass-clinometers and measuring tape to derive a crude estimate of the dip and dip-direction of the discontinuities as well as the joint lengths, referencing a classification and characterization system. Slob et al., (2007) also remarked on the use of compass and inclinometer, and documentation by recording information on a notebook as well as photographing with a camera to map fractures at rock faces. The use of the spectrograph, X-ray diffraction and fluorescence, and photoelectron techniques was applied in determining the mineralogy of the weathered rock mass in comparison to its fresh state, to provide better understanding about the mineral changes in the parent material as a result of chemical weathering process (Butler, 1953).

2.4.2. Application of ground-based remote sensing methods to detect weathering

Due to the improvement of safety for users, speed in data collection, possibility of quickly acquiring and analyzing large datasets as well as providing better access to the rock face, terrestrial remote sensing and the application of photogrammetry has encouraged and enabled the use of quality and semi-automated procedures in rock engineering to detect discontinuities and other weathering signatures (Reid & Harrison, 2000). Rengers (1967) and Franklin et al. (1988) mentioned the application of terrestrial remote sensing technique using analogue stereo and digitized photographs to analyze the discontinuity geometry and roughness of the rock mass used to estimate the resistance of the discontinuity to shearing and weathering. Another application of remote sensing technique is the use of computerized electronic tachometer, otherwise known as total station to measure in detail the discontinuity traces on inaccessible rock slopes (Bulut & Tüdeş, 1996). The use of ground-based thermal imaging camera have also been applied to detect and monitor rock mass weathering due to the varying rock temperature, as both direct and indirect heating are found to enhance the breakdown of the rock mass (Warke et al., 1996; Warke & Smith, 1998). Terrestrial hyperspectral (HS) imagery application has also been employed to map the weathered rock mass face and applied in determining the different degrees of weathering on the rock mass through the use of mineralogical and textural associations related to the geomorphologic processes in the study area (Riaza et al., 2001). Table 2-1 below helps to highlight the different ground-based sensors that have been used to detect observable weathering parameters remotely and the possible parameters that can be detected using the UAV photogrammetry.

The invention of the laser scanning and its application for remote sensing has further brought about significant technological advancement in rock engineering. Use of terrestrial laser scanning on the rock mass surface produce dense point cloud which are converted into image data that can be processed using basic photogrammetry principles in combination with pattern recognition to derive discontinuity information for analysis of the geometry, fracture mapping and create 3D imagery of the rock mass surface (Slob et al., 2002).

2.4.2.1. Application of ground-based terrestrial laser scanning (TLS)

Terrestrial laser scanning (TLS) is an active imaging, non-contact method, with a technique for high density acquisition of the physical surface of the scanned objects that is rapidly becoming a standard for 3D modelling of complex scenes (Barnea & Filin, 2012). It has advantage over the manual field and traditional remote sensing methods (Slob et al., 2005) with the capacity to measure the rock mass face at a distance of nearly 200m in ideal conditions and still achieve a high resolution imagery between 5 to 10mm (Siefko Slob & Hack, 2004). They noted that limitations may be faced in terms of occlusion for a rock mass face with height above the reach of the laser scanner. Slob & Hack (2004) further stated that it is a very useful application to monitor loose blocks, movement in unstable soil and rock slopes and, between fresh and weathered surfaces within a very short period. Over the years, there has been a tremendous increase and variety of remote sensing applications of TLS equipments. Combination of the application of TLS and digital photogrammetric methods has ensured scientific advancement in the measurement of the rates of rock mass surface weathering, allowing for detailed monitoring of surface change at a high resolution spatial and temporal scales, while facilitating the development of digital terrain models of weathering surfaces and surface change (Moses et al., 2014).

2.4.2.2. Application of ground-based infrared thermography (IRT)

Infrared thermography is used to detect and measure the differential surface temperature of the object of study using thermal optical devices, known generally as thermal imager or thermal camera. It is a non-contact method for producing a thermal image from the infrared radiation emitted by objects due to their thermal conditions, since any object with a temperature above absolute zero (i.e., T > 0K (-273^{O}C)) emits infrared radiation (Usamentiaga et al., 2014). Images acquired using thermal infrared cameras are converted into thermal images by assigning a color to each infrared energy level. However, thermal images are limited to the detection at relatively shallow depth, just a few millimetres under the surface, but it is assumed that the radiation at the surface of the object of study is most often influenced by the sub-surface condition, which effects the thermal characteristics of adjoining materials.

Table 2-1: Observable parameters of the different types of weathering signatures and the list of proposed sensors that has the possibility to provide representative results when applied in detecting them based on literature.

Observable weathering Signatures	Ground-based Sensors used to detect weathering signatures in past research.				UAV Platform	Literature Support
	Optical Camera	TLS	Thermal Camera	Hyper-Spectral	Optical Camera	
Physical						
Discontinuities planes and set.	Y	Y	Y	N	Y	(Curtaz et al., 2013);
Persistence.	Y	Y	Y	N	Y	(Miller, 1968)
Discontinuities spacing.	Y	Y	Y	N	Y	(Curtaz et al., 2013)
Roughness.	Y	Y	N	N	Y	(Curtaz et al., 2013)
Aperture.	Y	Y	Y	N	Y	(Curtaz et al., 2013)
Weathering products- (Gravel, sand & fine debris)	Y	N	Y	N	Y	(Romo et al., 2013); (Miller, 1968)
Change in color.	Y	N	Y	Y	Y	(Fowler et al., 2011)
Texture.	N	N	N	N	N	(Kirkland, 2003)
Vegetation.	Y	Y	Y	Y	Y	(Miller, 1968)
Organic activities.	Y	N	Y	Y	Y	(Piatek et al., 2013)
Temperature variation.	N	N	Y	Y	N	(Wu et al., 2000); (Piatek et al., 2013)
Chemical						
Clay minerals.	N	N	N	Y	N	(Miller, 1968); (Riaza et al., 2001)
Magnetite & Hematite & Quartz.	N	N	Y	Y	N	(Miller, 1968); (Riaza et al., 2001)
Carbonate compounds and	N	N	Y	Y	N	(Riaza et al., 2001)
Oxides of Ca, Na, Mg and K.	N	N	Y	Y	N	(Miller, 1968)
Presence of water.	N	N	Y	Y	N	(Miller, 1968)
Temperature variation.	N	N	Y	Y	N	(Miller, 1968); (Piatek et al., 2013)

Warke & Smith (1998) stated temperature as having the most significant control on physical rock weathering and contributes directly to the disruption of the rock mass through the process of chemical weathering. Warke et al. (1996) discovered that when cleaned, the effect of particulate deposit on a rock surface with low thermal conductivity and high albedo is extremely distinct. The presence of the staining and weathered products on a rock mass at varying degree was noticed to have caused both surface and near-surface temperature variations, which are responsible for the physical breakdown of the rock mass as they affect precisely the zone in which physical weathering mechanisms are concentrated. They noticed that the presence of weathered products increases the surface temperature of the rock mass in contrast to the regions not covered. González-Gómez et al. (2015) mentioned temperature variations influence the intrinsic properties of a rock mass which can be observed as a significant color change. Examples were given of the oxidation of iron, a chemical action caused by temperature, resulting to a red coloration due to the presence of hematite, whereas less common yellow and brown colorations are due to the presence of limonite and goethite respectively, green-gray to black color in rocks is related to the presence of total organic carbon, where as darker colours are related to higher carbon content. They also observed that as the rock color darkens with increase in temperature, there is decrease in the reflectance while light rock colour gives higher reflectance. Bland and Rolls (1998) cited in Hall, Meiklejohn, & Arocena (2007) mentioned that dark rock mass surface, as a result of weathering process, due to presence of weathered products or just as a result of the natural coloration of the rock body, translates to higher temperature while light coloured rock mass surface results to low temperature. However, these observations are in contrast with the findings made by Arocena and Hall (2004); Hall et al. (2005); Hall (2006) all cited in Hall et al. (2007) stating that there is the possibility of lighter coloured materials attaining temperatures equal to or higher than the darker materials under certain conditions, in spite of direct solar radiation.

2.4.3. Application of UAV-based photogrammetry in weathering detection

The application of repeat photography and close range photogrammetry technique is a cheap alternative to directly detect and monitor rock mass surface weathering (Moses et al., 2014). This method involves application of UAV-based imagery processed using basic digital photogrammetry techniques to extract information on rock mass surface weathering (Nex & Remondino, 2013). The use of UAV platforms is an important medium for data collection, detection and 3D modeling process of a weathered rock mass (Remondino et al., 2012). It has encouraged the use of close range remote sensing by the combination of affordable platforms, with regular digital cameras and GNSS systems to acquire relatively accurate data (Remondino et al., 2012). Advances in data acquisition using UAV has created increasing awareness in its use for rock mass surface imagery. It has led research trend to develop simplified methodology, example is the semi-automatic image analysis (Vasuki et al., 2014), as well as free and commercial software to handle the processing, interpretation and the 3D visualization of the data captured in a short flight effectively and efficiently (Vasuki et al., 2014).

The application of UAV to the weathering analysis of external building walls shows loss of materials, fissures, fractures and colour alterations as the main forms of weathering signatures (Ortiz et al., 2013). Although, it was noted that the quality of the imagery did not allow for a clear quantification of changes as a result of the weathering process. Mancini et al. (2013) applied the use of UAV-based imagery with structure from motion (SfM) approach, a photogrammetry technique, to acquire high resolution digital surface model of a beach dune system. They estimated the quality of the point cloud data generated from the approach with a point cloud dataset of the same location acquired using a TLS, to determine the absolute or relative correspondence between UAV-based and TLS methods. The results from the UAV-based point cloud was found to be comparable with the TLS point cloud dataset. Potter & Helmke (2007) mentioned the application of an UAV to a boulder field to obtain information, which from observation of the UAV-based imagery shows the undisturbed exposed upper surface of the boulders were deeply weathered. There were also changes in the coloration of the boulder as a result of loss of iron due to leaching caused by dissolving of the iron minerals through chemical weathering process. In rock engineering, studies have been carried out in the use of UAV photogrammetry and in combination with other ground-based methods (Danzi et al., 2013; Bemis et al., 2014). Hugenholtz et al. (2013) suggests that UAV-based data will offer cheap, quick and more flexible alternative to airborne laser scanning for geomorphologic mapping.

In this chapter, the theoretical background and the datasets were explained. The theoretical background was explained from reviewed literature as the basis for the concept of the research. The processes of weathering were explained, and its influence on certain parameters, termed weathering signatures, on the rock mass from which its effects can be inferred were stated. The datasets can be divided into UAV-based and TLS point cloud datasets, thermal data, and the field investigation data. The point cloud datasets are the main focus for use in the detection of weathering, the thermal data are to be use to support the point cloud datasets in the detection of weathering and the field investigation data are to be used as ground truth to validated the results from the UAV-based and TLS point cloud datasets and the thermal data.

3. DESCRIPTION OF THE STUDY AREA

3.1. Description and location of the study area

The study area is the quarry Gildehaus where the Bentheim sandstone is being mined. It is located $52^0$18'08 north and $07^0$06'14 east in the town of Bad Bentheim in Lower Saxony, Germany. Bentheim sandstone is been the host rock of several oil and gas fields of northwest Germany and the north-eastern Netherlands (Knaap and Coenen, 1987 cited in Dubelaar et al., 2015). In the construction and building industry, it has also proven itself as a very resilient natural and construction stone with its application in use since about 1100 AD (Dubelaar et al., 2015). The Bentheim sandstone are of two types. These have been differentiated by geologists as the lighter-coloured, pale yellow (cream) sandstone, characteristic of the Gildehaus area, on which data for this research study were collected, and the darker reddish-brown found in the area east of Bad Bentheim and they attributed the colour variations to the iron content, that is iron oxide hematite (Fe_2O_3), of the rock mass (Dubelaar et al., 2015; Drees, 2015). The study area, the quarry Gildehaus, is shown in Figure 3.1 below.

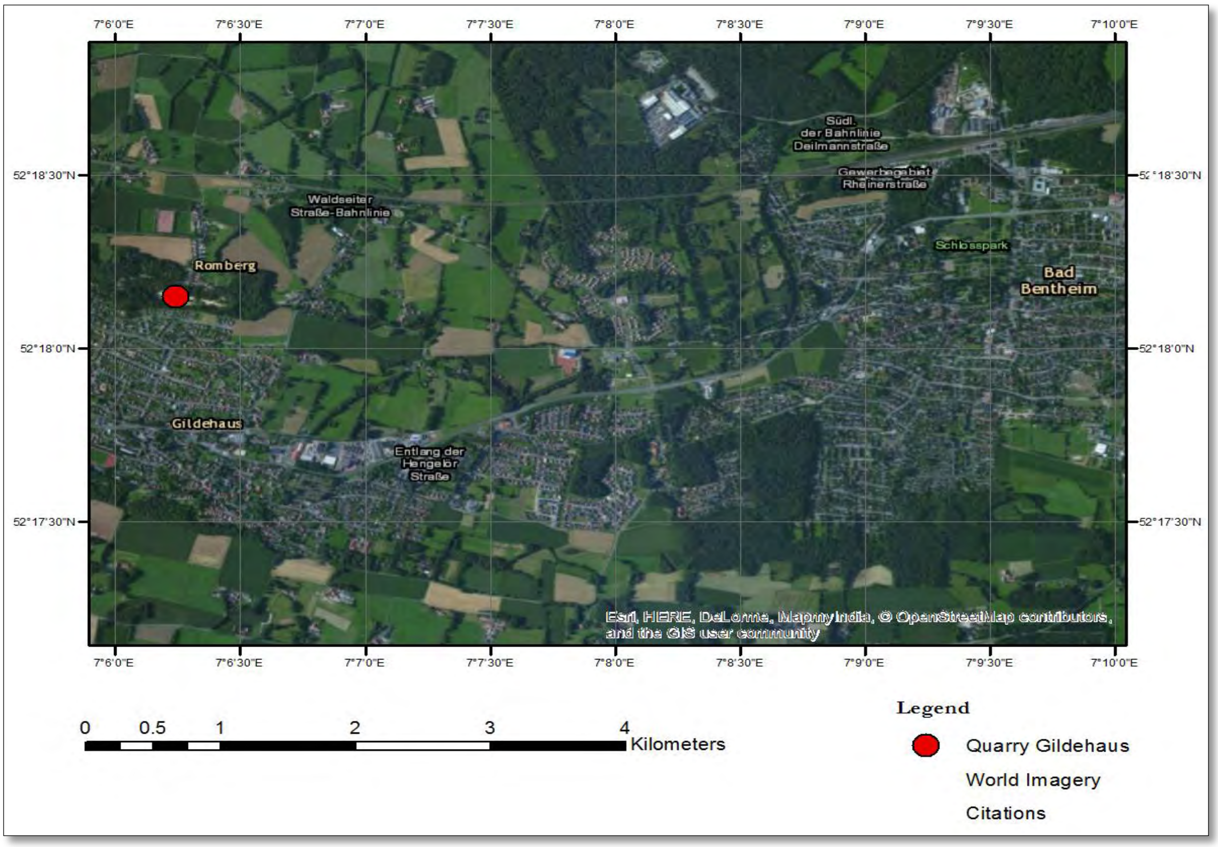

Figure 3-1: Map of the study area. The red point indicates the location of the studied slope, quarry Gildehaus. Source: ESRI, HERE, DeLorme, MapmyIndia, OpenStreetMap Contributors and the GIS user community.

3.2. General geology of the study area

The geology of the study area consists of sedimentary rock deposit of Mesozoic era occurring during the lower Cretaceous period. In the northwest European area, quite a number of basins were present in the lower Cretaceous period, one of which is the lower saxony basin (Figure 3-2). The sedimentation patterns of the lower saxony basin during the lower Cretaceous period were controlled by divergent dextral shear movements related to the contemporaneous rifting or crustal extension which began in the late middle to early upper Jurassic in the Central North Sea valley (Ziegler, 1990 cited in Traska, 2014).

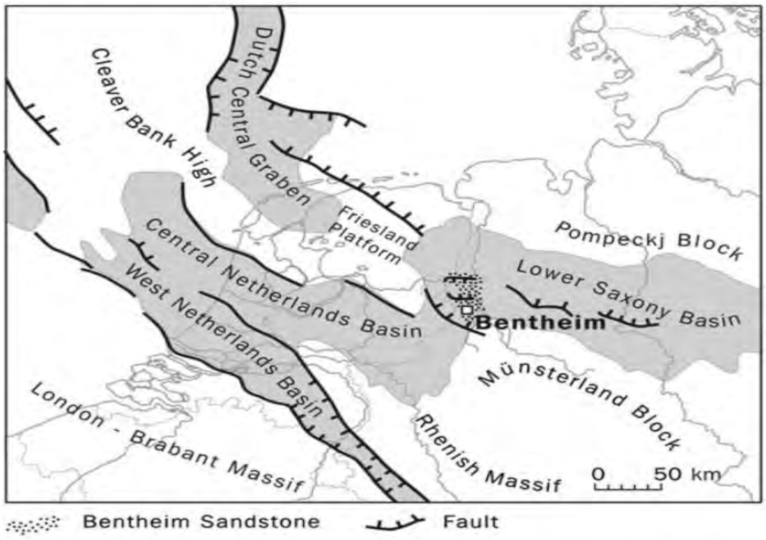

Figure 3-2: Basin configuration during the lower Cretaceous and the period's structural elements in the Netherlands and the adjacent part of Germany
Source- adapted from De Jager and Geluk (2007); Kombrink et al. (2012) and cited in (Dubelaar et al., 2015)

The Bentheim sandstone is characterised by well to fairly well sorted, fine to medium grained, quartz-rich grains which occurs together with minor conglomerate beds. It forms sheet-like and lenticular- shaped sand bodies with thickness of about 80 metres, which consists mainly of coarse-grained to conglomeratic sandstones with pebbles of quartz and frequently contains clay flakes, ironstones and some coals embedded in an argillaceous, very glauconitic sandstone (Mansurbeg, 2001). There is also the occurrence of medium grained sandstones with a high content of calcareous cement. It is found to have similar formation as the reservoir rock from the Schoonebeek oil field, which is approximately a few tens of km North of the quarry Gildehaus, but they differ in terms of microstructure, petro-physical properties and composition (Klein et al., 2001). The Bentheim sandstone is very strong and described as a relatively homogeneous quartz-rich sandstone with porosity of about 23% (Klein et al., 2001). It is a white to yellow color sandstone, containing a mean composition of 95% quartz, 3% feldspar, and 2% kaolinite (Klein et al., 2001). It has grain size that varies from 18um to 500um with the mean grain size about 300um (Reinicke et al., 2008 cited in (Stanchits et al., 2009).

3.3. Description of the studied slope (Gildehaus slope)

The Bentheim sandstone slope is located in the quarry Gildehaus, otherwise known as the Romberg quarry. In the quarry Gildehaus, the Bentheim Sandstone is still being excavated, but the limited volume of quarried rock is now mainly used for restoration purposes. The Bentheim sandstone main outcrops with approximately 9km-long east-west aligned ridge with an average width of about 400m. During the Alpine folding of the basin sediments, The ridge was formed as part of an east-west trending anticline dipping 10–20°to the south (Dubelaar et al., 2015).

Füchtbauer (1963) cited in Dubelaar et al., (2015) stated that the porosity of the Bentheim Sandstone is relatively high with up to 26 volume %. Malmborg (2002) also cited in Dubelaar et al., (2015) stated that the primary porosity was most probably preserved by the quartz cementation. It was concluded that the silica (quartz) cement helped the framework of the Bentheim sandstone to withstand the effect of limited mechanical compaction and overburden pressure, though precipitated in limited amounts.

The slope length and height is approximately 250m and 25m, respectively, but for this research work, only about 2m from the bottom part of the slope are described to provide detailed information of the weathering signatures within the small scale of detection range of 0-50mm, while the whole slope face was described on a larger scale greater than 50mm. The slope faces east ward at a dip-direction of 70^{O} with an average slope dip of 21^{O}. The slope itself consists of whitish yellow sandstone cemented with siliceous quartz. It has a considerable thickness ranging from 200mm to 2m. An overview of the slope as shown in Figure 3-3, gives a description of all units in the slope. A preliminary weathering classification of the slope was carried using the slope stability probability classification (SSPC), after Hack (1998).

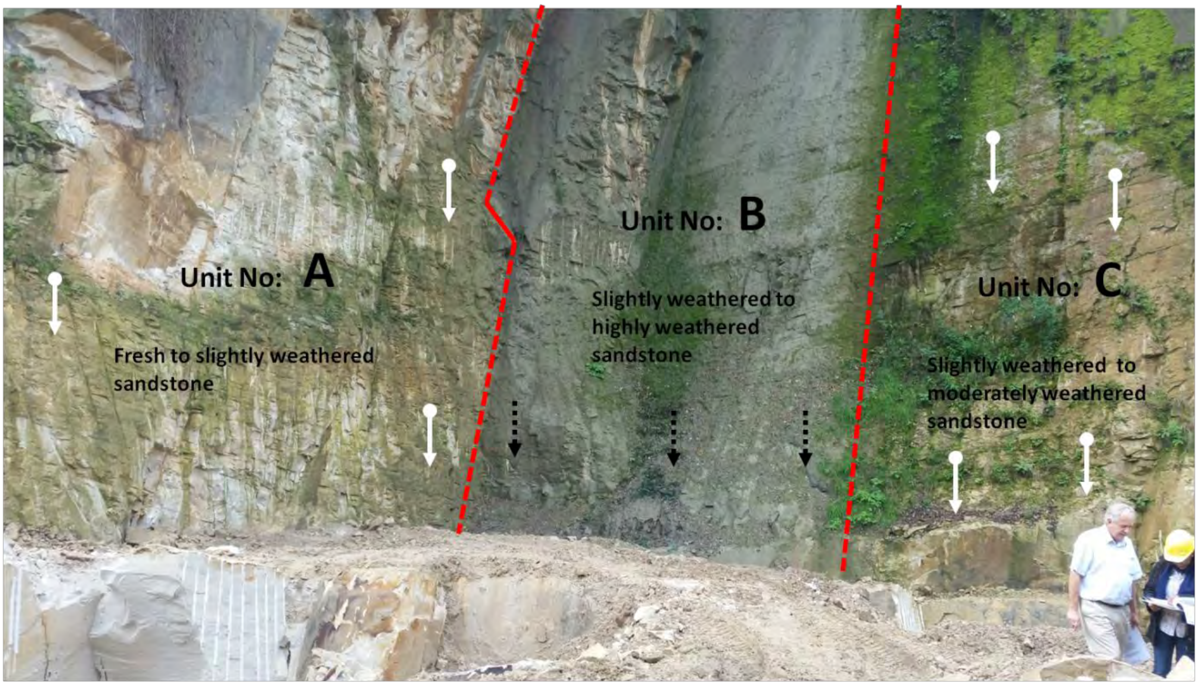

Figure 3-3: The exposure of the Gildehaus slope into classified geological units (see chapter 4.2), the different weathering classes of the slope, the direction of the arrow indicates that the weathering differences are obvious from top to bottom, white arrow indicating oxidation regions of the exposed rock mass, deposit of weathered products and debris (black arrow). Weathering classification follows the approach 2 of the BS5930:1999.

In this chapter, the study area was explained. The study area was explained based on the literature. The chemical composition and geochemical characteristic of the Bentheim sandstone found in the study area was stated and explained, as they influence the susceptibility of the exposure slope in the study area to the effects of weathering process.

4. METHODOLOGY

In this research project, the work flow comprises of five main stages namely- field work for data acquisition; quality and accuracy analysis of the point cloud data; assessment of the detectability of the direct and indirect weathering signatures from the UAV-based and ground-based data using image processing, integration of the TLS point cloud with thermal imagery and lastly the weathering classification of the rock mass using data from the UAV and ground-based sensors. The overall research workflow scheme is shown in the appendices (Appendix 1).

4.1. Data collection

Fieldwork for data collection was carried out from 18th August, 2015 to October 15, 2015. In order to carry out a detailed description of the weathering state of the rock mass, the expression of weathering observed on the surface of the rock mass were used to infer the weathering indicators using referenced information from literature. A preliminary investigation of the study area, the Quarry Gildehaus was carried to determine its suitability for the research work. The preliminary investigation was conducted to identify the location of particular rock mass surface to be investigated. Some of the points considered in selecting the location include the weathering degree and the accessibility of the exposure, but unfortunately, many good exposures could not or only partially be assessed due to safety consideration.

4.2. Data acquisition for the geologic field investigation

4.2.1. Methodology

In-situ field description and classification of the weathered rock mass were carried out using visual assessment, quantification of the discontinuity characteristics and the simple means steps as described by Hack & Huisman (2002), Hack et al., (2003), Tating (2015) among others in accordance to BS standards using the Approaches 1 and 2 of the BS 5930:1999 (see Chapter 2.3.1.1). Below is an overview of the steps taken to achieve this objective.

-Identification of rock mass surface, carried out during the preliminary site investigation.

-Identification of the geotechnical unit(s) on the rock mass surface using the discontinuity orientation measuring with an inclinometer and geological compass, (see Figure 3-4).

-Determination of the intact rock strength; the discontinuity set(s) geometry to estimate the discontinuity spacing and persistence; and the condition of discontinuity set(s) to estimate the roughness, aperture and infill material using a geological hammer, geological compass, measuring tape, use of hand pressure, through tactual and observation.

-General information and observations not included in the rock mass characteristics but important for the study such as method of excavation at the study area, accessibility, observed stability, vegetation etc.

-The rock mass parameters for the geotechnical unit(s) are classified and the rock mass weathering states are evaluated and graded based on the Approaches 1 and 2 of BS 5930: 1999 specifications as used in SSPC system (Hack et al., 2003; Hack, 1998; Mulenga, 2015) (see Chapter 4.2.3).

4.2.1.1. The geotechnical units in the rock mass

Hack (2006) expressed that orientations of discontinuities with the same origin are related to the process that has created them and to the geological history of the rock mass. Thus, orientation, defined as the discontinuity's attitude in space, is important in its use in delineating clearly the discontinuity set(s). The discontinuity sets were defined visually with discontinuities having the same dip and dip direction grouped together has a unit or set. The notation for the discontinuity orientation has used in the SSPC data collection sheet is dip/dip direction, with example, J-I - 10/65 meaning Joint set I with dip of 10° and dip direction of 65°; Note bedding planes are denoted as B and faults as F (Cabria, 2015).

4.2.1.2. Rock mass characteristics and quantification of the intact rock strength

An overview of the characteristics of the rock mass were obtained using parameters such as the rock name, texture, structure, grain size, colour, discontinuity geometry and condition, intact rock strength and the weathering state of the rock mass. Overall, visual observation was carried out on almost all the parameters except the intact rock strength.

- The geological rock name was obtained from the rock identification and geological map;
- Texture was obtained by tactile and hand lens. The texture of the rock mass are described as porphyritic, crystalline, cryptocrystalline, amorphous or glassy;
- Structure was assessed by observation referencing the scale in BS 5930:1999 (Appendix 2a). The structure of the rock mass are described as bedded or laminated for sedimentary rocks, foliated or banded for metamorphic rocks while flow-banded was used for igneous rocks;
- Grain size data was obtained using the sand disc ruler referencing Table 14 (pg 128) of the BS 5930:1999 (Appendix 2b);
- Colour for rock material and discontinuities was obtained using the Munsell colour charts;
- The discontinuity geometry and condition (spacing, persistence, roughness, aperture, infill material) was obtained using the measuring tape, hand pressure, through tactual. Following BS5930:1999, the discontinuity spacing was measured perpendicular to the discontinuities with the minimum spacing considered while the persistence measured along dip and along the strike was described as either continuous or discontinuous (Cabria, 2015). The roughness was assessed on two scales, large-scale (Rl) and small-scale (Rs). The large-scale roughness was determined in an area larger than 20cm x 20cm but smaller than 1m x 1m and it was described as either, wavy, slightly wavy, curved, slightly curved or straight while the small-scale roughness was assessed on an area of 20cm x 20cm and described as stepped, undulating or planar with tactual observation classified as rough, smooth or polished (Price et al., 2009). The infill material are described as cemented, non-softening or softening when in contact with water.
- The simple means method was used to estimated the intact rock strength by application of hand pressure and the geological hammer. The parameters for the estimated unconfined compressive strength was assessed referencing the scale in BS 5930:1999 (Appendix 2c).

4.2.1.3. Description of the weathering state of the rock mass

Standard factual description of weathering was carried out using the exposure characterization sheet of the Slope Stability Probability Classification (SSPC) to systematically record the field observations which mainly consist of the description of the rock material and discontinuity properties. The weathering description of the rock mass follows the format in accordance to Approach 1 of the BS 5930:1999. The description parameters obtained where classified according to the BS5930: 1981 (Appendix 2d) and Approach 2 of the BS 5930:1999 (Table 4-1) incorporating the SSPC system (Hack, 1998). The complete SSPC sheets showing the description of the studied slope are included in the appendices (Appendix 3).

4.2.1.4. Sampling

To analyse the influence of chemical weathering on the rock mass, samples were collected from each of the geological units which are to be analysed in the laboratory. The samples were kept in sealed plastic bags to help maintain their original conditions. Unfortunately, due to the restrictions at the quarry, accessibility as well as difficulty in harvesting part of the rock mass, not all the weathering grades encountered were sampled. However, the samples acquired are a good representative of the Gildehaus slope. The two rock samples collected from the unit A were acquired from freshly exposed rock mass and labelled A1 and A2, while the samples collected from unit B and C were also labelled correspondingly. For unit B, three samples were collected with the third sample representing the completely weathered and residual soil at the foot of the rock mass and it is labelled Residual.

Table 4-1: Description and classification of a weathered rock mass following BS5930:1999 incorporating the SSPC system

Approach 2- Classification for uniform materials (For rock moderately strong or stronger in fresh state)			
Grade	**Classifier**	**Typical Characteristics**	**WE**
I	Fresh	Unchanged from original state.	1
II	Slightly weathered	Slight discolouration, slight weakening.	0.95
III	Moderately weathered	Considerably weakened, penetrative discolouration. Large pieces cannot be broken by hand.	0.90
IV	Highly weathered	Large pieces can be broken by hand. Does not readily disintegrate (slake) when dry sample immersed in water.	0.62
V	Completely weathered	Considerably weakened. Slakes in water. Original texture apparent	0.35
VI	Residual soil	Soil derived by in-situ weathering but having lost retaining original texture and fabric.	

4.2.1.5. Expected Output

The expected output was a detailed factual field description and weathering classification table to be derived from the study of the rock mass characteristics, quantification of the intact rock strength as well as the weathering characteristics and condition of the rock mass surface. These parameters was to be analyzed using the weathering signatures has key factors, taking into consideration elements that are likely to influence the weathering signatures and the weathering condition of the rock mass to help classify the studied slope.

4.3. Data acquisition for the UAV -based imagery, TLS dataset and thermal imagery of the study area

4.3.1. UAV-based imagery

The framework for the acquisition and processing of the UAV-based imagery involves three main steps. They are image acquisition, dense matching and accuracy improvement of the UAV-based point cloud data. Careful planning was carried out to simulate the UAV flight at the studied slope to obtain oblique overlapping images of the rock mass surface using the DJI PHANTOM II Vision platform. This was achieved using manual flight operation with the camera setting configure to capture images at every 5 seconds time-step. The point cloud data was derived using the scale-invariant feature transform (SIFT) operator, structure from motion (SfM) approach and patch-based multi-view stereo (PMVS), all are photogrammetry techniques incorporated into the Pix4DMapper software. The SIFT operator finds similar feature key-points identified in each of the overlapping RGB images. Using the bundle adjustment process of the SfM approach, the feature key-points are matched using the nearest neighbour approach and random sample consensus (RANSAC) algorithms to generate a sparse point cloud. Application of PMVS was used in carrying out the dense image matching process to finally generate the dense 3D point clouds of the rock mass as shown in Figure 4-1. Eight (8) ground control points were collected to use in the geo-referencing of the acquired images, to ensure high accuracy, quality and precision results, otherwise the results cannot be used for measurements, overlay, and compared with others.

4.3.1.1. Digital imagery and 3D UAV-based point cloud assessment

This step was used to carry out visual inspection of the datasets aimed to show that the identification of the weathering signatures was possible by the analysis of the digital images captured of the studied slope and the corresponding 3D point-clouds. The quality assessment of the point cloud was done using visualisation approach to check for the completeness of data and the analysis of the quality report generated which gives an average ground sampling distance (GSD) of 8.9mm for a total area coverage of 0.0025km². A sigma value and root mean square error of 0m was acquired after the geo-referencing process using the ground control points, which is less than the GSD value, thus acceptable.

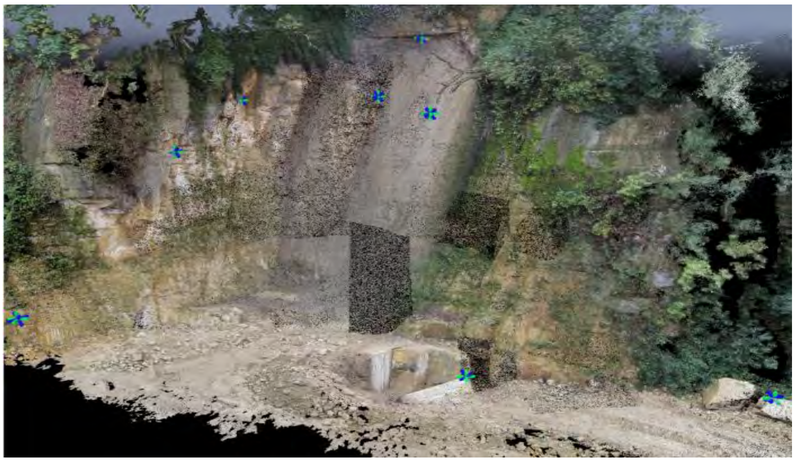

Figure 4-1: UAV-based 3D point cloud of the Gildehaus slope showing the positions of the ground control points (GCPs)

4.3.2. TLS dataset

The V-Line 3D terrestrial laser scanner RIEGL VZ-400 was used to acquire the TLS dataset of the studied slope. Equipped with a narrow infrared laser beam with instantaneous scanning mechanism, it provides high speed, non-contact data acquisition. Its unique RIEGL's echo digitization and online waveform processing ensures very high laser ranging accuracy that permits realisation of better measurement capability even under adverse atmospheric conditions and the appraisal of numerous target echoes. The scanning of the rock mass surface was carried out using the line approach, which is based on a fast rotating multi-facet polygonal mirror, this offers completely linear, unidirectional and parallel scan lines. The TLS data was acquired by scanning of the rock mass from a single standpoint. The problem of occlusion in the XY direction was not a limiting factor as the scanning covered the total area of interest of the rock mass surface as a result of the scanner capability of a 360° x 360° field of view, thus the problem of occlusion associated with single scan is negligible. The point cloud of the studied slope was extracted from the scan data and processed using the RiSCAN software as shown in Figure 4-2.

Figure 4-2: TLS 3D point cloud of the Gildehaus slope showing the laser scanning position

4.3.3. Thermal imagery of the study area

To determine the radiant temperature of the Gildehaus slope (see Chapters 1.1.2 and 2.2.6), TH9100PMV thermal infrared camera was used to acquire both the visible and thermal images of the rock mass surface, with the camera mounted on a tripod levelled using a bubble level. The thermal camera (Appendix 4) has a spectral response range of 8 to 14 µm which provides an excellent atmospheric window and satisfies the criteria of being the preferred window for terrestrial remote sensing (Gupta, 2003). Three sets of images were captured at different times during the day to enable the analyses of the diurnal temperature cycle effect on the radiant temperature of the geological units of the rock mass surface. From the basic principle of the diurnal cycle which was conducted for 24 hours, from dawn to sunset, the peak heating of the sun is established as noon period, with the peak absorption and radiation of thermal infrared taken between 1-4 hours after noon (Sabins, 2007). For the study, the emissivity value for the temperature camera was set at 1, to enable the acquisition of the radiant temperature of the rock mass surface. The first set on thermal images were taken by 9am, the 2nd were taken at noon (midday - 12pm) while the last were taken 2hours after noon (at 2pm). The visible and thermal images were exported using the irMOTION collection software with the settings on dynamic scale having a temperature range of 0^0C to 50^0C.

4.4. Data analysis

4.4.1. UAV-based and TLS 3D point cloud data

The UAV-based and TLS 3D datasets were inputted into CloudCompare software for alignment and registration to ensure a uniform platform for analysis and quantitative comparison. This was carried out to assess the agreement and variation between the two datasets in order to allow the weathering features detected in either DEM to be compared. CloudCompare is a point cloud processing software designed to carried out direct comparison between dense 3D point clouds (Girardeau-Montaut, 2015).

4.4.2. Methodology

4.4.2.1. Alignment and Registration of the 3D point cloud datasets

In CloudCompare, manual and automatic techniques are the two main methods to roughly and / or finely align and co-register point cloud datasets relatively to each other to the same reference system. This helps to provide a uniform benchmark between the two datasets for a quality comparison. To finely align and register the point cloud data, there is need to determine which of the datasets will be classified as the 'Data' (or Registered, that is, the dataset to be moved eventually) and the other to be classified as the 'Model' (or Reference, which is the dataset that would not be moved). The TLS point cloud dataset was set as the model or referenced data due to its established advantage of having a very high point density achievable up to a resolution of 3mm (Slob et al., 2004; Slob & Hack, 2004) and using visualisation analysis, which follows as stated in the software's user manual to select the denser dataset as the model or reference. Under the manual technique, match bounding-box centres followed by picking point pairs were applied on the UAV-based and TLS 3D point cloud datasets to align and register the datasets.

- Match bounding box centres- It is a very simple and the most easiest method that is used to roughly align and register point cloud datasets. It translates the entities relative to each other by centring all the selected point cloud datasets on their respective centre of gravity.
- Picking (equivalent) point pairs- It is also a simple but powerful method to finely align and register two point cloud datasets quite precisely. In certain instances were two point cloud data have great differences on large extents, It provides the singular means of finely aligning and registering the point cloud data. It is applied by picking at least three equivalent point pairs in both datasets. Although a manual process, it can be relatively fast and quite accurate.

Under the automatic technique, fine registration with Iterative Closest Point (ICP) was applied on the UAV-based and TLS 3D point cloud datasets to align and register the datasets.

- Fine registration with ICP- Presently, it is the only automatic method available to very finely register two point cloud data using the well-known ICP algorithm. It is applicable based on the assumptions that both point cloud data have already been roughly registered and that both data represent the same object having at least the same overall shape or on their overlapping parts.

For each of the techniques used to achieve the fine alignment and registration of the datasets, a rigid transformation matrix (that is a 4x4 matrix) is generated to enable the registered data move relatively to the reference data. The resulting root mean square error (RMSE) is generated which should be less than the fixed scale value of the datasets when using picking point pairs method or less than the given threshold between two iterations when using the fine registration with ICP method with a specified level of overlap of the data/registered point cloud relative to the model/reference point cloud if both clouds were registered (Girardeau-Montaut, 2015). The output from the picking point pairs analysis carried out on the two datasets gives an information of final RMSE value of 0.201466 which is lesser than the fixed scale value of 1.0 used for the analysis, thus within acceptable range (Table 4-5). Similarly, the output from the ICP method carried out gives an information of final RMSE value of 2.08217 which is greater than the given threshold of $1.0e^{-05}$ (0.00001) set as the computation accuracy limit for a theoretical overlap of 100% computed on 50,000 points used for the analysis. This value is not within acceptable range and the large variation from the computation accuracy limit is due to the 50,000 points, as the point cloud number in both the UAV-based and TLS datasets are well over 3,000,000 points. Consequently, the alignment and registration used for the data comparison of the datasets was the picking point pairs method.

4.4.2.2. Data comparison

To carry out the comparison process between the finely registered UAV-based and TLS point cloud datasets, a distance computation tool was applied to the datasets. This is used to compute the cloud to cloud distances between the two data, with the maximum distance of the data/compared point cloud to the model/reference point cloud under the general parameter tab set to 1m followed by the application of the local modelling strategy. The strategy helps optimise the results and consists of the computation of a local model around the nearest point in order to accurately approximate the real surface and get a better estimation of the real distance. For the datasets, computation was carried out using both 6 and 8 number of neighbours nearest to any given point and the height function model. The model is a quadratic function with a high level of versatility and fidelity to the local geometry which ensures that the computed distances are statistically accurate, although rarely, there may be occurrences of modelling aberration due to local approximation. Thus it is advisable not to compute the cloud to cloud analysis for just a single point.

4.4.2.3. Expected Output

The expected output were co-registered UAV-based and TLS point cloud data with the transformation matrix within acceptable RMSE range. Point cloud data showing the results from the cloud to cloud comparison carried was also expected to be generated with the differences between the two datasets shown as a scalar function ranging from 0m to 1m. The output from this process would be used as an input data in both the CloudCompare and Matlab programming software to carry out the extraction of probable weathering signatures presence in the datasets.

4.4.3. Extraction of weathering signatures from the point cloud datasets and the thermal imagery

The first step was to convert the scalar intensity of the TLS point cloud into a RGB (that is Red Green Blue) color field similar to the UAV-based point cloud data using it as a reference (Girardeau-Montaut, 2015). The next step was to critically visualize the co-registered 3D point cloud datasets to determine the weathering features that could be detected and likely extracted. The point cloud datasets were then sub-sampled with the random method in CloudCompare software to decrease the number of points but still maintaining all the features of the original datasets. This is to allow for the importation of the datasets saved in ASCII format into the Matlab workspace as the original point cloud data were too large for use otherwise. The weathered regions on the rock mass surface based on the weathering signatures detected (vegetation and organic matter, total organic carbon and oxidation) were extracted based on developed Matlab code to generate a 3D image for each weathering indicator. RANSAC shape detection(qRansacSD) algorithm, a plug-in tool in the CloudCompare software was used to extract the discontinuity geometry from the point cloud data and to ensure a standard comparison, the same parameters were used on both datasets. For further analysis, a combination of the visible and thermal imagery with the point cloud datasets were carried out for visual analysis.

4.4.4. Methodology

4.4.4.1. Vegetation and organic matter on the rock mass surface

Vegetation and organic activities were extracted from the UAV-based and TLS point cloud data using the excess green (ExG) vegetation index derived for analysis using the visible bands (RGB) (Woebbecke et al., 1995 cited in Torres-Sánchez et al., 2014). The use of vegetation indices (VIs) has been utilised in numerous image analysis techniques for quantifying vegetation cover. They are derived based on arithmetic operations performed using the spectral information reflected by the vegetation at different wavelengths (Xiao and Moody, 2005 cited in Torres-Sánchez et al., 2014). The ExG vegetation index was used to enhance the differences between the points containing vegetation spectral, which is classified as the "Green" band in this study as it is the colour representative of the feature in the visible bands, and the points containing non-vegetation spectral. An automatic threshold operation was carried out on the result from the application of the vegetation index to derive an optimum threshold value that sets a breakpoint between both point classes (vegetated and non- vegetated points in the dataset) for better visualisation, using the Otsu's method (Guijarro et al., 2011; Meyer and Neto, 2008 cited in Torres-Sánchez et al., 2014).

$ExG = 2G - R - B$ (4.1) where G is Green band, R is Red band & B is Blue band

4.4.4.2. Oxidized and total organic carbon regions on the rock mass surface

Similar to the concept behind the excess green vegetation index of using the spectral information of the point cloud datasets, a visible image, that shows clearly the features of interest, from the series of imagery captured with the digital camera mounted on the UAV platform was imported into the Matlab workspace. A series of RGB values of the feature of interest (regions with the total organic carbon and oxidation respectively) were noted down from the visible image, about 30 values were taken, and the average was taken and inputted into the RGB color wheel to verify if it gives a good representation of the spectral reflectance similar to that of the feature of interest before acceptance of the RGB values. This step was repeated four times to ensure that the values selected are as realistic as possible. The RGB values with a range of +/-20 were then inputted with the imported point cloud datasets. This translates to mean that the Matlab code should select every point in the imported point cloud data that have exactly the stipulated RGB values or values within a range of 20 below or above the stipulated RGB values.

4.4.4.3. Discontinuity geometry of the rock mass surface

The RANSAC Shape Detection (qRansacSD) algorithm proposed by Schnabel et al., (2007) is a simple interface to the automatic shape detection integrated as a plug-in tool into the CloudCompare software workflow (Girardeau-Montaut, 2015). It was used to detect the planar primitives present in the UAV-based and TLS point cloud datasets corresponding to the bedding and joint discontinuities on the Gildehaus slope based on parameters inputted into the plug-in dialog box such as the maximum distance to primitive set at 0.290, sampling resolution at 0.580, maximum normal deviation at 25.00 degrees, overlooking probability at 0.010000 and the minimum support points per primitive set at 8,000 points.

The most important parameter being the minimum support points per primitive which values were varied severally until a set of planar features corresponding to the orientation of the bedding and joint system on the rock mass was achieved.

4.4.4.4. Thermal image processing

A stacking of the thermal images was carried out for visual inspection which shows the presence of a peak intensity at the right corner of almost all the thermal imagery even when unexpected (see Appendix 8). Thus, an assumption was made that there is a linear or gradient in background of the camera influencing the quality of the thermal images captured. To verify this assumption, thermal images were captured in the lab using the same thermal camera with the same set of parameters as were used in the study area to capture the background image of the camera (Figure 4-3a-b).

(a)
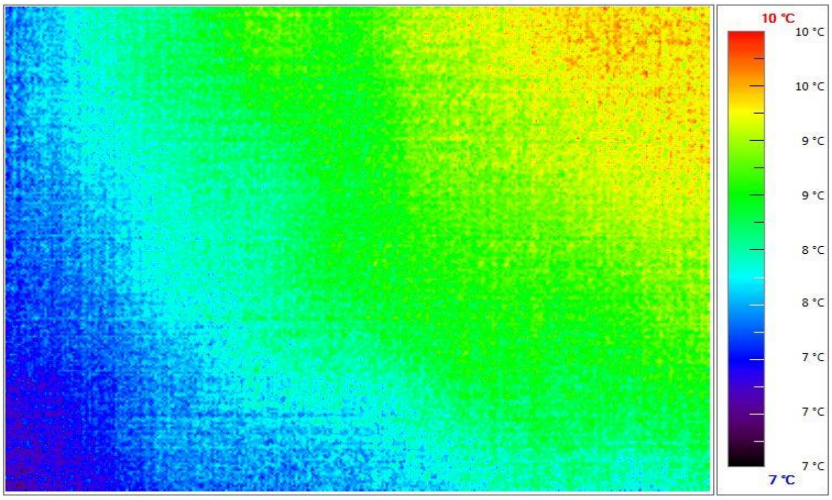

(b)
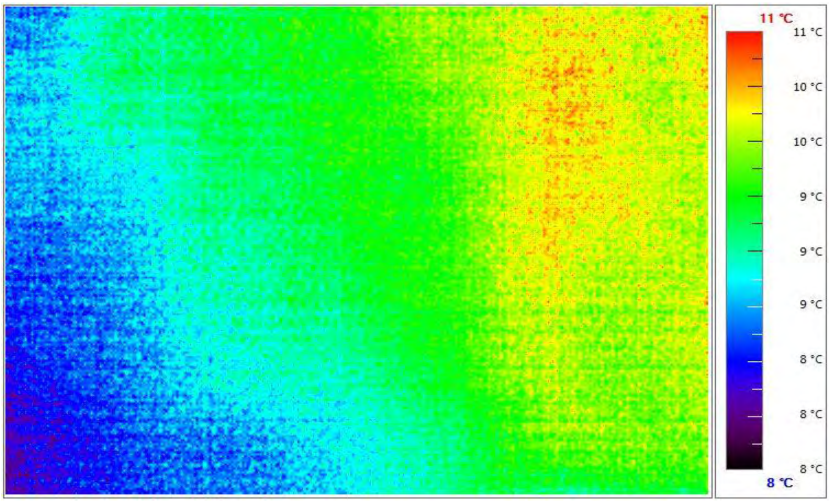

Figure 4-3: Thermal images capturing the background of the thermal camera. (a) shows the first thermal image of the rock mass with temperature 7-10^{0}C, (b) shows the thermal image captured in the laboratory with temperature 8-11^{0}C.

This was done by covering the lens of the camera with three sheets of aluminium to block every form of light, although the ambient temperature in the lab is higher than that of the study area, thus there might still be some infrared radiation influencing the captured image. To remove this background, the first thermal image taken in the morning was also considered since it is best to reason that the rock mass is still very cold at the time and thus the emission of the thermal radiation is very low. Also the ambient temperature of the rock mass was very cold at about 6-7^{0}C and thus, the assumption is that the camera is not receiving any thermal radiation from the rock mass but just measuring the dark count of the background which makes the first thermal image a good representative of the linear background.

Comparison shows a similar pattern to the first thermal image of the rock mass but the temperature ranges are different with the thermal image taken from the lab giving a maximum temperature of 11^0C while the first thermal image as well as the other thermal images taken of the rock mass in the morning gives a peak temperature of 10^0C, making the first thermal image of the rock mass a better representative of the background of the thermal camera. The background was subtracted from all the images to acquire the true radiant temperature of the rock mass.

4.4.4.5. Visual analysis of the UAV-based and TLS point cloud data with Thermal imagery

Sections were segmented from the UAV-based and TLS datasets corresponding to the regions captured in the thermal images from each of the geotechnical units, similar to where the geologic investigation was carried out for the small scale range of detection. A combination of the datasets, the thermal imagery from 9am, 12pm and 2pm, UAV-based and TLS point clouds, were integrated together and analysed visually.

4.4.4.6. Expected Output

The expected output were a 3D imagery of the co-registered UAV-based and TLS point clouds with the weathering signatures highlighted. The possibility to also quantified the percentage of the weathering signatures presence on the Gildehaus slope is expected to be help carried out statistically comparison to determine how much of the weathering signatures can be detected in the two point cloud datasets. The integration with the thermal imagery is expected to further highlight whether the signatures are consistent with the expected weathering parameters has referred from literature.

4.5. Laboratory analysis

Spectral measurement was carried out to assess the presence of certain elements and minerals in the rock mass known for their influence on the chemical weathering process using the portable X-ray Fluorescence (XRF) analyzer, powder X-ray Diffraction (XRD) equipment and Bruker Vertex 70 Fourier Transform Infrared (FTIR) spectrometer. The analyses were carried out at University of Twente ITC Faculty spectral laboratory.

4.5.1. Methodology

4.5.1.1. Determining the mineral composition and clay mineralogy of the samples

Laboratory tests were carried out on each of the rock samples collected at each of the geotechnical units of the Gildehaus slope to determine the presence of clay minerals and the presence of mineral compositions that may likely give indications of the occurrence of weathering process using the powder X-ray diffractometer (PXRD) as an augmentation to the weathering degree determined by visual assessment during the geological field investigation. Fresh (un-weathered) samples were acquired in the quarry from newly excavated rock exposure without the influence of atmospheric and penetrative oxidation. For each of the geotechnical units, two test samples were prepared from different surfaces of the rock samples to give an holistic representation except for unit B whereby three test samples were prepared with the third test sample representing the residual soil. The test samples preparation for analysis involves the fine grinding of the rock samples into homogenous powder and filled into a calibrated sample holder. The powder X-ray diffraction (XRD) was used because of its rapid, non-destructive analytical technique to analyze all varied form of crystalline and amorphous materials inclusive of their properties such as phase composition and crystal structure within short periods. The scan covered a 2-theta range of 4.5° to 80° with an increment of 0.006 degrees and a 2-second count time per step. The resulting X-ray diffraction phase pattern obtained from the tested samples extracted using the DIFFRAC.EVA software are compared with the 2θ (theta) values, based on Bragg's law which prescribes the 2θ angular position for each peak, from a reference database to identify the pattern of the phases for corresponding minerals.

Supplementary samples were prepared for the clay mineralogy to provide additional support for the results from the mineral composition analysis using the pipette test method. This method was used because of the very high peaks of the quartz minerals noticed during the analyses using the methodology stated above which overshadows the presence of other minerals in the rock samples. Powdered rock samples (measured 25 grams) from each of the geotechnical units were mixed with 1liter of demineralised water in a sample bottle and place on a shake table for 24 hours (Figure 4-4a). The mixture was poured into a measurement beaker and using a pipette, 500ml of the suspension were collected after allowing the mixture to stand for 45mins and heated on a hot plate for the water to dry up (Figure 4-4b). The resulting residue were filled into the calibrated sample holder and analysed using the PXRD.

(a)  (b) 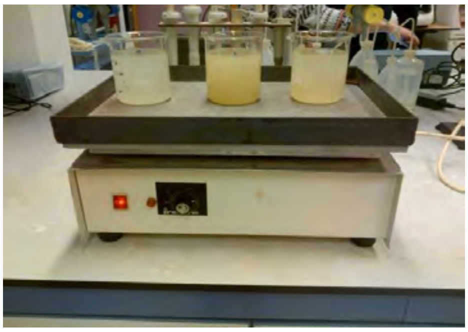

Figure 4-4: Set up for the extraction of rock samples for the clay mineralogy test. (a) Collection of solution into the beaker with a pipette, (b) Removal of water from the solution.

4.5.1.2. Detection of minerals using the X-ray Fluorescence (XRF) analyzer

This analysis was carried out in support of the detection of the presence of certain minerals that influence the possibility of the occurrence of chemical weathering process on a rock mass (see Table 1-1). Portable NitonXL3 XRF analyzer was used to analyse the rock samples taken from each of the geotechnical units with an average of three test carried out on various parts of the rock sample for a holistic representation. The soil mode under the mining analysis was used with a 90-second measurement range. This mode was selected because it is the best for detecting the possible presence of low concentration elements at 0.5% (5000 ppm) or even less. XRF is a non-destructive equipment often used for the quick determination of elemental composition of a rock sample, but care as to be taken during operation to avoid the exposure of the user to radiation and also exposure of the XRF analyser to strong electromagnetic fields.

4.5.1.3. Emissivity spectral analysis of the rock samples in the thermal bands

Bruker Vertex 70 Fourier transform infrared (FTIR) spectrometer instrument modified with an external integrating sphere with a 30 mm sampling port to allow for measuring large, inhomogeneous samples was used for the reflectance spectral analysis of the rock samples using the concept of infrared spectroscopy. The modification of the spectrometer does not in any way hinder it reliability, as shown in Hecker et al., (2011). Three (3) test samples were analysed over eight consecutive measurements from each of the rock samples collected at the three geotechnical units of the Gildehaus slope. Due to the effect of a small fraction of incoming energy being reflected off the edge of the sphere, rather than the sample itself, correction for background radiation was applied to both the gold plate, used as a reference test sample, and the rock sample measurements before a ratio of the two was performed. The correction was achieved by first measuring the empty sample port, then subtracting the empty measurement from the gold plate and rock sample measurements. HypPy software using the Opus converter algorithm was then used to extract the reference test sample and rock sample measurements including the empty port measurements which were used to generate the reflectance spectra of all the samples (Fagbohun, 2015; Hecker et al., 2011). FTIR spectroscopy with the advantage of being sensitive to both crystalline and amorphous materials, is used to obtain an infrared spectrum of absorption or emission of a material by analysing the spectral features of the material from the generation of patterns, a function of wavelength caused by the vibrational fundamental modes in the molecular structure of the material analyzed when excited. These spectral features are unique to various minerals and can be used to identify the material's components or to determine its mineralogic details which can be used as an addition to ground truth or remotely-sensed data. Following Kirchoff's law of thermal radiation, which states that for the maintenance of equilibrium absorptivity (α_λ) and emissivity (ϵ_λ) of each wavelength are equal, and the energy conservation law, which states that all incident electromagnetic radiation with an object are either absorbed, reflected or transmitted.

$\alpha(\lambda) + \varrho(\lambda) + \tau(\lambda) = 1$ (4.2) Energy conservation law

where: $\alpha(\lambda)$ is the absorptivity or absorptance, $\varrho(\lambda)$ is the reflectance and $\tau(\lambda)$ is the transmittance of the object.

$\alpha(\lambda) + \varrho(\lambda) = 1$ (4.3) For opaque objects, where $\tau(\lambda) = 0$

Where: $\alpha_\lambda = \epsilon_\lambda$ (4.4) Kirchoff's law

Thus, $\epsilon_\lambda + \varrho(\lambda) = 1$ (4.5)

Whereby: $\epsilon_\lambda = 1 - \varrho(\lambda)$ (4.6)

This is used to estimate the emissivity (see Chapter 1.1.2) from the reflectance spectral measurements of the rock samples, with the assumption that the object is opaque (that is impenetrable by radiation), thus no incident electromagnetic radiation is being transmitted but is either being absorbed or reflected.

4.5.2. Expected Output

The expected output was a list of elements present in the rock mass that have been established by literature to be indicative of the likely occurrence of weathering process from the analysis to be carried out using the portable X-ray Fluorescence (XRF) analyzer, while the presence of four (4) mineral compositions namely Quartz, Kaolinite, Hematite and Magnetite are to be earmarked during the powder X-ray Diffraction (XRD) analysis. The reflectance measurements are to be used as inputs to determine the emissivity following Kirchoff's law, to determine the variation in the emissivity of the rock mass as a result of changes to its composition due to the influence of the weathering process.

In this chapter, the methodology was explained. The methodology can be divided into three stages. First, the analysis of the field investigation data in order to determine the weathering grade in each of the likely geotechnical units in the rock mass, and the influence of weathering process on the weathering signatures observed on the rock mass. Second, the data collection and analysis of the UAV-based data, TLS data, and the thermal data in the detection of the weathering signatures observed in the datasets. Third and final, the assessment and estimation of the weathering signatures detected using the UAV-base and TLS point cloud datasets. The assessment results are to be validated by the table developed from the field investigation.

5. RESULTS AND DISCUSSION

The results of the previously described methodology are presented in this chapter and it follows similar structure as the methodology chapter. This details first the analysis of the geologic field investigation carried out, the laboratory analysis of the rock samples, followed by the comparison analysis of the UAV-based and TLS point cloud data, the weathering signature feature extraction from the point cloud datasets and analysis of the thermal imagery, and lastly the aggregation of the results to develop an overall scoring to the datasets to determine the most optimal in the possible detection of weathering signatures.

5.1. Weathering description and classification of the Gildehaus Slope

Weathering has been shown to affect the properties of both intact rock and discontinuities (Hack & Price, 1997; Huisman, 2006; Tating et al., 2014). All the geotechnical units of the slope investigated in the Gildehaus Quarry are geologically about homogene, which means each geotechnical unit is of about the same rock type geologically. Weathering has affected the rock mass such that the top part of the slope is most weathered and weathering reduces downwards. A field investigation was carried out to identify parameters with which weathering signatures can be determined. All descriptions follow the British Standard BS5930:1999.

5.1.1. Weathering

The investigated slope (Gildehaus slope) has been vertically divided in different layers identifiable visually on colour, texture and structure. The higher parts of the slope are not accessible at the location of the investigated slope, but these layers can be identified further to the west or east in the same quarry.

5.1.1.1. Vertical variability

(i) Layer I- The rock material in the upper most part of the slope (layer I) consists mostly of brownish to dark-grey coloured organic soil. This unit is inaccessible at the location of the slope, but the same unit can be more closely observed further to the west in the same quarry of Gildehaus. It is assumed that the layer does not change very much over the length of the quarry. The zone consists of residual soil and completely weathered rock mass and some part of the highly weathered rock mass as shown in Figure 5-1.

(ii) Layer II- consists of thin to medially bedded rock mass with noticeable high degree of oxidation of the rock exposure due to the mostly reddish-brown to brownish grey colouration. The zone consists of highly weathered to moderately weathered rock mass as shown in Figure 5-1.

(iii) Layer III- The zone consists of slightly weathered to fresh rock mass with the lower part covered with fallen debris from layer I and layer II, the uppermost part of the weathering profile. It has sparse reddish brown areas of oxidation but is mainly dark grey to dark greenish grey colour of total organic carbon, which is supported by Nijland et al. (2003) which stated the effect of black weathering (it is the dark greyish to black discoloration of the weathered surface of a result of the deposition of iron minerals, trace amount of heavy minerals, airborne particles, micro-biota as well as gypsum) resulting from the presence of total organic carbon on sandstone to be a widespread phenomenon (Figure 5-1). They also mentioned that although only minor amounts of gypsum are present in the black weathered layers, the small amounts is more than sufficient to fixate the airborne particles responsible for the blackish appearance

(iv) The overall thickness of the layers in the weathering profile of the studied slope are not uniform and ranges from 1m to more than 10 m (Figure 5-1).

5.1.1.2. Horizontal variability

(i) Unit A (slightly weathered to fresh rock zone) consisting of cream or off-white coloured fresh rock mass to reddish-yellow and reddish-brown coloured rock mass resulting from oxidation of the exposed surface to the atmosphere (Figure 5-2). This occurs as a consequence of the iron minerals in the rock mass reacting with air or water, or through the precipitation of oxidized iron on the surface of the rock mass. The humid environment of the study area encourages the development of lichens and algae as can be seen from the light greyish green colour of part of the rock mass exposure just few weeks after excavation and exposure of the rock mass surface. Sounding analysis carried out shows no reduction of the intact rock strength except around the discontinuities which shows a highly weathered to completely weathered grade, as well as penetrative oxidation.

<table>
<tr><th>Weathering profile (vertical variability)</th><th>Weathering zone</th><th>Weathering grade</th></tr>
<tr><td rowspan="3">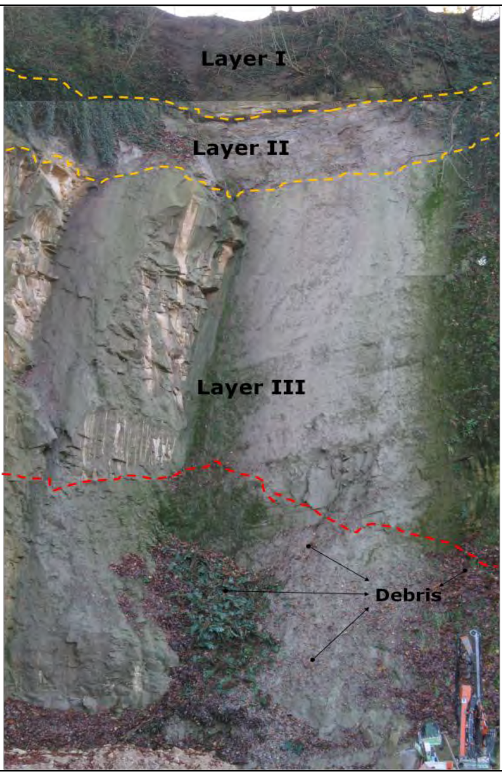
</td><td>Layer I - Residual soil and completely weathered rock mass supporting vegetation.</td><td>VI

V</td></tr>
<tr><td>Layer II - Highly to moderately weathered rock mass, presence of oxidation, downward seepage of water.</td><td>IV

III</td></tr>
<tr><td>Layer III - Slightly weathered to Fresh un-weathered rock mass, greyish colour of slightly weathered rock mass. Sounding analysis carried out shows slight weakening of the rock strength as a result of the downward seepage of water causing the erosion of the surface material of the rock mass, as well as the occurrence of penetrative chemical weathering over time as a consequence.

The red line indicates the start of the boundary of the fallen debris from layers I & II on layer III. Seepage of water, deposit of saturated weathered products (clay and fine sand), debris (moist organic matters from vegetation) at the foot of the rock mass resulting in the weakening of the intact rock strength, stalling of the intact rock surface as a result of physical weathering and penetrative chemical weathering.</td><td>II</td></tr>
</table>

Figure 5-1: Weathering profile of studied slope at the Quarry Gildehaus showing the vertical variability of the weathering zones. The arrows indicate the direction of the seepage of saturation at the upper most of the weathering profile and the progression of weathering along the profile. Weathering grade follows the approach 2 of the BS5930:1999.

(ii) Unit B (weathered rock zone- ranging from moderately weathered to highly weathered) differs from unit A in terms of the discolouration and a reduction in the intact rock strength. The variation is quite abrupt along the planes of weakness, that are the joint discontinuities. It consists of dark grey to dark greyish green, a by-product of the presence of total organic carbon resulting from the discoloration from the downward seepage along the unit and very sparse clustering of lichens, moss and algae on the rock mass surface (Figure 5-2). Presence of saturated weathered products, debris at the foot of the rock mass from the deposit of from erosional process and droppings from vegetation covering the top of the rock mass, results into the influence of moisture on the fresh rock beneath the debris leading to penetrative chemical weathering and weakening of the intact rock strength. Sounding analysis and the use of the simple means test shows slight weakening of the rock mass strength in comparison with unit A, and mostly along the planes of weakness (discontinuities).

(iii) Unit C (weathered rock zone- ranging from moderately weathered to highly weathered) consist also of light reddish brown result from oxidation of the rock exposure to greyish green from the presence of total organic carbon. The green colour on part of the rock mass results from the cluster of lichens, moss and algae as well as sparse vegetation. Development of integral discontinuities progressing to the spalling and disintegration of the intact rock surface as a result of physical weathering. The oxidized surface exhibiting resistance to further weathering process as noticed from the unchanging condition of the rock after the oxidation of the exposure rock mass surface but there is evidence of penetrative oxidation and increase in the spread of the clustering lichens and moss. Sounding analysis carried out shows slight weakening of the intact rock strength especially along and majorly around the discontinuities. The thickness of the weathering profile of the studied slope is not uniform and it ranges from 3 to more than 5 m (see Figure 5-2).

	Weathering profile (horizontal variability)- along a line 2m above the toe of the rock mass		
Weathering unit	Unit A (Slightly weathered to fresh rock zone)- consisting of cream coloured fresh rock mass to reddish yellow and reddish brown coloured rock mass resulting from oxidation of the exposed surface to the atmosphere. Light greyish green colour of part of the rock mass exposure indicates the beginning of the development of clusters of lichens, algae and moss as a result of the humid environment of the Study area.	Unit B (Weathered rock zone)- consisting of dark grey to dark greyish green resulting from the presence of total organic carbon resulting from the discoloration from the downward seepage along the unit (Nijland et al., 2003). This unit can be classified as ranging from moderately to highly weathered.	Unit C (Weathered rock zone)- composed of light reddish brown to greyish green resulting from oxidation and the presence of total organic carbon respectively. This unit ranges from moderately to highly weathered.
Weathering grade	I ⟶ II (Intact rock) IV ⟶ V (Discontinuities)	III ⟶ IV (Intact rock) IV ⟶ V (Discontinuities)	III ⟶ IV (Intact rock) IV ⟶ V (Discontinuities)
	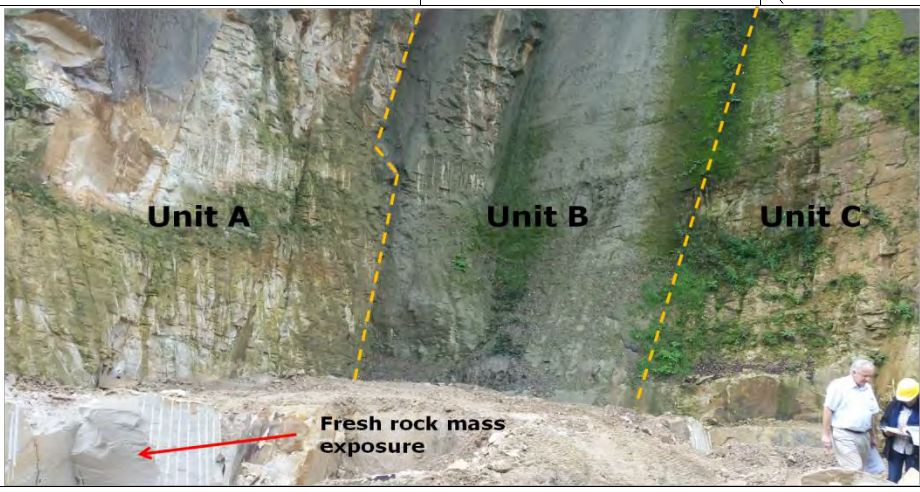		

Figure 5-2: Weathering profile of studied slope at the Quarry Gildehaus showing the horizontal variability of the weathering zones. Weathering grade follows the approach 2 of the BS5930:1999.

5.1.1. Spalling and flaking of the rock mass

The noticeable influence of physical weathering action on the intact rock surface resulting into the spalling and flaking away of the rock material, also the disintegration of the rock mass especially along the planes of weakness in both units B and C of the studied slope (see Figure 5-3). This is likely due to the development of new discontinuities as a result of the continuous increase and reduction of stress relief within the rock mass triggered by the repeated heating and cooling of the surrounding.

(a) (b) (c) (d)

Figure 5-3: (a) and (b) shows a rock material spalling off the intact rock surface, (c) and (d) shows the disintegration of the rock mass along the bedding plane in unit C and along a joint discontinuity in unit A respectively.

5.1.2. Discoloration of the rock mass

Discoloration or staining is often observed on rock mass surfaces within a short time after exposure to atmospheric conditions and weathering processes. Figure 5-4 shows the different discolorations of various regions on the studied slope with reference to the color tone of a freshly exposed surface, which shows the natural occurring color of the sandstone at the study area to be cream color (off-white) having a lighter and brighter color than a weathered surface. It is one of the first observable parameters and may be an indication of weathering process on the rock mass as noted on the Gildehaus slope, were the weathered mass has a much different color from the fresh rock surface but not a good or viable indication of the changes to the geotechnical properties of the rock mass.

(a) (b)

(c) (d) (e)

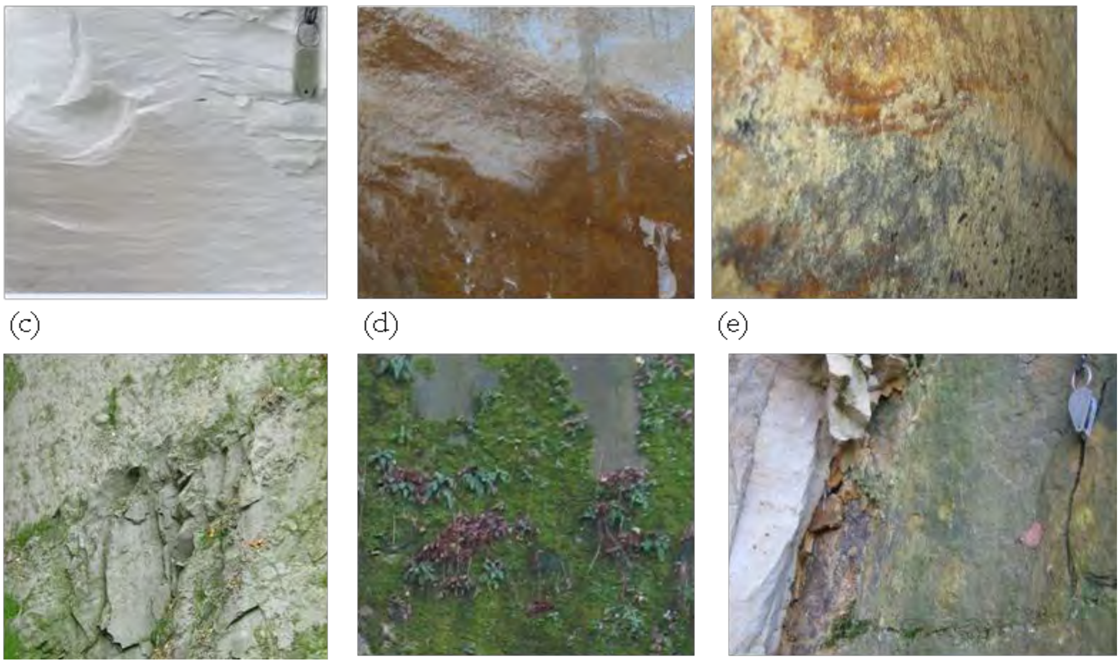

Figure 5-4: Various degrees of staining on the exposed rock mass surface with reference to a fresh rock mass (a). (b) shows discoloration as a result of oxidation, (c) shows discoloration as a result of the presence of total organic carbon, (d) shows discoloration as a result of the presence of lichens and vegetation, (e) shows a combination of the different discolorations on an exposed rock mass surface ranging from fresh to stained.

5.1.3. Oxidation

Oxidation of the studied slope at the study area is characterized by varying colours ranging from yellowish to reddish brown to blackish red intact rock and along the discontinuities. Oxidation of intact rock minerals is the influence of the presence of hematite and magnetite minerals (iron oxide/hydroxide-Fe_2O_3/$Fe(OH)_3$) produced from the react of the iron between the grain boundaries of the rock mass with water and/or air. These iron minerals are more resistant to later surface weathering and erosion than the intact rock but causes continuous oxidation of the rock mass within its interior matrix and sub-surface especially along the region of the discontinuities. This occurrence was very much observable on the unit C region of the Gildehaus slope. Figure 5-5 shows a collection of the oxidized regions captured from the exposed slope.

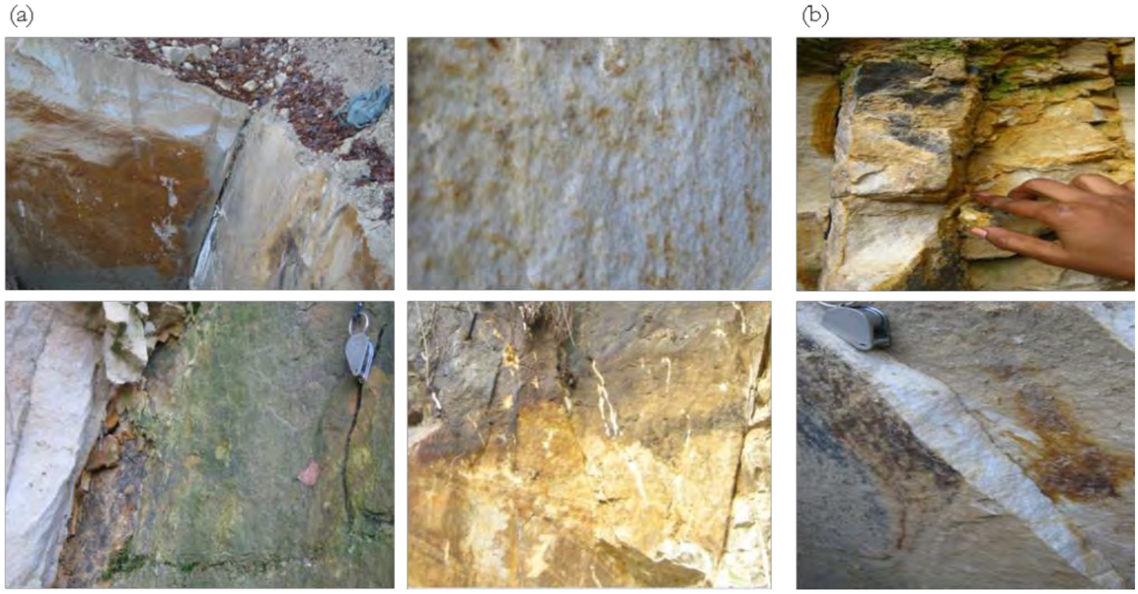

Figure 5-5: Typical oxidation of the intact rock (a) and around the discontinuities (b) showing progression into the interior matrix of sandstone rock mass.

5.1.4. Presence of vegetation and organic matter on the rock mass (lichens, moss, algae)

The presence of vegetation on the rock mass surface as a proxy for detection of weathering process has been classified into two types following the weathering grade definition of approach 2 of the BS5930:1999 (Table 5-1). The influence of vegetation was observed on the rock mass surface with the presence of clusters of lichens, algae and moss with small rooted shrubs (see Figure 5-6). The moist weather condition is likely to be an enhancing factor has it provides a conducive environment for the development of organic activities on the rock mass surface. Rooted vegetation on the surface of the rock mass and into the discontinuities have their root growth limited to a few millimetres but they are likely to grow much deeper at the uppermost part of the rock mass with the presence of completely weathered rock mass to residual soil. In addition, throughout the period of field investigation, there were observed new clustering of organic activities and small rooted plants on the rock mass.

Table 5-1: The classification of the vegetation and organic matter on the rock mass exposure.

Vegetation grade	Weathering grade	Weathering classifier	Typical characteristics of the rock exposure
I	I - II	Fresh to slightly weathered	No vegetation on rock exposure; sparse cluster of lichens, moss, algae.
II	III - VI	Moderately to highly weathered to residual soil	Presence of sparse vegetation; slightly to highly dense vegetation; clustering of lichens, moss, algae; vegetation debris.

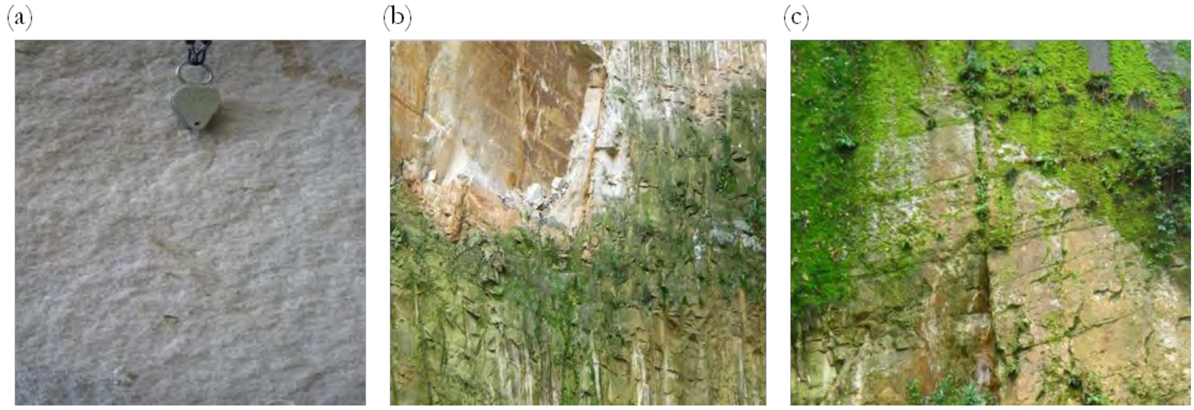

Figure 5-6: (a) A recently exposed fresh surface without the presence of vegetation and lichens, (b) Shows presence of moss and lichens, (c) Shows a relatively dense clustering of lichens, moss and vegetation.

5.1.5. Discontinuities geometry and condition of discontinuities

5.1.5.1. Discontinuity spacing and persistence

The decrease of discontinuity spacing is due to the formation of new mechanical discontinuities that become visible. The influence of weathering action on the formation of new discontinuities is mainly pronounced in the reduction of the spacing for all discontinuity sets with increasing weathering grade (Figure 5-7). In most sandstone rock mass, the bedding planes that form the mechanical discontinuities are usually persistent. The persistence of the bedding planes is usually controlled by the thicknesses of the original strata, with the mechanical discontinuity geometry at any one place in the same unit with the same weathering grade being the same. A limitation however may arise from the development of integral discontinuities into mechanical discontinuities, which may not be uniform and continuous along the whole discontinuity surface. Thus, there is the possibility of a bedding plane having become a mechanical along a plane to still exhibit as an integral discontinuity at other locations along the same plane (Figure 5-7). The results of the field investigation carried out show the bedding planes on the rock mass as having spacing ranging from 60 to 200mm and from 200 to 600mm.

Figure 5-7: The orientation of the discontinuities sets (3Nos bedding and 2Nos joint system)in the studied slope.

The 200 to 600mm bedding plane spacing starts from the toe of the rock mass to about 5m above with a high continuous persistence value of 10 to 20m terminating against the joint discontinuities. This region represents the medium to thickly bedded unit in the sandstone, and is assumed to be responsible for the large blocks of rock mass excavated from the Gildehaus slope involving the use of a pneumatic hammer and type of chemical "pre-splitting" excavation technique. The joint system on the rock mass surface have a wide spacing of 600mm to 2m with a high continuous persistence value of 10 to 20m.

5.1.5.2. Development of integral discontinuity to mechanical discontinuity

The variation in the environmental condition of the study area encourages the influence of weathering action on the formation of new discontinuities resulting from the repeated heating and cooling of the rock exposure. Figure 5-8(b) below shows the formation of new mechanical discontinuities in unit C induced by physical weathering. Tating (2015) citing Hencher and Knipe (2007) and Huisman et al., (2004) mentioned the possibility of the formation of integral discontinuities due to the presence of invisible internal structures or as a result of the different elastic response of adjacent minerals grain to changes in the geological environment, such as loading and unloading during wetting and drying of the rock mass. This latter statement is much more in line with the condition of the studied slope.

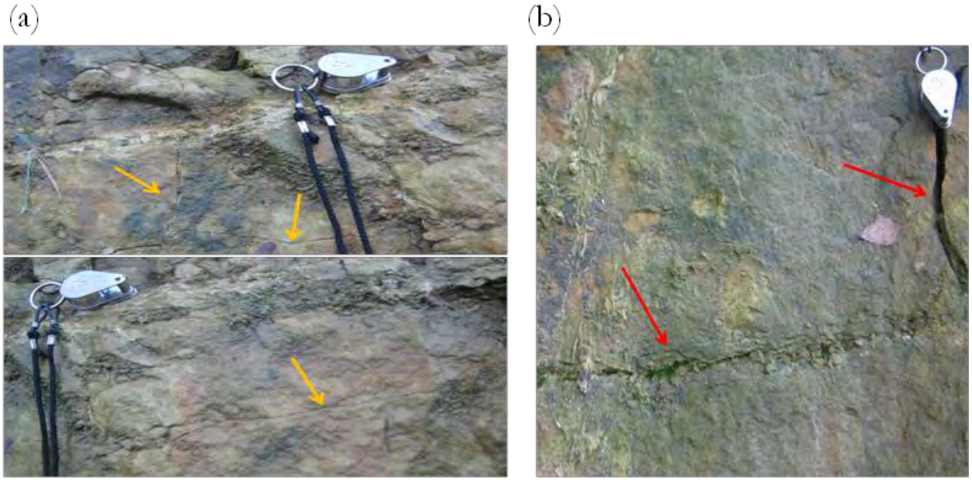

Figure 5-8: Development of integral discontinuities into mechanical discontinuities. (a) Yellow arrow indicates position of the developing integral discontinuities. (b) Red arrow shows the location of newly formed and now clearly visible mechanical discontinuites.

5.1.5.3. Discontinuity roughness, aperture and infill material

The bedding and joint discontinuities have a large-scale roughness of slight curvature independent of the weathering grade. The small-scale roughness is mostly "rough undulating" in weathering grade fresh to slightly weathered masses and becomes "smooth undulating" in more weathered regions. This is consistent to what is expected as mostly, small-scale roughness becomes smoother due to the deterioration of asperities as a result of the progressive weathering (Geertsema, 2003). However contrary to this, there is the possibility for roughness to increase with increasing degree of weathering if chemical weathering is dominant and there is an abundance of precipitation of iron hydroxide and other iron compounds along the discontinuities (Tating, 2015). This phenomenon was not noticeable on the studied exposure surface but there was the precipitation of iron compound coatings on the surfaces of the rock mass resulting in rough surfaces and sometimes in completely cemented discontinuities as observed on the unit C, a unit classified as moderately to highly weathered sandstone. This is consistent with a statement by Tating (2015) that the iron-coated or cemented discontinuities are mostly found in areas with moderately to highly weathered sandstone more than in sandstone masses with a lower degree of weathering. As shown in Figure 5-9, the infill material noticed between the discontinuities is as a result of the weathering of the discontinuities walls and the high possibility of the washing of particles and debris into the discontinuities, but it is unlikely the major source especially for the infill material noticed between the bedding planes but it can be concluded to be the major source of the deposited at the foot of the rock mass. It was also observed that un-cemented discontinuities are mostly filled with fine-grained soft sheared (clayey) material that are probably as a result of the weathering process acting on the rock mass and these discontinuities have been detected to have a "smooth undulating" small-scale roughness with a high degree of weathering. The aperture (openness) of the bedding planes are rather very tight less than 2mm while the joint system has a tight aperture ranging from 0.1mm to 0.5mm. There was noticeable falling of debris from the upper part of the Gildehaus slope in unit B over the rock mass surface.

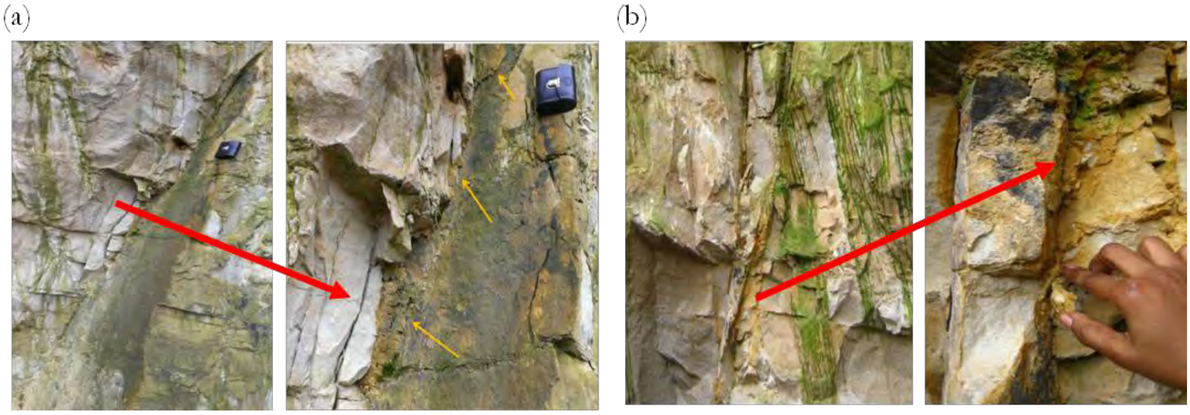

Figure 5-9: (a) The presence of fine soft sheared material along the joint discontinuity bordering unit B, (b) The presence of fine non-softening or sheared material along the joint discontinuity in unit A. The red arrow shows the position of the area of interest zoomed in on, while the yellow arrow indicates the visible infill material between the discontinuity.

5.2. Laboratory analysis of the rock samples from the studied slope

5.2.1. Mineral composition and clay mineralogy analysis

As mentioned before, the analyses of the rock samples using the powder XRD was to determine the possibly presence of certain minerals indicative of the occurrence of chemical weathering process in a rock mass. The evidences found that support the proposed methodology are presented below.

5.2.1.1. Mineral composition

The results of the laboratory mineralogy tests conducted on representative fraction of the rock samples are presented using the pattern fitting method, which scales the experimental digital pattern shown in colours to the reference simulations shown in black. This method is deemed to give better results has it includes all minor phases and it is preferred for analysis including amorphous (that is non crystalline) components (ICDD, 2015). The results indicate that all the samples comprises mostly of quartz showing very sharp peaks at 20.85, 26.7, 36.5, 39.5, 42.4, 50.1, 60.05, 68.45 (2-theta) with amounts of kaolinite clay minerals having peaks at 12.3, 24.85, 54.95 (2-theta), hematite at 24.3, 54.25, 62.75, 64.2 (2-theta) and magnetite with peaks at 35.45, 57.2, 62.75 (2-theta), the diffractogram below show the XRD patterns of sample A1 (fresh) in Figure 5-10 (see Appendix 5a). The samples also contains compounds of feldspars in minor amounts of muscovite with peaks at 23.05, 45.55 (2-theta), a very common mineral in most rock types, also jadeite, tourmaline and gypsum with peaks at 40.6, 47.3 and 20.8 (2-theta) respectively. Other varieties of quartz (that is other crystalline polymorph of silica- SiO_2) were detected, they are beryl ($Al_2Be_3(Si_6O_{18})$) and Titanite ($CaTiSiO_5$) with peaks at 45.55 and 65.7 (2-theta) respectively. The high intensity percentage of the quartz in the sandstone rock mass is consistent with the chemical composition analysis carried out on the Bentheim sandstone, which states quartz has the main constituent of the sandstone making up to >90% of the rock mass (Dubelaar et al., 2015).

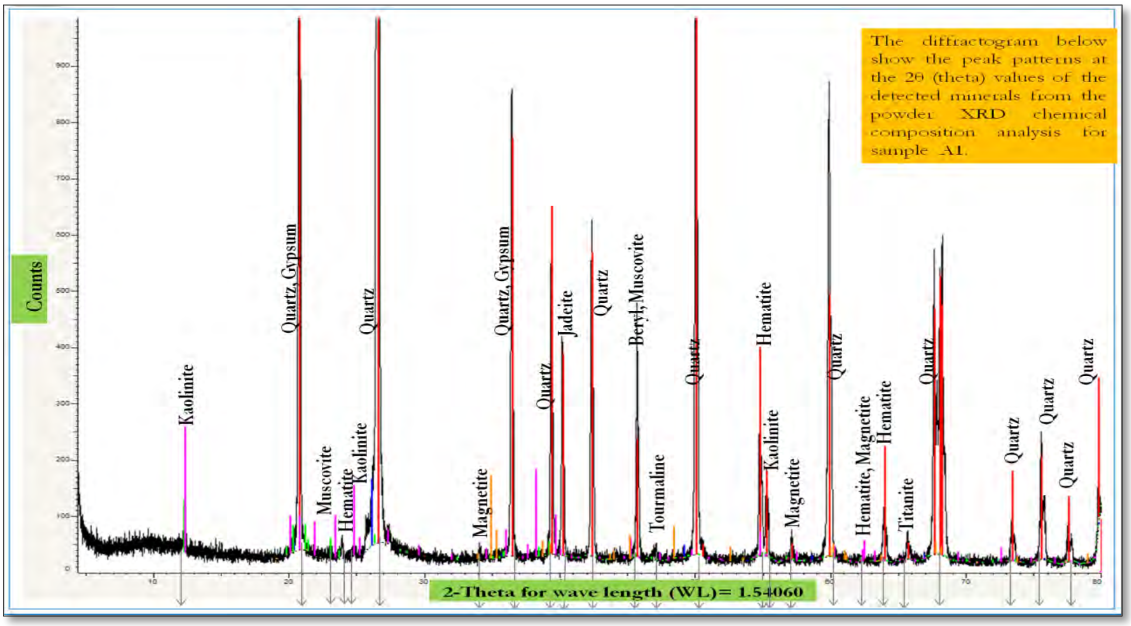

Figure 5-10: X-ray diffractogram (XRD) for sample A1 from unit A, Gildehaus Slope (the arrow lines below the peaks have no meaning and are only for identification).

The intensity percentage (I%) values were derived from the DIFFRAC.EVA software which was used to carried out the phase identification and accurate quantitative phase analysis unique to each mineral based on the reference intensity ratios (RIR) values (Bruker Corporation, 2016). Table 5-2 shows a list of the minerals and the corresponding I% values derived from the rock samples tested. As observed, the I% of the hematite mineral is much lower in unit B which is to be expected as the surface area where the samples were collected are covered by the presence of total organic carbon, but this is compensated for by the intensity percentage values of the magnetite which is more of a penetrative oxidation.

Table 5-2: The intensity values of the phase identification in percentage. The scanning covered a 2-theta range of 4.5° to 25° with a step size of 0.006 degrees and a 2-second count time per step to highlight the presence of the minor phases overshadowed by the high quartz content in the rock samples.

Samples	Phase (minerals)			
	Quartz (I%)	Kaolinite (I%)	Hematite (I%)	Magnetite (I%)
Sample A1 (Fresh)	100 (low)	6	100	100
Sample A2 (Fresh)	19 (low)	1	4	100
Sample B1	5 (low)	2	2	100
Sample B2	14 (low)	1	2	100
Sample B (Residual)	100 (low)	12	9	56
Sample C1	14 (low), 100 (high)	10	100	100
Sample C2	100 (low)	12	100	100

***Quartz-tridymite-cristobalite group (atmospheric and low pressure) is a crystal structure of Silica (SiO_2).** **- Low (α)-quartz - Trigonal**; **- High (β)-quartz - Hexagonal**

Quartz (Trigonal low-temperature alpha-quartz) is the most important silica modification in nature due to it pure crystal structure and also most frequently used in technical applications.** ***Source: *Götze (2012)*

5.2.1.2. Clay mineralogy

The pipette test method results follow the same analysis as the mineral composition (see Table 5-3). Due to the preparation steps carried out on the rock samples, though the quartz phases were still clearly observable at 20.85, 26.7, 42.4, 50.1, 60.05 (2-theta), there were noticeable increase in the peak frequency and intensity percentage for the minor phase of the kaolinite clay minerals present in the rock samples, showing very sharp peaks at 12.3, 24.85, 34.9, 35.9, 54.95 (2-theta). Also noticed in the phase identification results, were the presence of hematite at 24.3 (2-theta), beryl at 45.55, 19.3 (2-theta), titanite at 18 (2-theta), muscovite at 8.9, 45.55, 61.8 (2-theta), gypsum at 20.8, 29.15, 31.15, 36.05 (2-theta), as well jadeite and tourmaline showing peaks at 37.15 and 14 (2-theta) respectively. Figure 5-11 shows the peaks of the phase identification of the minerals present in the rock sample B(Residual) (see Appendix 5b).

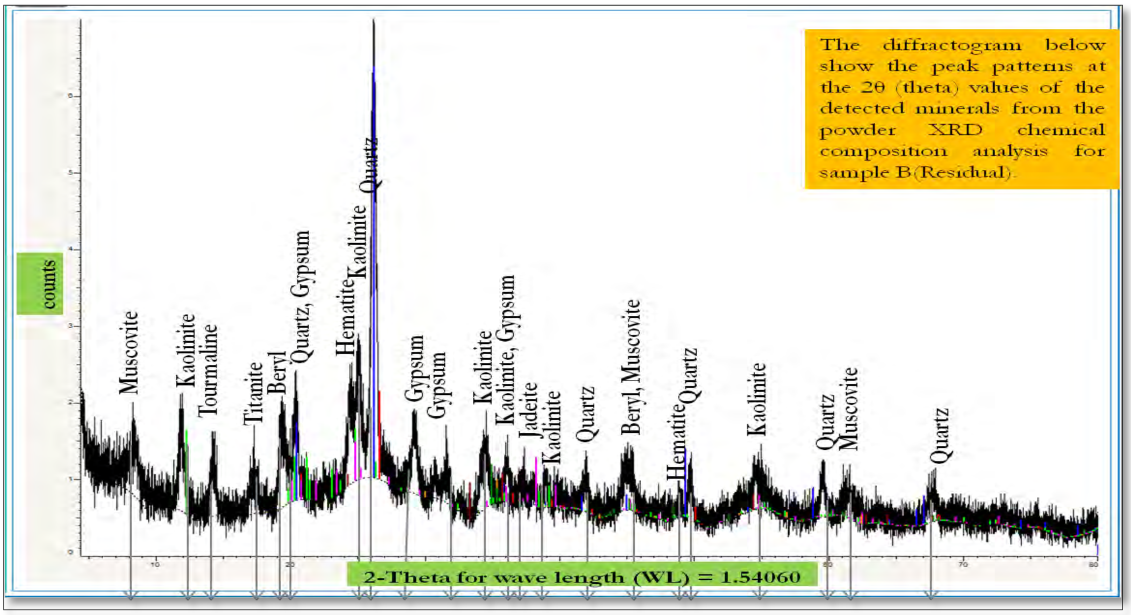

Figure 5-11: X-ray diffractogram (XRD) from the pipette test method for sample B(Residual) from unit B, Gildehaus slope (the arrow lines below the peaks have no meaning and are only for identification).

Table 5-3: The pipette test analysis showing the level of accuracy of identification in percentage using the RIR approach

Samples (Pipette test)	Phase (minerals)			
	Quartz (I%)	Kaolinite (I%)	Hematite (I%)	Magnetite (I%)
Sample A1 (Fresh)	84 (low)	64	4	9
Sample B (Residual)	18 (low), 83 (high)	17	7	8
Sample C2	12 (low), 84 (high)	16	12	11

5.2.1.3. Discussion

As a construction material and for engineering purposes, sandstones have been used and are still being used worldwide for this purpose, although most sandstones show similar appearances and properties, the effects of chemical weathering may cause differences in its geotechnical and granulometric properties, which can be predicted using the mineralogical properties of the sandstone (Mubiayi, 2013). The XRD analysis was focused on the determination of three major minerals namely quartz, clay minerals and iron oxides/hydroxides. This choice is supported by Boggs (2009) who stated that the effect of chemical weathering on a sedimentary rock leads to the concentration of resistant residues consisting mainly of quartz minerals, the formation of secondary minerals such as clay minerals and iron oxides as shown in Table 5-2. In addition compounds of elements such as calcium, potassium, sodium, magnesium and silica are leached away from the rock mass and are likely present in rich constituent in the weathered products. Supporting this statement is the XRF results (Table 5-4) indicating the presence of minor amounts of feldspar showing high concentration level for both calcium and potassium in sample B(Residual) and also high concentration of potassium in the unit A sample 3 which can be justified as being the presence of potassium oxides in the fresh rock sample not yet released by weathering processes.

The XRD analysis results indicates the dominant presence of quartz with considerable amounts of iron oxides and minor of clay minerals. The presence of quartz in the mineral composition analysis is an expected occurrence as it is naturally abundant in most sedimentary rocks and is the least susceptible mineral to weathering on exposure to the surface (Mulenga, 2015). The high intensity percentage of the analysed sample C1and C2, and the sample B (Residual) support the results and the opinion that due to its relative resistance to chemical weathering process, there is a high likelihood for the presence of abundance of quartz minerals on the rock mass surface after the leaching away of the binding cement minerals holding the quartz grains together, as a result of the weathering process the rock mass has been exposed to. The high intensity percentage of the fresh rock sample A1 is representative of the very sharp peaks at all the phases unique to the presence of quartz, but this is a sharp contrast to the relatively very low intensity percentage value of the Trigonal low-temperature alpha-quartz (it indicates the crystal structure of pure quartz) of sample A2, which can be attributed to the presence of moisture on the rock mass surface as a result of the environmental conditions during collection, presence of contaminants on the rock sample, interference among the elements, or analytical error during analyses. However, the high intensity percentage value of the Hexagonal high-temperature beta-quartz (it indicates the crystal structure of the defect pure quartz influenced by the presence of other minerals, that are mostly fine-grained and intimately inter-grown with the natural quartz to form another variety of quartz) is still consistent, albeit a contaminated form of quartz.

The XRD analysis results revealed that Kaolinite ($Al_2Si_2O_5(OH)_4$), a clay mineral and a product of chemical weathering, was present in all the sandstones. This finding is supported by the tests carried out on the Bentheim sandstone at the Gildehaus quarry by Mansurbeg (2001) and Klein et al. (2001) in which they described in detail that the Bentheim sandstone is relatively homogeneous, with mean composition of 95% quartz, 3% kaolinite and 2% orthoclase. The presence of the kaolinite indicating two likely conditions, that first, the rock mass has clay minerals as part of the cementing material between the quartz grains or second, it has already been subjected to chemical weathering. The high intensity percentage value of the fresh rock sample A1 in the pipette test is quite consistent with the first condition of the presence of clay minerals in the binding material of the rock mass. This is justifiable by the field geologic investigation carried out, which states the presence of trace clay minerals found with the grains of the sandstone. Due to the well known difficulties inherent in the quantitative analysis of clay minerals, such as variable degrees of structural order or disorder, compositional variation, and their tendency towards preferred orientation in a powder sample, has given rise to a general and quite justifiable perception that the results acquired from the XRD analysis are often semi-quantitative at best (Brindley, 1980 cited in Hillier, 2000). Also, the use of XRD to determine and measure the clay minerals in sandstones are often compounded by the fact that the total clay mineral content is most commonly only a very small fraction of the whole test sample which tends to be dominated by other phases, notably quartz (Hillier, 2000). This has necessitated the use of the pipette analysis method, where the increase in peak frequency and intensity percentage of kaolinite and high (β)-quartz in samples B and C support the second condition that the rock mass has been subjected to chemical weathering. The intensity percentage results of the iron minerals (hematite and magnetite) in the pipette test are more subdued, possibly due to the washing out of the iron minerals from the rock samples during sample preparation.

5.2.2. Results from the XRF Analysis

The spectral analyses for the detection of minerals such as Iron (Fe), Quartz (silica), carbonate compounds/oxides of Calcium (Ca), Sodium (Na), Magnesium (Mg) and Potassium (K) were carried out in accordance with the method outlined in chapter 4.5.1.1. Table 5.4 shows the list of the composition elements identified in the rock mass but it should be noted that the elements occur naturally in their oxides or in combination with other elements. There are various other elements present in trace amounts (see Appendix 6) with the concentration for iron being the highest in regions with visible discoloration caused by oxidation on the rock sample but with lower iron concentrations in the fresh rock samples, Figure 5-12 was used to visually inspect the data to reveal the differences between the measured samples.

Table 5-4: Summary of the elements concentration estimates and the inherent analytical error associated with the estimates

SAMPLE	**Fe (ppm)**	**Fe %**	Fe Error %	**Ca** (ppm)	**Ca %**	Ca Error %	**K** (ppm)	**K %**	K Error %
NWG-01 (test sample)	**81001**	**8.10**	0.05	**75043**	**7.50**	0.06	**9498**	**0.95**	0.03
Where S - Surface, ppm - parts per million, Fe (%) = Fe/10000									
Unit A (Fresh)- S1	**388**	**0.04**	0.00	**137**	**0.01**	0.00	**4711**	**0.47**	0.01
Unit A (Fresh)- S2	**360**	**0.04**	0.00	**89**	**0.01**	0.00	**3298**	**0.33**	0.01
Unit A (Fresh)- S3	**1652**	**0.17**	0.01	**87**	**0.01**	0.00	**8917**	**0.89**	0.01
Unit B (Oxidized)- S1	**58836**	**5.88**	0.04	**302**	**0.03**	0.01	**3487**	**0.35**	0.02
Unit B- S2	**713**	**0.07**	0.00	**188**	**0.02**	0.00	**3943**	**0.39**	0.01
Unit B (Residual)- S3	**5858**	**0.59**	0.01	**767**	**0.08**	0.00	**8197**	**0.82**	0.01
Unit C- S1	**1507**	**0.15**	0.01	**347**	**0.03**	0.00	**5795**	**0.58**	0.01
Unit C- S2	**1113**	**0.11**	0.00	**159**	**0.02**	0.00	**4794**	**0.48**	0.01
Unit C (Oxidized)- S3	**66700**	**6.67**	0.04	**489**	**0.05**	0.01	**4768**	**0.48**	0.02

5.2.2.1. Discussion

Sodium and magnesium were not detected from the rock samples analysed as a result of the limitation of the portable XRF analyser, as the rock samples needed to be prepared carefully in a controlled and consistent manner using the helium flush for the equipment to be able to analyse them accurately even down to a concentration level of +/-0.01%. The limitation of the XRF is due to its ineffectiveness in detecting common elements considered to be "light" elements, such as lithium, beryllium, sodium, magnesium, aluminium, silicon, and phosphorus (EPA, 2008). The XRF result is consistent with the chemical analysis (atomic absorption spectrophotometry- AAS) carried out by Mansurbeg (2001) used to determine the elements concentrations of Potassium (K), Calcium (Ca), Sodium (Na) and Aluminium (Al) present in the Bentheim sandstone. The atomic absorption spectrophotometry depends on electron transitions between distinct energy levels within the electron shells of the atom in the solution under analysis where by each of the specific elements absorbs light at a characteristic set of wavelength. The results from the analysis confirms potassium (K) feldspar has the main feldspar with higher concentrations than the calcium (Ca) feldspar similar to the results of the XRF analysis carried out. He also mentioned the possibility of the presence of small amounts of sodium (Na) or the likely admixture of sodium compound within the potassium feldspar as the two elements have a high positive correlation. The same can be said for the presence of magnesium in the rock sample, following a rule of thumb that says the presence of calcium in the rock samples is a good indicator that magnesium compound is also present. This is due to the high possibility that the magnesium could be admixed within the calcium feldspar.

Nijland et al. (2003), from the whole rock chemistry of the Bentheim sandstone carried out, mentioned that the results showed total iron contents and oxalic acid soluble iron has been highly present in the weathered layers analysed and increases as the weathering process increases. They also mentioned that there was noticeable increasing mobility of the iron minerals during the enrichment process in the weathering layers as well as the presence of trace heavy metals such as Lead (Pb), Zinc (Zn) and Tin (Sn) contributing to the effect of black weathering on the rock mass. Thus, it can be surmised from the results of the XRD and XRF analyses, that the rock mass has been influenced by chemical weathering.

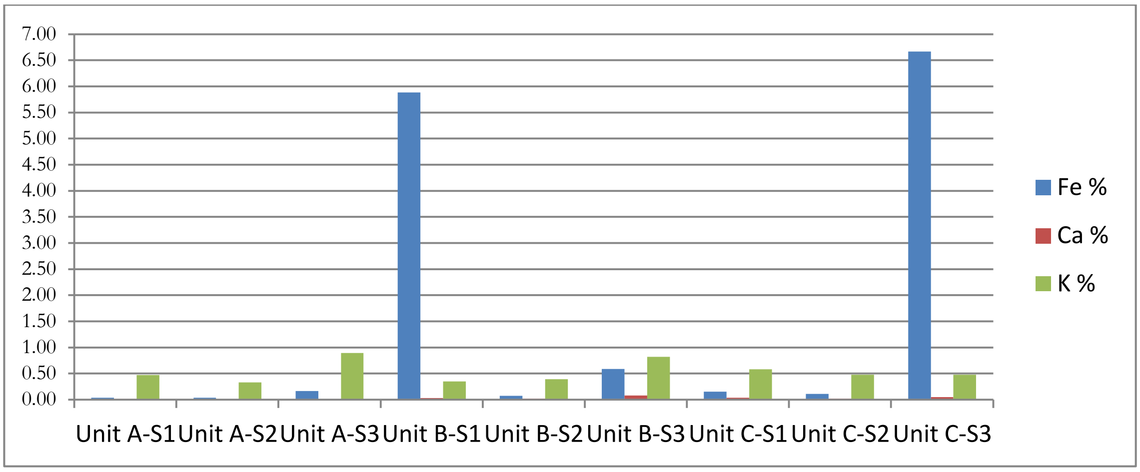

Figure 5-12: Column chart for visualization of the concentration (%) of the minerals in the rock samples.

5.2.3. TIR (Emissivity) analysis results of the rock samples

The eight spectrums for each sample were averaged into a single spectrum and mineral identification was carried out using the ENVI spectral analyst and reference spectral library from JPL and JHU (the reference spectral are collected from relatively pure mineral sample). The spectral absorption features in the Mid wave Infrared (2.1-5.2µm) and TIR (7-12µm) regions were both used for interpretation, by identifying minerals with spectral features at observed wavelength from literature. Two minerals were identified, they are quartz with characteristic doublet absorption features at ~8 - 9.2µm and another at ~12.5 - 12.7µm (Figure 13a), as well as kaolinite with absorption features at ~2.2 and also at ~2.7 to 2.8µm (Figure 13b).

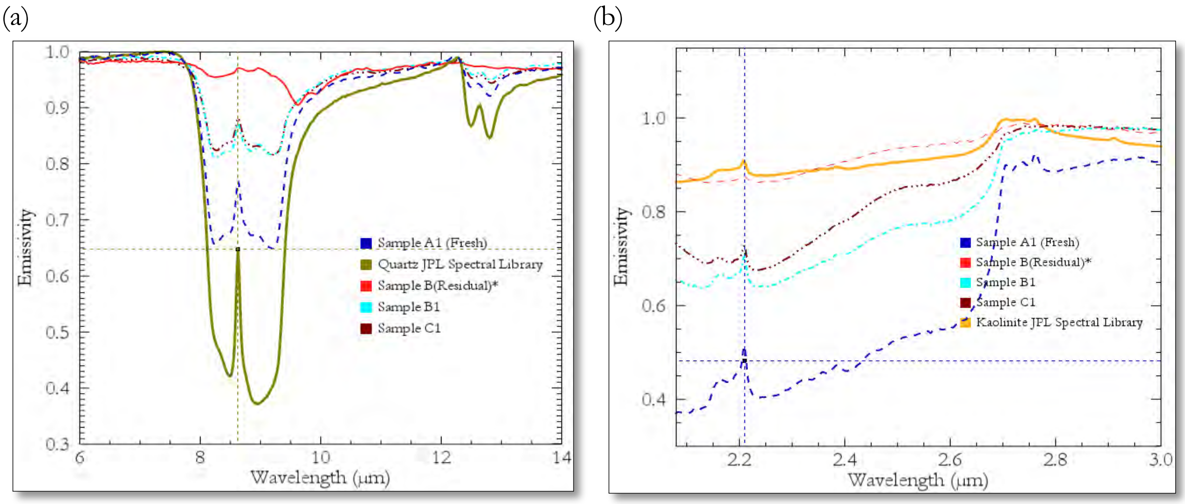

Figure 5-13: Emissivity spectra for quartz (a) and kaolinite clay mineral (b).

The sample B(Residual) shows a high emissivity feature for quartz due to the low concentration of quartz and dark spectral property of the rock sample in comparison to the fresh rock sample and the reference spectral, this is supported by Gupta (2003) who stated that silica has a low emissivity. The fresh rock sample also exhibits some feature in the doublet at ~9.2µm, which shows some traces of other minerals present that has likely inter-grown with the silica crystal structure of the natural quartz. The rock samples other than the fresh rock sample, exhibit a lower reflectance due to the dark colour and a higher emissivity as supported by literature (Chapter 2.2.6, 2.4.2.2). All the rock samples tested exhibited absorption features for the presence of clay minerals including the fresh rock sample although with a very low emissivity value of less than 0.4, with the sample B(Residual), taken from the final weathered products at the foot of the Gildehaus slope having the highest emissivity at ~0.9. This supports the likely occurrence of chemical weathering process on the rock mass. The presence of water in the rock samples is an added indication of chemical weathering has observed from the differences in the reflectance values of the same spectra taken of the samples B and C due to the drying out of moisture from the rock samples during the cause of the FTIR measurement.

5.2.4. Factual description and weathering classification of the studied slope

The studied slope has a total exposure size of approximately 15m height with another 8m layer of clay horizon underneath the total exposure (Traska, 2014) and 20m depth (wideness in scope).The section mapped for the detailed small scale study ranges approximately 10m length and 2m height above the toe of the rock mass to detect in individual weathering signatures, while weathering signatures such as coloration of the rock mass, presence of vegetation and organic activities, discontinuity geometry were also detectable on a larger scale for the whole slope exposure. The result of the geological field description, chemical analysis and weathering classification carried out on the Gildehaus slope is shown in Table 5-5. Blue cells represents parameters detectable within a small scale spatial resolution of less than 50mm, while red cells represents parameter detectable within both a small scale and large scale spatial resolution of greater than 50mm. Yellow cells represent the weathering classification of the geotechnical units.

5.2.4.1. Discussion

The discontinuity sets, **B-II** - 20 /180 from unit B and have **B-III -** 15 /294 from unit C were expected to have similar discontinuity geometry although the angle of dip are quite close in value, but the high variation of the dip direction can be attributed to the geo-morphological folding of the rock mass over time from continuous applied crustal forces and uplifting as well as the interact of the two joint systems relative to each other. The high value of the intact rock strength of unit B and C in relation to that of unit A can be attributed to the adverse effect of weathering occurring mostly along the plane of weakness as well as the influence of the mineral content affecting the geo-mechanical properties of Bentheim sandstone. According to Mubiayi (2013), who reported that rocks containing quartz, calcite and ferrous minerals as binding materials are the strongest materials in the order mentioned while rocks with clayey binding materials are the weakest materials. From the simple test and sounding analysis carried out in addition to the geologic investigation, a strong assumption can be made that the strength of the Gildehaus slope can be attributed to the binding material, silica or siliceous quartz between the grains. The presence of calcium from the XRF analysis results (see Table 5.4) with the highest concentration of 0.08% present in the sample B (Residue) however, indicates the likely presence of calcite as part of the binding material, cementing together the quartz grains of the sandstone, which was deposited by erosional processes at the foot of the rock mass in unit B as a result of weathering process in the unit.

Akhavan (2015) mentioned that largely the weathering process occurring in a quartz rich rock mass in an oceanic climate, as is the case of the climatic condition at the Gildehaus quarry, is mostly due to physical weathering forces and processes such as changes in temperature, erosion, cracking by ice-wedges, and grinding of the grain minerals against each other or abrasion form the effect of strong wind. He attributed this to the presence of abundant quartz minerals formed on the surface of the rock mass as a result of the decomposition and wearing away of the cementing minerals that filled out the voids between the grains leaving the quartz behind. This is supported by the sharp peaks and intensity percentage of the phase identification and accuracy indicating a very strong presence of quartz minerals in the rock samples analysed using the XRD during the mineral composition and clay mineralogy tests (see Chapter 5.2.1).

Table 5-5: Exposure characteristics and weathering classification of the geotechnical units after the SSPC following Approach 1and 2 of the BS5930:1999 and the chemical analysis of the rock samples.

Unit A	Unit B	Unit C
▪ **Grain size**- 0.06 to 0.2mm. ▪ **Structure**- ranges from medium (200-600mm thickness) to thickly bedded (600mm-2m thickness). ▪ **Texture**- Clastic (cemented with silica or siliceous quartz with traces of clay). ▪ Intact rock strength of 100MPa.	▪ **Grain size**- 0.002 to 0.2mm ▪ **Structure**- Medium (200-600mm thickness) to thickly bedded (600mm-2m thickness). ▪ **Texture**- Clastic (cemented with silica or siliceous quartz with presence of clay) ▪ Intact rock strength of 75MPa (reduction)	▪ **Grain size**- 0.06 to 0.2mm ▪ **Structure**- Medium (200-600mm thickness) to thickly bedded (600mm-2m thickness). ▪ **Texture**- Clastic (cemented with silica or siliceous quartz with traces of clay) ▪ Intact rock strength of 75MPa (reduction)
▪ **Color**- White(cream) to light reddish yellow & reddish brown resulting from early oxidation	▪ **Color**- Dark grey to dark greyish green resulting from the presence of total organic carbon.	▪ **Color**- Reddish brown to greyish green resulting from oxidation and total organic carbon.
▪ Presence of fresh exposure on the rock mass surface.	▪ Presence of lichen and sparse vegetation.	▪ Presence of clusters of lichen and vegetation.
▪ **Discontinuity geometry-** **B-I** - 28 /188 Spacing- 0.22m Persistence- continuous	▪ **Discontinuity geometry-** **B-II** - 20 /180 Spacing- 0.25m Persistence- continuous	▪ **Discontinuity geometry-** **B-III -** 15 /294 Spacing- 0.25m Persistence- continuous
▪ **Condition of discontinuity-** Roughness (Rl)- Slightly curved Roughness (Rs)- Rough undulating Aperture- Very tight less than 2mm Infill- Soft sheared material (fine) No presence of Karst	▪ **Condition of discontinuity-** Roughness (Rl)- Slightly curved Roughness (Rs)- Smooth undulating Aperture- Very tight less than 2mm Infill- Soft sheared material (fine) No presence of Karst	▪ **Condition of discontinuity-** Roughness (Rl)- Slightly curved Roughness (Rs)- Smooth undulating Aperture- Very tight less than 1mm Infill- Cemented material No presence of Karst
J-I - 65 /10 Spacing- ~4.5m Persistence- continuous	**J-I -** 65 /10 Spacing- ~4m Persistence- continuous	**J-II -** 80 /107 Spacing- ~10m Persistence- continuous
Roughness (Rl)- Slightly curved Roughness (Rs)- Rough undulating Aperture- Tight (0.1mm to 0.5mm) Infill- Non softening or sheared material (fine) No presence of Karst	Roughness (Rl)- Slightly curved Roughness (Rs)- Smooth undulating Aperture- Tight (0.1mm to 0.5mm) Infill- Soft sheared material (fine) No presence of Karst	Roughness (Rl)- Slightly curved Roughness (Rs)- Rough undulating Aperture- Very tight less than 1mm Infill- Cemented material No presence of Karst
J-II (measurements were taken at the joint face) Spacing- ~10m Persistence- continuous	**J-II -** 80 /107 Spacing- ~10m Persistence- continuous	**J-I (measurements were taken at the joint face)** Spacing- ~4m Persistence- continuous
Roughness (Rl)- Slightly curved Roughness (Rs)- Rough undulating Aperture- Very tight less than 1mm Infill- Cemented material No presence of Karst	Roughness (Rl)- Slightly curved Roughness (Rs)- Rough undulating Aperture- Tight (0.1mm to 0.5mm) Infill- Soft sheared material (fine) No presence of Karst	Roughness (Rl)- Slightly curved Roughness (Rs)- Smooth undulating Aperture- Tight (0.1mm to 0.5mm) Infill- Soft sheared material (medium) No presence of Karst
▪ **Chemical analysis** Trace amounts of clay mineral. Trace amounts of Hematite. Trace amounts of Magnetite. Very high indication of trigonal Quartz (i.e. Pure Quartz). Trace amounts of Feldspar (Ca, K). No indication of moisture (Water). Low emissivity of ~0.65 for Quartz and ~0.4 for Kaolinite.	▪ **Chemical analysis** Presence of clay mineral. Presence of Hematite. Presence of Magnetite. High amounts of Hexagonal Quartz with low amounts of trigonal Quartz Presence of Feldspar (Ca, K) Indication of moisture (Water). High emissivity of ~0.85 to 1.0 for Quartz and ~0.7 to 0.9 for Kaolinite.	▪ **Chemical analysis** Presence of clay mineral. Presence of Hematite. Presence of Magnetite. High amounts of Hexagonal Quartz with low amounts of trigonal Quartz Presence of Feldspar (Ca, K). Indication of moisture (Water). High emissivity of ~0.85 for Quartz and ~0.75 for Kaolinite.
▪ **Weathering classification** Fresh to Slightly weathered.	▪ **Weathering classification** Moderately to highly weathered.	▪ **Weathering classification** Moderately to highly weathered.

5.3. Assessment of the detectability of the weathering signatures from UAV-based and TLS dataset

The analyses for the possible detection of the weathering signatures from the UAV-based and TLS point cloud datasets follows the methodology given in Chapter 4.4. The result derived is presented below.

5.3.1. Estimation of the agreement and variation between the UAV-based and TLS point cloud datasets

Cloud to cloud comparison was first carried out on the two dataset according to the methodology stated out in Chapter 4.4.2.3 to estimate the agreement and deviation between the two measurements. The agreement and differences are displayed as a color map of the study area (Figure 5-14). This gives a visual and statistical indicator of the deviation between the UAV-based point cloud data and the TLS point cloud data ranging from 0m -1m (max distance). The results from the cloud to cloud comparison are similar using both the 6 and 8 number of neighbouring points. The surfaces on the color map reflected as blue, show the agreement with 0m distance between the two point cloud datasets. The vegetation covering both adjacent part of the rock mass surface in the UAV-based data, reflecting as red gives the greatest distance variation of 1m, which is expected has they were not captured by the TLS during the scanning of rock surface. The toe of the Gildehaus slope reflecting as yellow, shows a distance variation between the range 0.625m to 0.875m. Zooming into the region shows this is likely as a result of the densification of the UAV-based point cloud, which provides point data for regions in the TLS point data with spaces as a result of the placement of the TLS-based points at a constant regular interval. This method helps to evaluate the level of statistical uncertainty between the two datasets and shows the variation as well as the relative position of the variation between the datasets in their use for the detection of weathering signatures. It also provides the user with the means to estimate the level of the accuracy and precision of the UAV-based point cloud to the TLS point cloud in the extraction of information as it influences the acceptance of the quality of results generated.

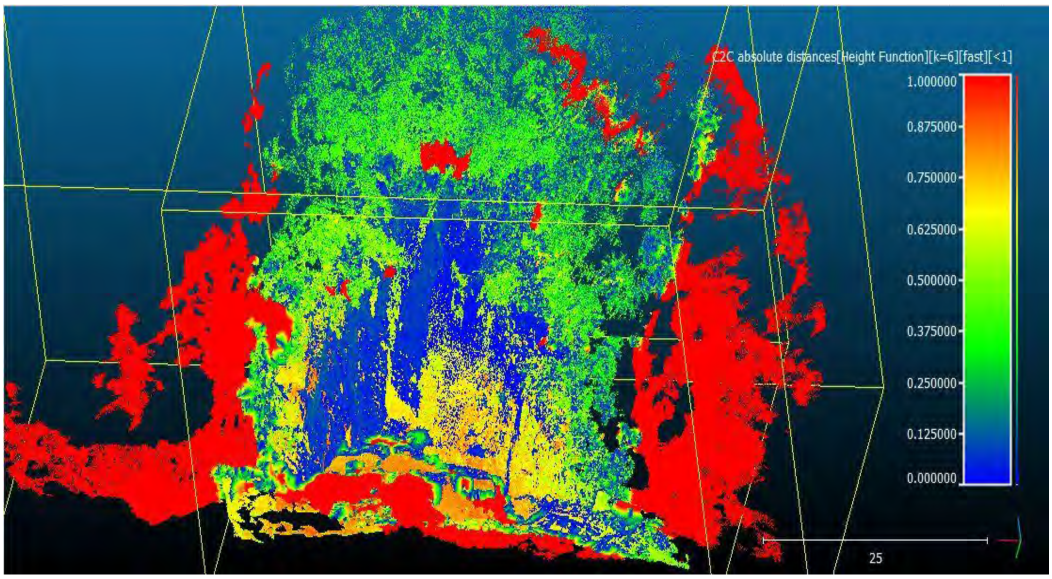

Figure 5-14: Cloud to cloud comparison of the UAV-based and TLS datasets using 6 neighbouring points. Shows the largest variation of the overlapped data at the vegetated areas of the UAV-based point cloud.

5.3.2. Extraction of vegetation and organic matter as weathering signatures from the point cloud data

The excess green (ExG) vegetation index was first carried out on a visible image from the UAV-based images to verify its applicability in extracting all vegetation and the organic matter captured in the image. The result of its application on the UAV-based and TLS 3D point cloud datasets shows that the vegetation index was reliable in the quantification of all possible vegetation on the rock mass surface including areas with very sparse vegetation, giving a unit value of 0 to all the points without vegetation and a unit value of 1 to all the points with vegetation as displayed in the color bar in Figures 5-15a-b. This has encouraged the level of confidence in the results acquired from the operation of the ExG vegetation index on the UAV-based and TLS point cloud datasets. The results are supported by Torres-Sánchez et al., (2014) where they concluded that the ExG vegetation is one of the best vegetation indices capable of achieving the best accuracy in its use for vegetation mapping. The results of the extracted vegetated areas in the UAV-based point cloud data are quite comparable to TLS point cloud data. The yellow regions in Figures 5-15a-b represents the vegetation and organic matter on the rock mass, while the blue regions represent the non-vegetation regions on the rock mass as supported by the original point cloud datasets.

(Fig 5-15a)

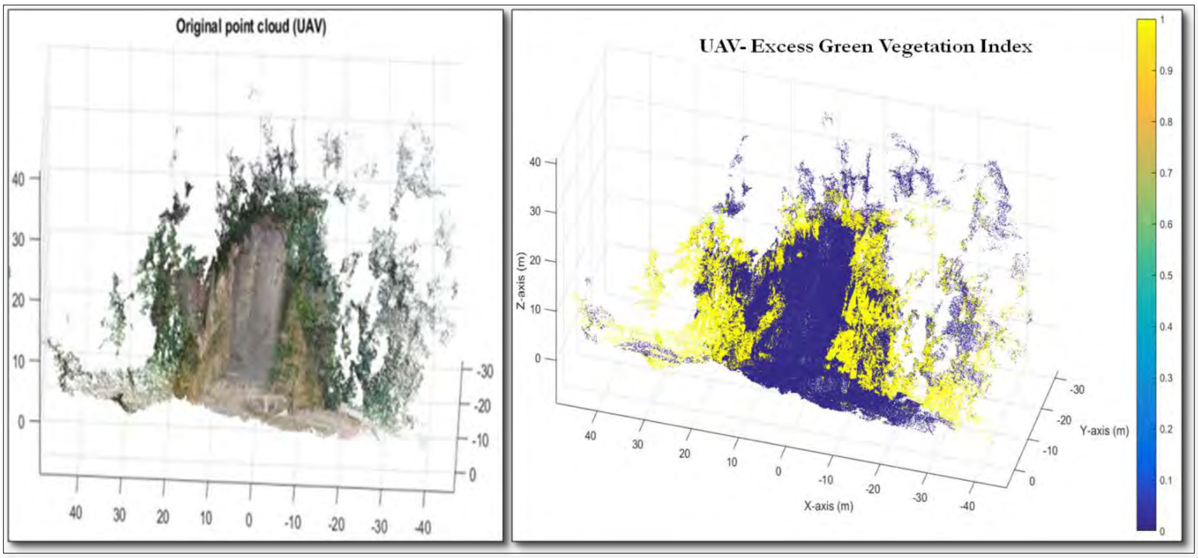

(Fig 5-15b)

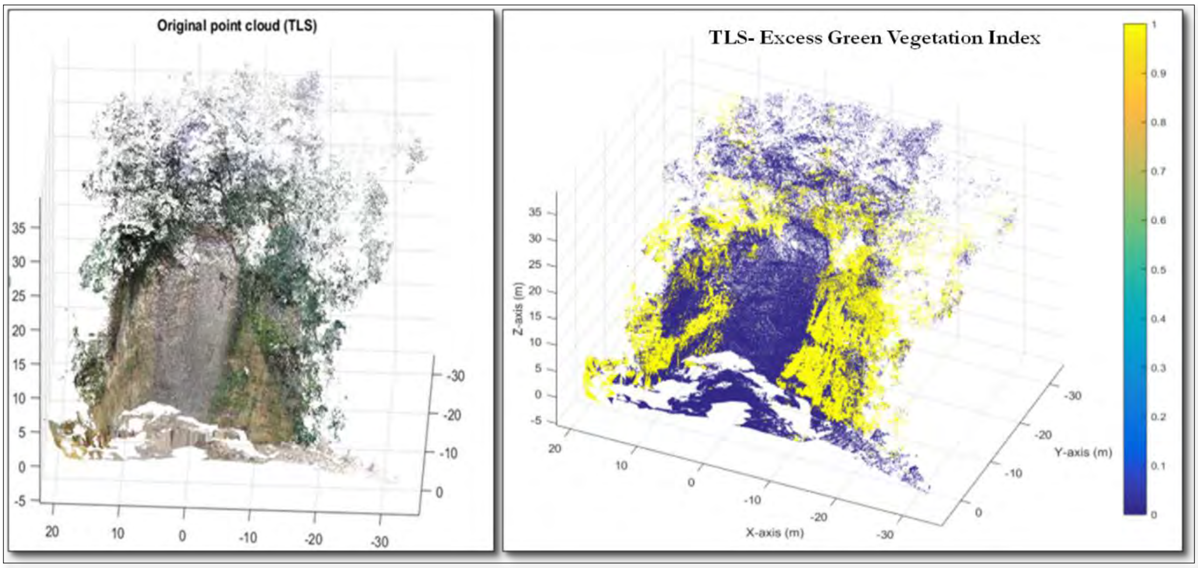

Figure 5-15: The detection of vegetation and organic activities on the rock mass surface. (a) represents the UAV-based 3D image and (b) represents the TLS 3D image, the color bar ranges from 0 (blue) to 1(yellow) and represents the classification of the rock mass with 1 for vegetated regions while 0 is for the non-vegetated regions.

5.3.3. Extraction of oxidized and total organic carbon regions as weathering signatures from the point cloud data

Several computation carried out using the RGB values of the oxidation areas shown clearly in the visible image from the series of imagery captured with the digital camera mounted on the UAV platform yielded RGB values with R=160, G=155 and B=100 within a range of +/-20. These RGB values are a function of the camera model used, PHANTOMVISIONFC200_5.0_4608x3456 (RGB) and the camera settings, with focal length of 5mm and pixel size of 1.4µm. The RGB values were used to extract the oxidized points from the UAV-based and TLS point cloud datasets respectively (Figures 5-16a-b). Similar operations were carried out to extract the regions with total organic carbon on the Gildehaus slope. The computation process carried out yielded RGB values with R=152, G=150 and B= 145 within a range of +/-20. The corresponding 3D images are shown in Figures 5-17a-b. The yellow regions in Figures 5-16 and 5-17 represents the oxidized and total organic carbon regions respectively, while the blue regions represent the non-oxidized and non-total organic carbon regions on the rock mass as supported by the original point cloud datasets in the Figures.

(Fig 5-16a)

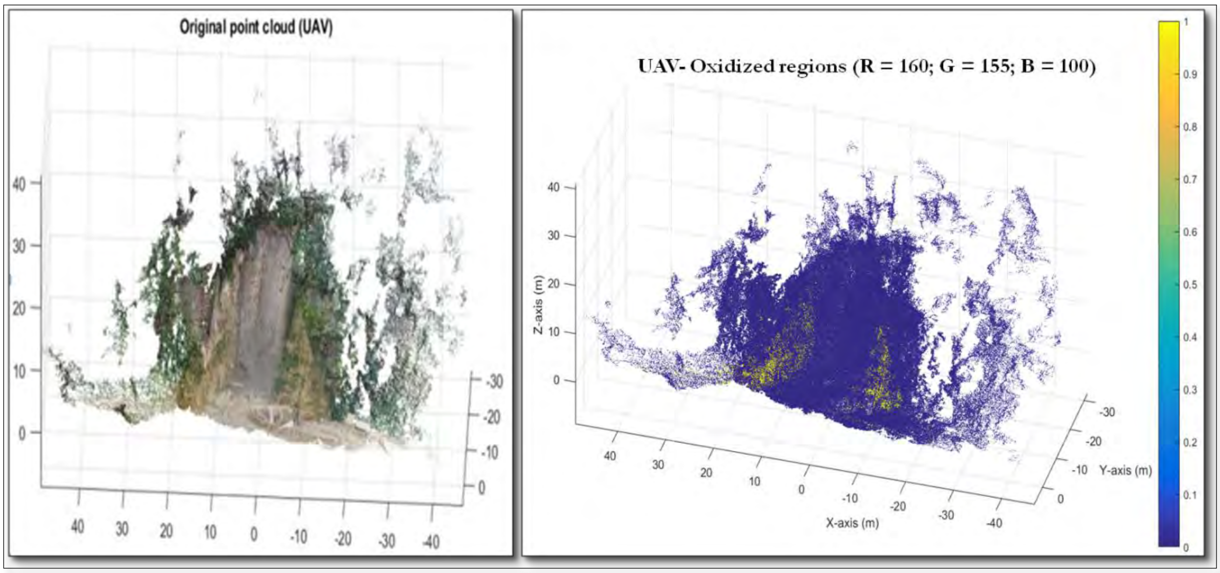

(Fig 5-16b)

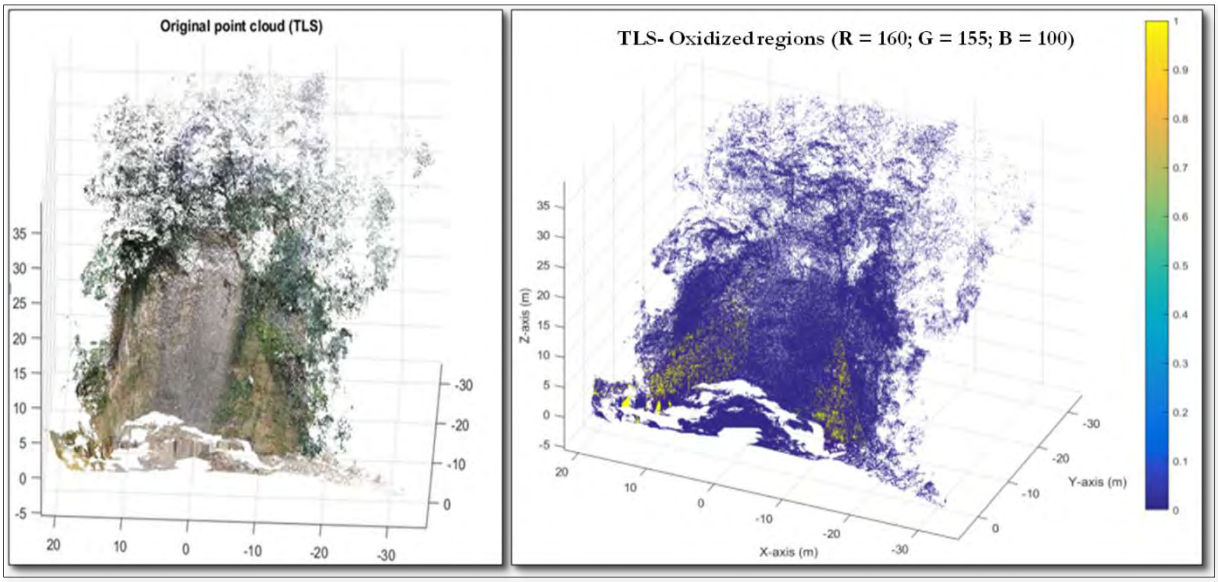

Figure 5-16: The detection of oxidized regions on the rock mass surface. (a) represents the UAV-based 3D image and (b) represents the TLS 3D image, the color bar rages from 0 (blue) to 1(yellow) and represents the classification of the rock mass with 1 for oxidation areas while 0 is for non-oxidation areas.

The application of the RGB values used to extract the oxidized regions and areas with the deposition of total organic carbon is a good technique as it shows acceptable results that are good representative of the real situation on the Gildehaus slope. It is also an easy and relatively quick method to classify the rock mass and determine the areas likely undergoing weathering or prone to weathering as a result of the rock mineralogy and the surrounding climate condition in the study area. Although, steps have been taken to reduce the inherent error in the technique by the series of computation carried out before the final acceptance of the used RGB values but the acceptance was biased as it was based on how well the user saw the RGB values representing closely the features of interest. This, however does not negate its usefulness until an arithmetic operation similar to the excess green can be derived. In Figures 5-16a-b, the points covered by oxidation are quite sparse in comparison to similar regions in the original point cloud datasets. This is as a result of the sub-sampling process carried on the datasets, otherwise an expected dense oxidized regions would have been extracted corresponding to the situation on the rock mass.

(Fig 5-17a)

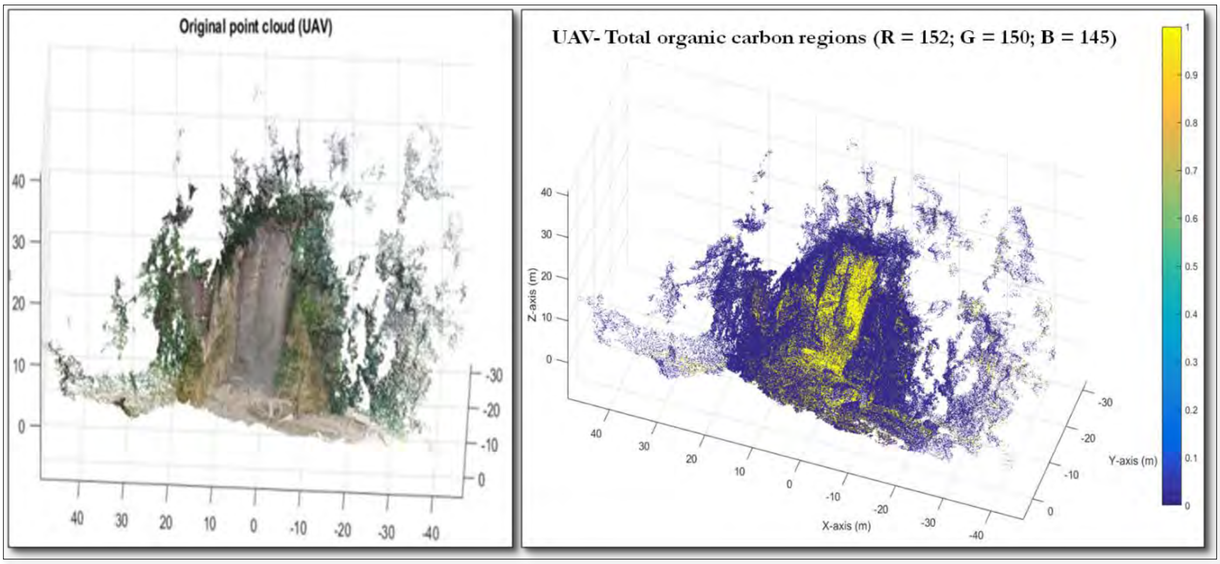

(Fig 5-17b)

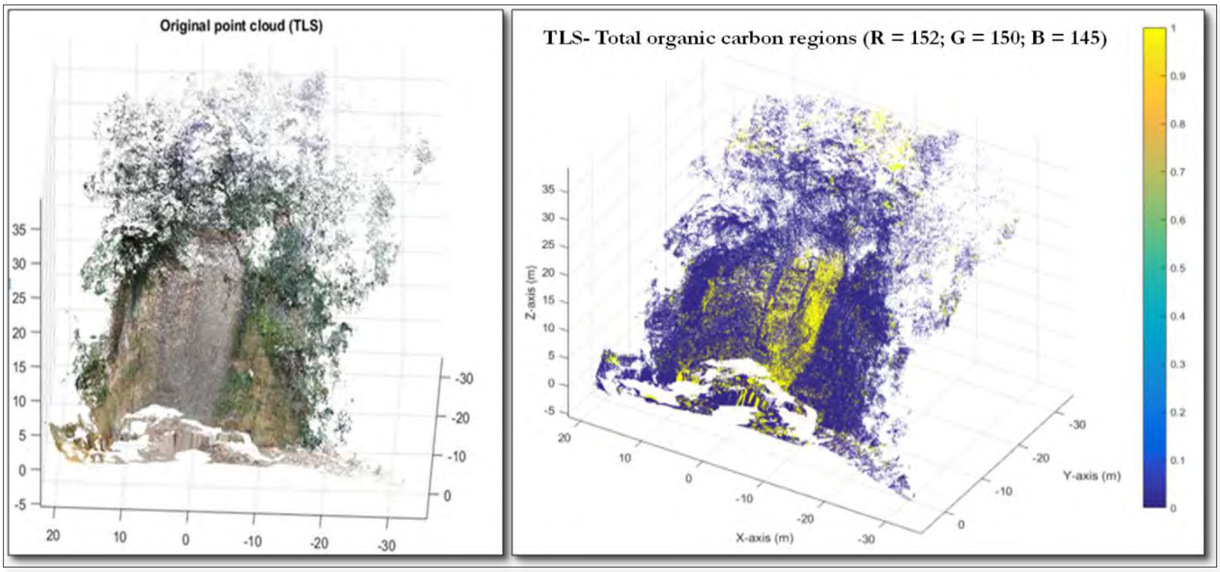

Figure 5-17: The detection of regions with total organic carbon on the rock mass surface. (a) represents the UAV-based 3D image and (b) represents the TLS 3D image, the color bar rages from 0 (blue) to 1(yellow) and represents the classification of the rock mass with 1 for total organic carbon regions while 0 is for non-total organic carbon regions.

5.3.4. Extraction of discontinuity geometry as weathering signature from the point cloud data

The RANSAC algorithm applied to the UAV-based and TLS 3D point cloud datasets was able to detect the direction of three (3) distinct planes. It highlighted the general direction of the bedding plane as oriented horizontally (Figure 5-18), as well as the location and orientation of the two joint discontinuities which is a good representation of the position of the joint discontinuities as observed on the rock mass during the field investigation of the Gildehaus slope (see Appendix 9).

There was a limitation in the detection of the discontinuity spacing and the conditions of the discontinuities, although the discontinuity persistence for the joint system can be inferred as being continuous from the representative planes derived from the automatic shape detection process. From the field investigation, observation shows three types bedding planes, with two very similar in orientation but the shape detection technique was only able to detect the general orientation of all the bedding planes. The method, however shows the possibility of the UAV-based 3D point cloud data by highlighting its geometric quality for extracting the parameters that define the discontinuities in the rock mass as clearly as can be carried out using the TLS point cloud data. The results are supported by the comparative analysis carried out by Duarte et al., (2015) which states that the UAV-based point clouds have sufficient geometric quality, very reasonable accuracy, reduce cost and is also applicable for fully automated mapping solutions comparable to the TLS point cloud data, although with lower quality. However, the visual comparison of the UAV-based point cloud with the TLS shows a high quality in the UAV-based dataset in par with the TLS data, although with reduce accuracy in relation to the exact spatial location of the points on the Gildehaus slope has analysed from the cloud to cloud distance analysis carried out on the two point cloud datasets.

(a) 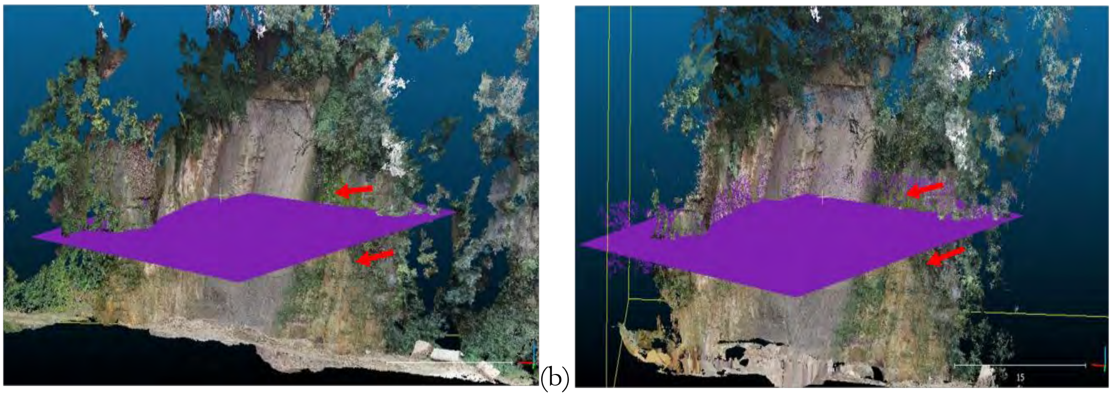 (b)

Figure 5-18: The detection of the discontinuities in the rock mass. (a) and (b) represents the bedding plane in the UAV-based and TLS 3D images respectively, the red arrow shows the direction of the discontinuity in the rock mass, while the purple plane shows the orientation of the bedding plane discontinuity.

5.4. Integration of the UAV-based and TLS point cloud datasets with the thermal imagery

Visual analysis of the thermal images taken in the early morning (9am), at noon (12pm) and in the afternoon (2pm) showed as expected the 2pm thermal images giving the highest thermal intensities although, there was not much structure of the features present on the Gildehaus slope, and seen clearly in the visible images and the point cloud data, in the thermal imagery. The thermal images did not show very clearly and distinctively features such as the discontinuity geometry and surfaces that are fresh or slightly weathered on the rock surface. The likely reason is due to the effect of heat diffusion that takes place when heat from a hot weathered surface spreads to the surrounding cold regions around it, thus affecting the thermal image by causing a blurring effect of the features of interest. An illustration is given in Figures 5-19a-c, a section from unit A, where the discontinuity indicated by the pink arrow in the visible image (b) and shown not too clearly in the thermal image captured in the morning (9am), could not be made out in the noon and afternoon thermal images as a result of heat diffusion, whereas the other discontinuity marked by the yellow arrow and the regions with the presence of organic matter marked by the green arrow in the visible image and in all the thermal images could still be detected.

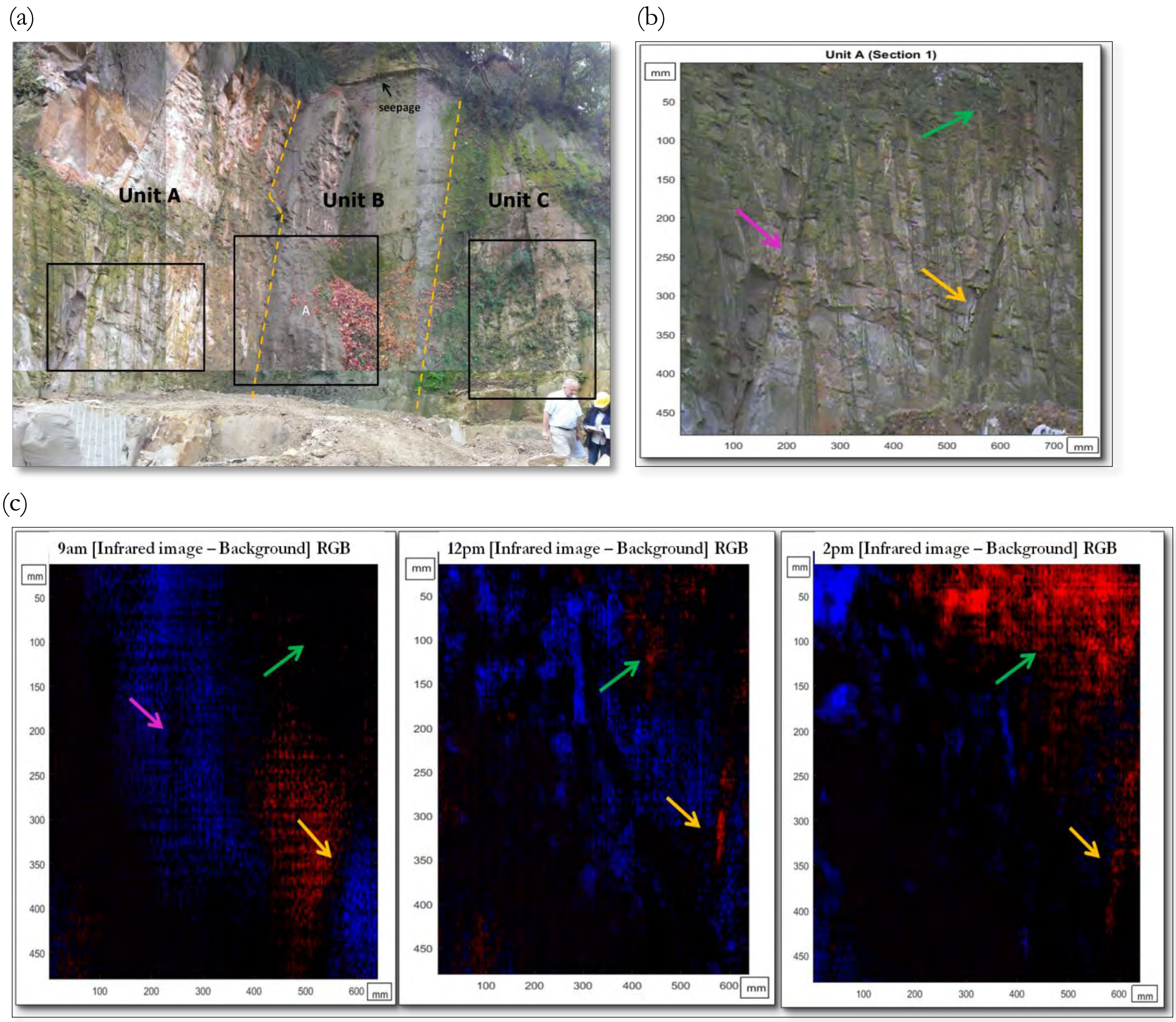

Figure 5-19: The visible and the thermal images of relatively the same location on the rock mass surface. (a) represents the Gildehaus slope highlighting the areas on the geotechnical units used for analysis, (b) shows the visible image of section (700x450mm) from unit A, while (c) shows the thermal images of section (600x450mm) from unit A captured in the morning at 9am, at noon by 12pm and in the afternoon at 2pm. The pink and yellow arrows indicate the position of the discontinuities in the images, while the green arrow points to the location of the cluster of organic matter on the rock mass.

However, weathering signatures investigated in unit B, shown in Figures 5-20a-c, using the thermal images showed relatively good contrast between the weathered surfaces, as a result of the presence of vegetation, oxidation and total organic carbon, in comparison to non-weathered surfaces. The two surfaces were distinguishable as a result of differences in their radiant capacity and chemical composition. This is supported by the results of the emissivity and XRD analysis carried out on the rock samples from the geotechnical units, showing variation as a result of the concentration of minerals in each of the units. The visual comparative analysis carried out using the UAV-based and TLS point clouds with the thermal imagery shows that the thermal radiance of the rock mass surface captured, exhibits and supports weathered rock mass characteristics has mentioned in literature in Chapter 2.2.5. Areas with vegetation, and organic matter on the rock mass surface gave high radiant temperature as indicated by the green arrows in Figures 5-20a-c. Referencing the statement made by Campbell & Claridge (1987) and stated also in Chapter 2.2.5, it supports the conclusion drawn as well as the field investigation carried out that the areas were sufficient weathering has occurred are able to sustain the development of vegetation. However, the presence of organic matter on the rock mass, although their growth may not necessarily have been attributed to the weathering process on-going on the rock mass, contribute greatly to the continuous action of both physical and chemical weathering on the rock mass. Areas at the toe of the rock mass with deposited debris and weathered materials as well as regions with total organic carbon radiated with high thermal intensity, especially in the afternoon (2pm) thermal image, as shown by the yellow and pink arrows respectively in Figures 5-20a-c. These high thermal intensities are likely due to the presence of moisture in these regions, thus increasing the thermal capacity of the areas. The purple arrow in Figures 5-20a-c indicates the fresh to slightly weathered region captured from unit A as part of the section from unit B, to highlight the thermal intensity contrast between the weathered and non-weathered surface. The oxidized areas also radiated with high thermal intensity, but the regions with deposited weathered products and vegetation radiated with the highest thermal intensity.

(a)

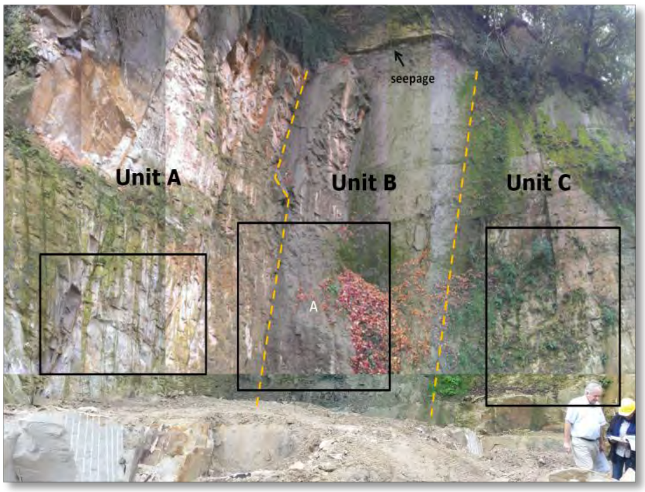

(b)

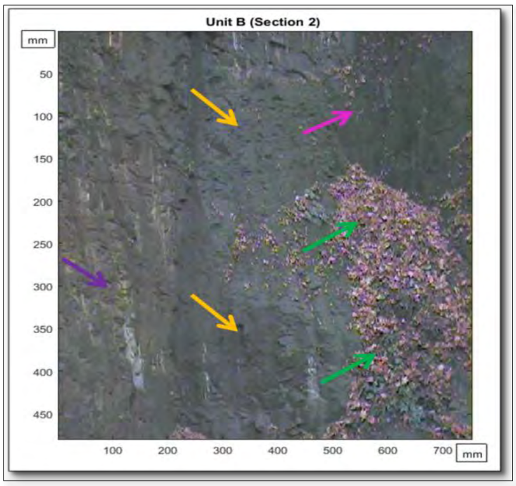

(c)

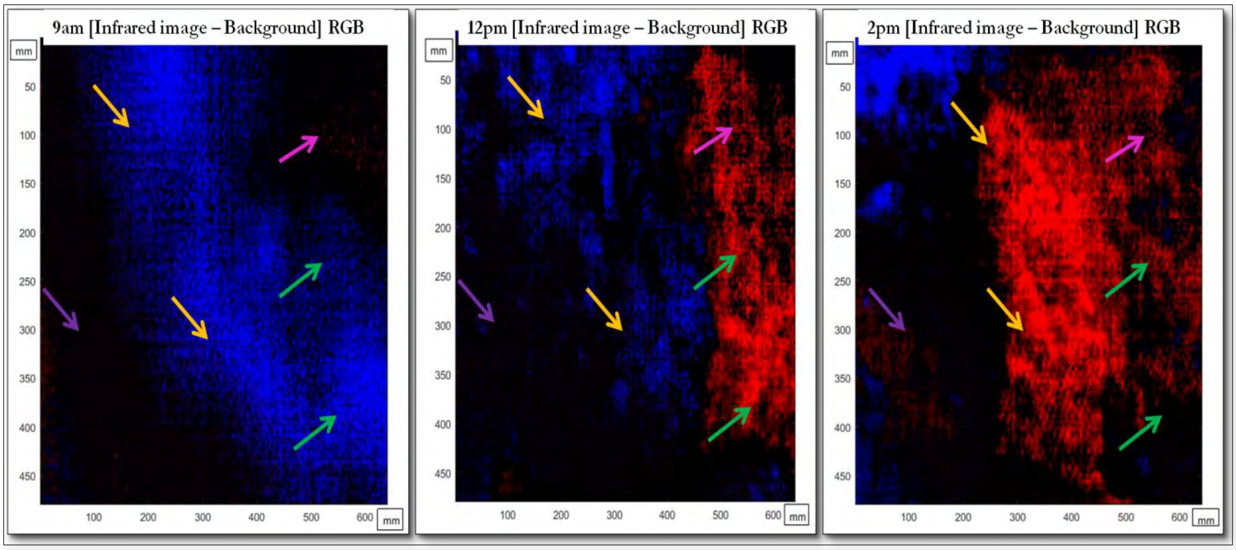

Figure 5-20: The visible and the thermal images of relatively the same location on the rock mass surface. (a) represents the Gildehaus slope highlighting the areas on the geotechnical units used for analysis, (b) shows the visible image of section (700x450mm) from unit B, while (c) shows the thermal images of section (600x450mm) from unit B captured in the morning at 9am, at noon by 12pm and in the afternoon at 2pm. The yellow arrows indicate the deposited weathered products, pink arrow indicates the total organic carbon areas, green arrows indicate the vegetation, while the purple indicates the bare slightly weathered to fresh rock surface captured from unit A.

However, this does not necessarily hold true for all the thermal images capturing the radiant temperature of the rock mass, as shown by the section from unit C (see Appendix 11). There are certain areas were the total organic carbon or oxidized regions radiate as hotter than either the vegetated or deposited weathered products areas, but in general they all reflect hotter than the bare slightly weathered or fresh rock mass.

5.5. Assessment and estimation of the weathering signatures detected using the UAV-based and TLS point cloud datasets

Weathering signatures such as coloration of the rock mass (due to oxidation and total organic carbon), presence of vegetation and organic activities, discontinuity geometry were only detectable on a large scale for the whole slope exposure using the UAV-based and TLS datasets. The first assessment carried out on these weathering signatures detectable on a large scale was done by calculating for the percentage of points covered by the weathering signatures extracted from the point cloud datasets (Table 5-6) with reference to the total points that makes up the rock mass for both point cloud datasets (see Appendix 10). The next assessment was carried out for a small scale of detection using the segmented point clouds from the point cloud datasets used for analysis in Chapter 5.4. The weathering signatures detected were the same as the features analysed for the whole slope exposure and were extracted using the same methodology as used in Chapter 4.4.4 (see Appendix 12a), except for the discontinuity geometry were a semi-automatic approach was applied. The segmented point clouds from each of the geotechnical units were visualised, with the bedding planes and joints manually delineated. The distances between the bedding planes and joints respectively, were derived with the application of a Matlab code (see Appendix 12b). The smallest of the distances for each discontinuity set was selected.

Table 5-6: Result of the assessment analysis carried out to detect the percentage of points in the UAV-based and TLS point cloud datasets covered by the weathering signatures for the whole slope exposure.

Weathering signatures	Percentage point covered by weathering signatures (%)	
	UAV-based 3D point cloud	TLS 3D point cloud
Vegetation and organic matter	**32.2**	**29.4**
Oxidation on the rock surface	**4.0**	**4.0**
Presence of total organic carbon	**15.2**	**16.0**

Table 5-7: Result of the assessment analysis carried out to detect the percentage of points in the UAV-based and TLS point cloud datasets covered by the weathering signatures for the segmented points in each of the geotechnical units.

Weathering signatures	Geotechnical Unit	Percentage point covered by weathering signatures (%)	
		UAV-based 3D point cloud	TLS 3D point cloud
Vegetation & organic matter on the rock mass surface	Unit A	51.1	52.1
	Unit B	19.4	22.5
	Unit C	50	51
Oxidation on the rock mass surface	Unit A	16.6	14.6
	Unit B	1.6	1.5
	Unit C	11.3	12.6
Presence of total organic carbon	Unit A	14.3	16.4
	Unit B	32.1	31.6
	Unit C	6.5	6.6

Results in Tables 5-6 and 5-7 shows that the extracted weathering signatures are quite comparable in the UAV-based and TLS point cloud datasets. Table 5-6 shows a difference of 2.8% for the vegetation extracted in the UAV-based data more than the TLS, while a difference of 0.8% for the total organic carbon was extracted more in the TLS data than in the UAV-based data. The variation in the percentages between the UAV-based and TLS point cloud datasets, as highlighted by Tables 5-6 and 5-7, is likely due to the variation in the density of points in the regions were the weathering signatures have been extracted. Table 5-7 shows unit A, in the UAV-based and TLS datasets, having the highest percentage of points covered by vegetation and organic matter (51.1% and 52.1%) as well as oxidation (16.6% and 14.6%) respectively in comparison to the other units, this is supported by the influence of the humid environmental conditions of the study area making the rock mass prone to the presence of lichens, moss and algae even on recently exposed surface. Although, this does not immediately translate to progressed weathering condition or reduced intact rock strength as supported by the sounding analysis carried out on the rock mass (see Chapter 5.1.1.2). The oxidation is a consequence of the iron minerals present in the fresh rock composition reacting with air or water, as indicated by the results of the XRD analysis (see Figure 5-10 and Table 5-2). Unit C also exhibited a high percentage of points covered by oxidation (11.3% and 12.6%), although expected to have the highest percentage, the likely reason is the resistance of the surface to further oxidation, with the large clusters of organic matter and sparse vegetation. As expected, unit B shows the highest percentage of total organic carbon, this is supported by the weathering horizontal variability carried out during the description and classification of the Gildehaus slope.

Table 5-8: Result of the assessment analysis carried out to detect the discontinuity geometry in the UAV-based and TLS point cloud datasets for the whole slope exposure.

Weathering signatures	UAV-based 3D point cloud	TLS 3D point cloud
▪ Bedding plane discontinuity	Direction- sloping horizontally	Direction- sloping horizontally
Discontinuity spacing	-	-
Discontinuity persistence	Infer as continuous	Infer as continuous
▪ Joint discontinuity	Direction- sloping vertically	Direction- sloping vertically
Discontinuity spacing	-	-
Discontinuity persistence	Infer as continuous	Infer as continuous

Table 5-9: Result of the assessment analysis carried out to detect the discontinuity geometry in the UAV-based and TLS point cloud datasets for the segmented points in each of the geotechnical units.

Weathering signatures	Geotechnical Unit	UAV-based 3D point cloud	TLS 3D point cloud
▪ Bedding plane discontinuity	All units	Direction- sloping horizontally.	Direction- sloping horizontally.
Discontinuity spacing	Unit A	0.3847m	0.3784m
	Unit B	0.3411m	0.2897m
	Unit C	0.3705m	0.3040m
Discontinuity persistence	All units	Continuous	Continuous
▪ Joint discontinuity		Direction- sloping vertically	Direction- sloping vertically
Discontinuity spacing	Unit A	3.9753m	3.1603m
	Unit B	3.2366m	3.2340m
	Unit C	Presence of a single joint set	Presence of a single joint set
Discontinuity persistence	All units	Continuous	Continuous

Comparison of the results displayed in Table 5-8 shows that the discontinuity geometry in the UAV-based and TLS point cloud datasets are the same. Table 5-9 shows a variation between the bedding plane spacing in the point cloud datasets, this is due to the limitation of the method applied. The manual delineation of the bedding planes are quite subjective, as it was majorly based on the user's ability to clearly visual and place the lines representing the discontinuities accordingly, which was quite challenging especially for the TLS data, where the bedding plane were not very clearly shown. Thus, the spacing between the discontinuities measured is a function of how well the lines were drawn, a slight shift in the lines will influence the results acquired. The joint discontinuity spacings give better comparable results in both the UAV-based and TLS datasets. This is likely due to the clearer visualization of the joint discontinuities in the point cloud datasets. However, comparison of the spacing results with the measured values during the geologic field investigation shows are relative variation. This is likely due to taking of the spacing measurement following the orientation of the discontinuities, instead of the straight line method used in the field, and also the precision of the delineated lines along the discontinuities.

The final assessment of the effectiveness of the UAV-based and TLS datasets in the detection of weathering signatures was carried out using the SSPC following Approach 1 and 2 of the British Standard 5930:1999, with the results highlighted in Tables 5-6 to 5-9. The results of the assessment analysis (Table 5-8) were validated by critical comparison with the developed geological field description, chemical analysis and weathering classification table (see Table 5-5). For good visualization, the table from the assessment analysis was color-coded. The UAV-based and TLS point cloud datasets were graded with good application represented by green, moderate as yellow, while poor application was represented by red.

Table 5-10: Assessment of the UAV-based and TLS point cloud dataset in the detection of weathering signatures.

Parameters	UAV-based 3D point cloud	TLS 3D point cloud
▪ Color	Representative of the actual coloration on the rock mass surface in the study area.	The scalar intensity of the TLS data was converted to RGB, using the UAV-based data has a reference, to aid in accurate visualisation and ensure uniform comparison.
▪ Vegetation	The vegetation and the organic activities on the rock mass surface were extracted using the excess green vegetation index.	The vegetation and the organic activities on the rock mass surface were extracted using the excess green vegetation index.
▪ Oxidation	The oxidized regions were extracted using the RGB values with R=160, G=155, B=100, with a range of +/-20, These RGB values were acquired using the UAV-based images.	The oxidized regions were extracted using the RGB values with R=160, G=155, B=100 with a range of +/-20. These RGB values were acquired using the UAV-based images.
▪ Total organic carbon	Similarly, the total organic carbon regions were extracted using the RGB values with R=152, G=150, B=145 with a range of +/-20.	The total organic carbon regions were extracted using the RGB values with R=152, G=150, B=145 with a range of +/-20.
▪ Temperature	The thermal images show the weathered areas on the rock mass surface as having a higher thermal intensity in comparison with the bare slightly weathered or fresh rock exposure	The thermal images show the weathered areas on the rock mass surface as having a higher thermal intensity in comparison with the bare slightly weathered or fresh rock exposure
▪ Discontinuity spacing	Large scale detection- Spacing was not detected	Large scale detection- Spacing was not detected
	Small scale detection- Measured using semi-automated approach	Small scale detection Measured using semi-automated approach
▪ Discontinuity persistence	Large scale detection- Inferred a continuous. Small scale detection- Continuous.	Large scale detection- Inferred a continuous. Small scale detection- Continuous.
▪ Weathered products	The weathered products at the toe of the rock mass was detectable.	The weathered products at the toe of the rock mass were detectable.

Certain parameters such as grain size, texture, intact rock strength, infill material, aperture and roughness along the discontinuities were not detected from point cloud datasets. Though, the degree of roughness on the rock face was extractable using the entropy algorithm, but since the roughness on the rock face was due to the excavation activities in the study area, it was not considered. An overview shows that the UAV-based point cloud data was more optimal over the TLS point cloud data due to the advantage of the possible application of the UAV-based images in the detection and extraction of the weathering signatures. The results from the point cloud datasets suggest that a combination of physical and chemical weathering has occurred on the Gildehaus slope deduced from the weathering signatures extracted the UAV-based and TLS datasets. However, the weathering grade of the geotechnical units using the point cloud datasets could not be properly determined. The assessment results in comparison with Table 5-5 shows that geologic field investigation is still the most practicable, detailed and viable methodology in the detection of weathering process on a rock mass. Its major advantage is that it enables the weathering grade, using strength and reduction of strength, the condition of the discontinuities and other parameters of the rock mass, to be properly described using recognised and accepted standards.

6. CONCLUSION AND RECOMMENDATION

6.1. Conclusion

The several analyses carried out during the cause of this research aids to conclude that the studied slope has been subjected to both physical and chemical weathering resulting from the seepage of water, the atmospheric condition at the study area and the mineralogy of the rock mass. There were noticeable variation in the colouration of the rock mass exposed to the atmospheric condition in the study area that differs from the fresh newly exposed rock mass surfaces. Although, colour variation is seen as the first primary indication that weathering is on-going or has occurred, the changes in the colour of the exposed rock mass does not necessarily translate to the reduction of intact rock strength but it suggests that the rock mass is susceptible to both physical and chemical activities that causes weathering to occur.

Oxidation can be visually observed on the rock mass and chemical analysis on the rock samples show the presence of iron compounds. The total organic carbon attributing to the effect of black weathering on the rock mass, is influenced by the presence of gypsum and other minor quantity minerals present in the rock mass, vegetation, deposition of weathered products and debris, and air particles. The discontinuities in the rock mass and their geometrical properties and conditions have been contributing parameters, used in the analyses of the weathering process affecting the rock mass. The geologic field investigation has provided detailed information with quality accuracy used to infer the grade of weathering in each of the geotechnical units on the rock mass, and the acquired results indicate that it is still the most optimal in the detection of weathering activities on a rock mass. The application of the UAV-based and TLS point cloud datasets have been used in the assessment of the weathering indicators on the rock mass, while effective and efficient in the detection of weathering parameters like vegetation and organic matter, oxidation, total organic carbon, discontinuity set and the discontinuities geometry, other features such as texture, reduction in intact rock strength, spalling and flaking of the rock mass and the condition of discontinuity (aperture, roughness, infill material) were not detected due to the spatial resolution ranging from micrometers to 5mm required to detect them. Also, it was not possible in this study to apply the point cloud datasets to determine firmly the weathering grade of the geotechnical units in the rock mass.

The cloud to cloud comparison shows that there is a high agreement between the UAV-based and TLS point cloud datasets, except for areas along the toe of the rock mass and the vegetation at the edges of the rock mass captured in the UAV-based point cloud where there is a distance of 0-1m between the UAV-based and TLS point cloud data, with the TLS having a higher exact representation of the rock mass. The problem of occlusion was not experienced in the study area during the capture of the UAV-based images and the laser scanning. From the whole slope exposure, assessment analysis shows that 51.4% of the points were covered by weathering signatures in the UAV-based 3D point cloud, while 49.4% were covered by weathering signatures in the TLS 3D point cloud. This variation was expected only in differences between the vegetation extracted in both point cloud datasets, but the difference of 0.8% for the total organic carbon extracted more in the TLS point cloud data than in the UAV-based data, shows that either the UAV-based data is lesser denser in the regions where the total organic carbon were extracted as a result of the sub-sampling process carried out on the data or that the TLS gives a better accurate result. Since, the UAV-based and TLS point cloud datasets were both sub-sampled to the same number of points and the RGB used to visual and present the TLS data was derived the UAV-based data, it can be deduced that it is likely due to the lack of density of points. Overall, The UAV-based 3D point cloud was better applicable in the extraction of the total organic carbon and the oxidized regions as both the visible images and the 3D point cloud data were applied to develop the computation operation applied. In addition, the intensity of the TLS 3D point cloud had to be convert to RGB to be able to visually assess the data and apply the computation operation. Also, the UAV-based data was able to resolve the problem of color properties of weathered rock mass, which would have made it difficult to detect certain features on the rock mass especially the proxies weathering signatures like the organic activities on the rock mass. The UAV-based and TLS point cloud gave similar results to the field investigation in the assessment of the discontinuity sets for the whole slope exposure, giving the general orientation of the bedding planes as sloping horizontally with a continuous persistence, while two joints sets were highlighted and both slope vertically with continuous persistence. The estimation of the weathering signatures, vegetation, oxidation and the total organic carbon and the discontinuities geometry, in each of the geotechnical units from the UAV-based and TLS point cloud datasets are quite comparable, thus making the UAV-based 3D point cloud data a good alternative for TLS in the detection of weathering signatures and the more optimal in terms of cost and variable applications. The UAV-based a Although, in contrast to other methodologies, UAV requires permission to be operated but given the vast opportunities available in its application, strict regulations are to be expected to enable safe use but there is high possibility of global consensus.

The thermal images and the emissivity analysis helped in supporting some of the references stated in the literature, thus ensuring sound conclusion can be drawn about the influence of weathering on the rock mass using the observable thermal intensity variation between the fresh rock surface from unit A and the rock surface from the moderately to highly weathered geotechnical units B and C. Analysis shows that areas with vegetation and organic matter, deposited weathered products, oxidation and total organic carbon radiated with higher thermal intensity than bare slightly weathered or fresh surfaces on the rock mass face. However, the use of the thermal sensor has an absolute for weathering detection is limiting has the emissivity analysis show differing emissivities of the rock samples taken from the same geotechnical units of the Bentheim sandstone at the study area.

The major constraint experienced during the course of this study includes the unavailability of freely sourced software that can help in the detailed analyses of point cloud data, as well as being capable of providing a medium for the analyses of both UAV-based and TLS point cloud datasets.

6.2. Recommendation

The recommendations for future researches are:

1. The possibility of using the combination of UAV-based thermal sensor and digital camera to enable the development of a 3D thermal point cloud data. It will provide a more uniform platform for comparison, feature detection in the two datasets and a more technical integration of information extraction.
2. Development of indices similar to the excess green vegetation index to provide a more objective feature detection and extraction. Limiting also the influence of human bias.
3. Improvement on the CloudCompare user interface to support the insertion of features and direct measurement on the 3D point cloud data.
4. To ascertain the rate of weathering on the Gildehaus slope, there is need to carry out a time series of investigation and measurements from the study area to determine the physical changes ongoing on the rock mass to adequately estimate the weathering and future weathering.

LIST OF REFERENCES

Akhavan, A. C. (2015). Quartz as a Rock-Forming Mineral. Retrieved January 23, 2016, from http://www.quartzpage.de/gen_rock.html

Antoine, P., Giraud, A., Meunier, M., & Van Asch, T. (1995). Geological and geotechnical properties of the "Terres Noires" in southeastern France: Weathering, erosion, solid transport and instability. *Engineering Geology*, *40*(3-4), 223–234. doi:10.1016/0013-7952(95)00053-4

Arikan, F., & Aydin, N. (2012). Influence of Weathering on the Engineering Properties of Dacites in Northeastern Turkey. *ISRN Soil Science*, *2012*, 1–15. doi:10.5402/2012/218527

Assali, P., Grussenmeyer, P., Villemin, T., Pollet, N., & Viguier, F. (2014). Surveying and modeling of rock discontinuities by terrestrial laser scanning and photogrammetry: Semi-automatic approaches for linear outcrop inspection. *Journal of Structural Geology*, *66*, 102–114. doi:10.1016/j.jsg.2014.05.014

Barnea, S., & Filin, S. (2012). Extraction of Objects from Terrestrial Laser Scans by Integrating Geometry Image and Intensity Data with Demonstration on Trees. *Remote Sensing*, *4*(12), 88–110.

Beasy, C. (2015). Lidar Mapping: High Accuracy, High Speed - White Paper. Eagle Mapping Services. Retrieved from http://www.eaglemapping.com/_white_papers/Lidar WPaper ENG - Mar08.pdf

Bell, F. G. (1992a). *Engineering Properties of Soils and Rocks* (3rd ed.). Oxford, London: Butterworth-Heinemann Ltd.

Bell, F. G. (1992b). Influence of weathering and discontinuities on the behaviour of rock masses. In *Engineering in Rock Masses* (pp. 27–53). doi:http://dx.doi.org/10.1016/B978-0-7506-1965-3.50006-6

Bemis, S. P., Micklethwaite, S., Turner, D., James, M. R., Akciz, S., Thiele, S. T., & Ali, H. (2014). Ground-based and UAV-Based photogrammetry: A multi-scale, high-resolution mapping tool for structural geology and paleoseismology. *Journal of Structural Geology*. doi:10.1016/j.jsg.2014.10.007

Birkeland, P. W. (1999). *Soils and geomorphology* (3rd ed.). New York. USA: Oxford university press.

Blyenburgh, P. van. (1999). UAVs: an overview. *Air & Space Europe*, *1*(5-6), 43–47.

Bockheim, J. G. (Ed.). (2015). *The Soils of Antarctica*. Cham: Springer International Publishing.

Boggs, S. J. (2009). *Petrology of Sedimentary Rocks*. Cambridge University Press.

Bruker Corporation. (2016). DIFFRAC.SUITE EVA Phase Analysis - XRD Software, X-ray diffraction. Retrieved January 21, 2016, from https://www.bruker.com/products/x-ray-diffraction-and-elemental-analysis/x-ray-diffraction/xrd-software/overview/eva/eva-phase-analysis.html

BS 5930:1999. (1999). *Code of practice for site investigations*. *British Standard*. London: British Standard Institution.

Bulut, F., & Tüdeş, Ş. (1996). Determination of discontinuity traces on inaccessible rock slopes using electronic tacheometer: an example from the İkizdere (Rize) Region, Turkey. *Engineering Geology*, *44*(1-4), 229–233.

Butcher, S. S., Charlson, R. J., Orians, G. H., & Wolfe, G. V. (Eds.). (1992). *Global biogeochemical cycles*. Oval Road, London: Academic Press.

Butler, J. R. (1953). The geochemistry and mineralogy of rock weathering: The Lizard area, Cornwall. *Geochimica et Cosmochimica Acta*, *4*, 157–178.

Cabria, X. A. (2015). *Effects Of Weathering In The Rock And Rock Mass Properties And The Influence Of Salts In The Coastal Roadcuts In Saint Vincent And Dominica*. Faculty of Geo-Information Science and Earth Observation. Retrieved from http://www.itc.nl/library/papers_2015/msc/aes/cabria.pdf

Calcaterra, D., & Parise, M. (2010). Weathering in the crystalline rocks of Calabria, Italy, and relationships to landslides. *Geological Society, London, Engineering Geology Special Publications*, *23*(1), 105–130.

Campbell, I. B., & Claridge, G. G. C. (1987). *Antarctica: Soils, Weathering Processes and Environment: Soils, Weathering Processes and Environment*. Elsevier.

Ceryan, S. (2012). Weathering indices for assessment of weathering effect and classification of weathered rocks: a case study from NE Turkey. *Earth Sciences*. *InTech*. doi:10.1016/j.jafrearsci.2014.12.005

Ceryan, S., Tudes, S., & Ceryan, N. (2008). A new quantitative weathering classification for igneous rocks. *Environmental Geology*, *55*(6), 1319–1336. doi:10.1007/s00254-007-1080-4

Chandler, R. J., & Apted, J. P. (1988). The effect of weathering on the strength of London Clay. *Quarterly Journal of Engineering Geology and Hydrogeology*, *21*(1), 59–68. doi:10.1144/GSL.QJEG.1988.021.01.04

Cowan, P. D., & Huntington, P. K. (2011). Lecture Notes: ESS 211 - Physical Processes of the Earth - Weathering soils handout. University of Washington. Retrieved from http://courses.washington.edu/ess211/Lecture_files/Weathering-soils_handout.pdf

Currey, D. T. (1977). Deeply weathered rock at victorian damsites. *Engineering Geology*. doi:10.1016/0013-7952(77)90038-2

Curtaz, M., Ferrero, A. M., Roncella, R., Segalini, A., & Umili, G. (2013). Terrestrial photogrammetry and numerical modelling for the stability analysis of rock slopes in high mountain areas: Aiguilles marbr??es

case. *Rock Mechanics and Rock Engineering*, *47*(2), 605–620. doi:10.1007/s00603-013-0446-z
Danzi, M., Crescenzo, G. Di, Ramondini, M., & Santo, A. (2013). Use of unmanned aerial vehicles (UAVs) for photogrammetric surveys in rockfall instability studies. *Rendiconti Online Societa Geologica Italiana*, *24*, 82–85.
Day, R. W. (1994). Weathering of expansive sedimentary rock due to cycles of wetting and drying. *Bulletin of the Association of Engineering Geologists; (United States)*, *31*(3), 387–390.
Dearman, W. R. (1974). Weathering classification in the characterization of rock for engineering purposes in British practice. *Bulletin International Association of Engineering Geology*, *9*, 33–42.
Deere, D. U., & Miller, R. P. (1966). Engineering Classification And Index Properties For Intact Rock. Retrieved from http://oai.dtic.mil/oai/oai?verb=getRecord&metadataPrefix=html&identifier=AD0646610
Drees, A. (2015). Bentheim sandstone - Lower Saxony. Retrieved November 10, 2015, from http://www.niedersachsen-tourism.com/bentheim-sandstone#mapOpen=false
Drever, J. I. (Ed.). (2005). *Surface and Ground Water, Weathering, and Soils: Treatise on Geochemistry* (2nd ed., Vol. 5). Elsevier. Retrieved from https://books.google.com/books?id=7NbGsXg96OAC&pgis=1
Duarte, J., Gonçalves, G., Duarte, D., Figueiredo, F., & Mira, M. (2015). Comparison of 3D point clouds obtained by photogrammetric UAVs and TLS to determine the attitude of dolerite outcrops discontinuities . In *European Geosciences Union (EGU) General Assembly 2015* (Vol. 17, p. 6630). Vienna, Austria: Geophysical Research Abstracts.
Dubelaar, W. C., Nijland, T. G., & Dubelaar, W. C. (2015). The Bentheim Sandstone: Geology, Petrophysics, Varieties and Its Use as Dimension Stone. In G. Lollino, D. Giordan, C. Marunteanu, B. Christaras, I. Yoshinori, & C. Margottini (Eds.), *Engineering Geology for Society and Territory - Volume 8* (Vol. 8, pp. 557–563). Cham: Springer International Publishing. doi:10.1007/978-3-319-09408-3_100
EPA, U. S. E. T. I. and F. S. D. (2008). Module 2 : Basic XRF Concepts. Retrieved January 23, 2016, from https://clu-in.org/conf/tio/xrf_080408/prez/XRF_02pdf.pdf
Everton, S. J., & Diffin, B. T. (2004). Technical Note Study of the benefits of ICE Site Investigation Steering Group documents: 10 years on. Retrieved November 5, 2015, from http://www.nce.co.uk/Journals/2015/01/26/s/e/t/2004-12_Pages_32-35.pdf
Fagbohun, B. J. (2015). *Combining Dominant Spectral Features in Airborne SWIR and TIR Imagery for Mineralogical Mapping*. University of Twente.
Fell, R., MacGregor, P., Stapledon, D., Bell, G., & Foster, M. (2014). *Geotechnical Engineering of Dams* (2nd ed., Vol. 25). CRC Press.
Fowler, A., France, J. I., & Truong, M. (2010). Applications of Advanced Laser Scanning Technology in Geology. *Riegl USA*, 7. Retrieved from http://www.rieglusa.com/pdf/applications-of-advanced-laser-scanning-technology-in-geology-ananda-fowler-final.pdf
Franklin, J. a., Maerz, N. H., & Bennett, C. P. (1988). Rock mass characterization using photoanalysis. *International Journal of Mining and Geological Engineering*, *6*(2), 97–112. doi:10.1007/BF00880801
Fritz, a., Kattenborn, T., & Koch, B. (2013). UAV-Based Photogrammetric Point Clouds – Tree Stem Mapping in Open Stands in Comparison To Terrestrial Laser Scanner Point Clouds. *ISPRS - International Archives of the Photogrammetry, Remote Sensing and Spatial Information Sciences*, *XL-1/W2*(September), 141–146.
Geertsema, A. J. (2003). *The Shear strength of rock joints with special reference to dam foundations*. University of Pretoria.
Gifford, C. (2005). *Weathering and Erosion*. Evans Brothers.
Girardeau-Montaut, D. (2015). CloudCompare v2.6.1 - User manual. http://www.danielgm.net. Retrieved from http://www.danielgm.net/cc/doc/qCC/CloudCompare v2.6.1 - User manual.pdf
González-Gómez, W. S., Quintana, P., May-Pat, A., Avilés, F., May-Crespo, J., & Alvarado-Gil, J. J. (2015). Thermal effects on the physical properties of limestones from the Yucatan Peninsula. *International Journal of Rock Mechanics and Mining Sciences*, *75*, 182–189. doi:10.1016/j.ijrmms.2014.12.010
Götze, J. (2012). Classification, Mineralogy and Industrial Potential of SiO2 Minerals and Rocks. In *Quartz: Deposits, Mineralogy and Analytics* (pp. 1–27). Berlin, Heidelberg: Springer Berlin Heidelberg.
Gupta, A. S., & Rao, S. K. (2001). Weathering indices and their applicability for crystalline rocks. *Bulletin of Engineering Geology and the Environment*, *60*(3), 201–221. doi:10.1007/s100640100113
Gupta, R. P. (2003). *Remote Sensing Geology*. Berlin, Heidelberg: Springer Berlin Heidelberg.
Hack, H. R. G. K. (1998). *Slope Stability Probability Classification (SSPC)* (2nd ed.). Enschede, The Netherlands.
Hack, H. R. G. K. (2006). *Discontinuous Rock Mechanics* (5th ed.). Enschede, The Netherlands.
Hack, H. R. G. K. (2012). Weathering Influence on Engineering Structures _ presentation. The Netherlands.
Hack, H. R. G. K., & Huisman, M. (2002). Estimating the intact rock strength of a rock mass by simple means. *Engineering Geology for Developing Countries*, (0), 1971–1977.
Hack, H. R. G. K., & Price, D. G. (1997). Quantification of weathering. *Engineering Geology and the Environment. Athens.*, 145–150.

Hack, H. R. G. K., Price, D., & Rengers, N. (2003). A new approach to rock slope stability – a probability classification (SSPC). *Bulletin of Engineering Geology and the Environment*, *62*, 167–184.

Hackney, C., & Clayton, A. I. (2015). Unmanned Aerial Vehicles (UAVs) and their application in geomorphic mapping. In L. Clarke & J. Nield (Eds.), *Geomorphological Techniques* (pp. 1–12). British Society for Geomorphology.

Hagen, A. (2012). *Engineering Geological Assessments of a Tunnel for the Proposed High Speed Railway Link Between Oslo and Bergen*. Norwegian University of Science and Technology. Retrieved from http://www.diva-portal.org/smash/get/diva2:603560/FULLTEXT01.pdf

Hall, K., Lindgren, B. S., & Jackson, P. (2005). Rock albedo and monitoring of thermal conditions in respect of weathering: some expected and some unexpected results. *Earth Surface Processes and Landforms*, *30*(7), 801–811. doi:10.1002/esp.1189

Hall, K., Meiklejohn, I., & Arocena, J. (2007). The thermal responses of rock art pigments: Implications for rock art weathering in southern Africa. *Geomorphology*, *91*(1-2), 132–145.

Hecker, C., Hook, S., van der Meijde, M., Bakker, W., van der Werff, H., Wilbrink, H., … van der Meer, F. (2011). Thermal infrared spectrometer for Earth science remote sensing applications-instrument modifications and measurement procedures. *Sensors*, *11*(11), 10981–99. doi:10.3390/s111110981

Heckes, J., Mauelshagen, L., & Skalli, M. (1988). Recording the Damages of Natural Stones. *International Society for Photogrammetry and Remote Sensing, Inc. (ISPRS)*, *27*(B5), 253–261.

Helipix UAV. (2015). Advantages of UAVs in Aerial Photography. Retrieved June 2, 2015, from http://www.helipix.org/advantages-of-uavs/4549253806

Hencher, S. (2008). Eurocodes- The "new" British and European standard guidance on rock description. A critique by Steve Hencher. Retrieved September 19, 2015, from http://www.nce.co.uk/eurocodes/1709994.article

Hillier, S. (2000). Accurate quantitative analysis of clay and other minerals in sandstones by XRD : comparison of a Rietveld and a reference intensity ratio (RIR) method and the importance of sample preparation. *Clay Minerals - The Mineralogical Society*, (35), 291–302.

Hoek, E., & Bray, J. D. (1981). *Rock Slope Engineering: Third Edition*. CRC Press. Retrieved from https://books.google.com/books?id=VSccRRWxHf4C&pgis=1

Hugenholtz, C. H., Whitehead, K., Brown, O. W., Barchyn, T. E., Moorman, B. J., LeClair, A., … Hamilton, T. (2013). Geomorphological mapping with a small unmanned aircraft system (sUAS): Feature detection and accuracy assessment of a photogrammetrically-derived digital terrain model. *Geomorphology*, *194*, 16–24.

Huisman, M. (2006). *Assessment of rock mass decay in artificial slopes*. Retrieved from http://www.itc.nl/library/papers_2006/phd/huisman.pdf

ICDD, T. I. C. for D. D. (2015). How to Analyze Minerals -Fundamentals. Retrieved January 20, 2016, from http://www.icdd.com/resources/tutorials/pdf/HowtoAnalyzeMinerals-Fundamentals.pdf

Irfan, T. Y. (1996). Mineralogy, fabric properties and classification of weathered granites in Hong Kong. *Quarterly Journal of Engineering Geology and Hydrogeology*, *29*(1), 5–35.

Ismael, M. A., Imam, H. F., & El-Shayeb, Y. (2014). A simplified approach to directly consider intact rock anisotropy in Hoek–Brown failure criterion. *Journal of Rock Mechanics and Geotechnical Engineering*, *6*(5), 486–492. doi:10.1016/j.jrmge.2014.06.003

ISO, 14689-1:2003. (2003). Geotechnical investigation and testing - Identification and classification of rock - Part 1: Identification and description. *European Committee for Standardization*.

ISRM. (1978). Suggested methods for the quantitative description of discontinuities in rock masses. *Int. J. Rock Mech. Min. Sci. Geomech. Abstr., 15*, 319–368.

Jain, S. (2014). *Fundamentals of Physical Geology*. Springer India. doi:10.1007/978-81-322-1539-4

Jenssen, E. T. (2007). CO2 free Svalbard under way. Retrieved November 8, 2015, from http://www.unis.no/60_NEWS/6030_Archive_2007/n_01_10_07_CO2/co2_free_svalbard_underway_news_01102007.htm

Jie, C., & Blume, H.-P. (2002). Rock-weathering by lichens in Antarctic : patterns and mechanisms. *Journal of Geographical Sciences*, *4*(40001011), 387–396. doi:10.1007/BF02844595

Kekeba, A. D. (2008). *Establishing relationship between thermal radiation and intensity of 3D terrestrial laser scan data of weathered rock surface for slope stability analysis*. University of Twente.

Kirkland, L. E. (2003). Infrared stealthy surfaces: Why TES and THEMIS may miss some substantial mineral deposits on Mars and implications for remote sensing of planetary surfaces. *Journal of Geophysical Research*, *108*(E12), 5137. doi:10.1029/2003JE002105

Klein, E., Baud, P., Reuschlé, T., & Wong, T. (2001). Mechanical behaviour and failure mode of bentheim sandstone under triaxial compression. *Physics and Chemistry of the Earth, Part A: Solid Earth and Geodesy*,

26(1-2), 21–25. doi:10.1016/S1464-1895(01)00017-5
Kumar, R., & Kumar, A. V. (1999). *Biodeterioration of Stone in Tropical Environments: An Overview*. Getty Publications. Retrieved from https://books.google.com/books?hl=en&lr=&id=D_7NzE5vKS0C&pgis=1
Lato, M. J., & Vöge, M. (2012). Automated mapping of rock discontinuities in 3D lidar and photogrammetry models. *International Journal of Rock Mechanics and Mining Sciences*, *54*, 150–158.
Liew, S. C. (2001). Electromagnetic Waves. Retrieved November 5, 2015, from http://www.crisp.nus.edu.sg/~research/tutorial/em.htm
Likar, J., Grøv, E., & Marolt, T. (2014). Basic parameters of small underground nuclear power stations. *RMZ-Materials and Geoenvironment*, *61*, 25–38. Retrieved from http://www.rmz-mg.com/letniki/rmz61/RMZ61_0025-0038.pdf
Mancini, F., Dubbini, M., Gattelli, M., Stecchi, F., Fabbri, S., & Gabbianelli, G. (2013). Using Unmanned Aerial Vehicles (UAV) for High-Resolution Reconstruction of Topography: The Structure from Motion Approach on Coastal Environments. *Remote Sensing*, *5*(12), 6880–6898. doi:10.3390/rs5126880
Mansurbeg, H. (2001). Modelling of reservoir quality in quartz-rich sandstone of the Lower Cretaceous Bentheim sandstones, Lower Saxony Basin, NW Germany.pdf. Lund, Sweden: Geologiska Institutionen, Lunds Universitet.
Matula, M. (1981). Rock and soil description and classification for engineering geological mapping report by IAEG Comission on engineering geological mapping. *Engineering Geology*, *24*, 235–274.
McGreevy, J. P. (1985). Thermal properties as controls on rock surface temperature maxima, and possible implications for rock weathering. *Earth Surface Processes and Landforms*, *10*(2), 125–136.
Meunier, J. D., Kirman, S., Strasberg, D., Grauby, O., & Dussouillez, P. (2014). Incipient weathering by Stereocaulon vulcani at Réunion volcanic island. *Chemical Geology*, *382*, 123–131.
Miller, V. C. (1968). Current trends in photogeology and in the use of other remote sensing methods in geological interpretation. *Earth-Science Reviews*, *4*, 135–152. doi:10.1016/0012-8252(68)90148-7
Miščević, P., & Vlastelica, G. (2014). Impact of weathering on slope stability in soft rock mass. *Journal of Rock Mechanics and Geotechnical Engineering*, *6*(3), 240–250. doi:10.1016/j.jrmge.2014.03.006
Mohamed, Z., Rafek, A. G., & Komoo, I. (2007). Characterisation and Classification of the Physical Deterioration of Tropically Weathered Kenny Hill Rock for Civil Works. *The Electronic Journal of Geotechnical Engineering (EJGE)*, *12*, 1–13.
Moses, C., Robinson, D., & Barlow, J. (2014). Methods for measuring rock surface weathering and erosion: A critical review. *Earth-Science Reviews*, *135*, 141–161. doi:10.1016/j.earscirev.2014.04.006
Mubiayi, M. P. (2013). Characterisation of Sandstones: Mineralogy and physical properties. In *Proceedings of the World Congress on Engineering 2013 Vol III* (p. 6). London, U.K: IAENG.
Mulenga, C. (2015). *Influence of weathering on geotechnical properties of road-cut slope mass and embankment fill on Saint Lucia and Saint Vincent*. University of Twente.
Nex, F., & Remondino, F. (2013). UAV for 3D mapping applications: a review. *Applied Geomatics*, *6*(1), 1–15.
Nijland, T. G., Dubelaar, C. W., Van Hees, R. P. J., & Van Der Linden, T. J. M. (2003). Black Weathering of Bentheim and Obernkirchen Sandstone. *Heron*.
Norbury, D., Hencher, S., Cripps, J., & Lumsden, A. (1995). The description and classificatioin of weathered rocks for engineering purposes- Geological Society Engineering Group Working Party Report. *Quarterly Journal of Engineering Geology and Hydrogeology*, *28*(3), 207–242. doi:10.1144/GSL.QJEGH.1995.028.P3.02
O'Neill, A. L. (1994). Reflectance spectra of microphytic soil crusts in semi-arid Australia. *International Journal of Remote Sensing*, *15*(3), 675–681. doi:10.1080/01431169408954106
Ortiz, P., Ortega, F. J., Vázquez, M. A., Martín, J. M., Aparicio, P., Ferruz, J., … Ollero, A. (2013). The Diagnosis of The Royal Tobacco Factory of Seville assisted by Quad-rotor Helicopters. In *RICH 2012 1st Conference on "Robotics Innovation for Cultural Heritage*.
Otoo, J. N. A. (2012). *Surface expressions of discontinuities , and the estimation of their 3-D orientations using combined LiDAR and optical imaging*. Missouri University of Science and Technology.
Palmström, A. (1995). *RMi – a rock mass characterization system for rock engineering purposes*. University Of Oslo.
Patton, F. D., & Deere, D. U. (1970). Significant Geologic factor in rock slope stability. In *In Van Rensburg, PWJ, Planning Open Pit Mines: Proceedings of the Symposium on the Theoretical Background to the Planning of Open Pit Mines with Special Reference to Slope Stability* (pp. 265–274). AA Balkema, Cape Town, Amsterdam.
Phillips, J. D. (2005). Weathering instability and landscape evolution. *Geomorphology*, *67*(1-2), 255–272.
Piatek, J. L., Hardgrove, C., & Moersch, J. E. (2013). Ground-Based Thermal Analysis Of A Terrestrial Rock Glacier As An Analog To Martian Lobate Debris Aprons. In *44th Lunar and Planetary Science Conference* (p. 2936). The Woodlands, Texas.
Pilk, S. (2015). Bad Bentheim climate info | what's the weather like in Bad Bentheim, Germany. Retrieved

November 10, 2015, from http://www.whatstheweatherlike.org/germany/bad-bentheim.htm
Pollefeys, M., Koch, R., Vergauwen, M., & Van Gool, L. (2000). Automated reconstruction of 3D scenes from sequences of images. *ISPRS Journal of Photogrammetry and Remote Sensing*, *55*(4), 251–267.
Potter, N. J., & Helmke, M. (2007). Hickory Run Boulder Field 3: More Observations and New Interpretations. In *2007 GSA Annual Meeting & Exposition* (Vol. 53–30). Denver, Colorado.
Price, D. G. (1995). Weathering and weathering processes. *Quarterly Journal of Engineering Geology and Hydrogeology*, *28*(3), 243–252. doi:10.1144/GSL.QJEGH.1995.028.P3.03
Price, D. G., De Frietas, M. H., Hack, H. R. G. K., Higginbottom, I. E., Knill, J. K., & Maurnenbrecher, M. (2009a). Chapter 3: Geological Masses. In M. (Ed. . de Freitas (Ed.), *Engineering Geology* (pp. 63–90). Springer Berlin Heidelberg. doi:10.1007/978-3-540-68626-2_3
Price, D. G., De Frietas, M. H., Hack, H. R. G. K., Higginbottom, I. E., Knill, J. K., & Maurnenbrecher, M. (2009b). *Engineering Geology : Principles and Practice*. (D. M. H. De Freitas, Ed.)*Engineering Geology*. Springer Berlin Heidelberg.
Price, N. J. (2015). *Fault and Joint Development in Brittle and Semi-Brittle Rock: The Commonwealth and International Library: Geology Division*. Elsevier.
Rango, A., Laliberte, A., Herrick, J. E., Winters, C., Havstad, K., Steele, C., & Browning, D. (2009). Unmanned aerial vehicle-based remote sensing for rangeland assessment, monitoring, and management. *Journal of Applied Remote Sensing*, *3*(1), 033542. doi:10.1117/1.3216822
Reid, T. R., & Harrison, J. P. (2000). A semi-automated methodology for discontinuity trace detection in digital images of rock mass exposures. *International Journal of Rock Mechanics and Mining Sciences*, *37*(7), 1073–1089.
Remondino, F., Barazzetti, L., Nex, F., Scaioni, M., & Sarazzi, D. (2012). UAV Photogrammetry For Mapping And 3d Modeling – Current Status And Future Perspectives. *ISPRS - International Archives of the Photogrammetry, Remote Sensing and Spatial Information Sciences*, *XXXVIII-1/*(September), 25–31.
Rengers, N. (1967). Terrestrial photogrammetry: A valuable tool for engineering geological purposes. *Rock Mechanics and Engineering Geology.*, *V/2-3*, 150–154.
Riaza, A., Strobl, P., Beisl, U., Hausold, A., & Müller, A. (2001). Spectral mapping of rock weathering degrees on granite using hyperspectral DAIS 7915 spectrometer data. *International Journal of Applied Earth Observation and Geoinformation*, *3*(4), 345–354. doi:10.1016/S0303-2434(01)85042-X
Romo, P. E., & Keaton, J. R. (2013). Reconnaissance Documentation of Geologic Structure Using Close-Range Terrestrial Photogrammetry. In *Geo-Congress 2013* (pp. 1578–1586). Reston, VA: American Society of Civil Engineers. doi:10.1061/9780784412787.158
Sabins, F. F. (2007). *Remote Sensing: Principles and Applications, Third Edition*. Waveland Press.
Saliu, M. A., & Lawal, A. I. (2014). Investigations of Weathering Effects on Engineering Properties of Supare Granite Gneiss. *Journal of Mining World Express*, *3*(0), 53. doi:10.14355/mwe.2014.03.008
Sara, M. N. (2003). *Site Assessment and Remediation Handbook, Second Edition*. CRC Press.
Savanick, G. A., & Johnson, D. I. (1974). Measurements of the strength of grain boundaries in rock. *International Journal of Rock Mechanics and Mining Sciences & Geomechanics Abstracts*, *11*(5), 173–180.
Schieber, D. J. (2007). Chapter 5: Minerals, Rocks & Rock Forming Processes. Retrieved July 28, 2015, from http://www.indiana.edu/~geol105/1425chap5.htm
Schnabel, R., Wahl, R., & Klein, R. (2007). Efficient RANSAC for Point-Cloud Shape Detection: Computer Graphics Bonn. *Computer Graphics Forum*, *26*(2), 214–226.
Shrivastava, G. (2014). Influence of Weathering on the Engineering Properties of Basalt near Indore , Madhya Pradesh. *IOSR Journal of Mechanical and Civil Engineering (IOSR-JMCE)*, 18–22.
Slob, S., Hack, H. R. G. K., Feng, Q., Röshoff, K., & Turner, A. K. (2007). Fracture mapping using 3D laser scanning techniques. *1th Congress of the International Society for Rock Mechanics*, *1*, 299–302.
Slob, S., & Hack, R. (2004). 3D Terrestrial Laser Scanning as a New Field Measurement and Monitoring Technique. In *Engineering Geology for Infrasutructure Planning in Europe. A European Perspective* (pp. 179–189).
Slob, S., Hack, R., & Turner, A. (2002). An approach to automate discontinuity measurements of rock faces using laser scanning techniques. *ISRM International Symposium - EUROCK 2002*, 87–94.
Slob, S., Hack, R., Van Knapen, B., & Kemeny, J. (2004). Automated identification and characterization of discontinuity sets in outcropping rock masses using 3D terrestrial laser scan survey techniques. *EUROCK 2004 & 53rd Geomechanics Colloquium. Schubert (ed.).*
Slob, S., Hack, R., Van Knapen, B., Turner, K., & Kemeny, J. (2005). A method for automated discontinuity analysis of rock slope with 3D laser scanning. *TRB 2005 Annual Meeting.*
Slob, S., van Knapen, B., Hack, R., Turner, K., & Kemeny, J. (2005). Method for Automated Discontinuity Analysis of Rock Slopes with Three-Dimensional Laser Scanning. *Transportation Research Record.*
Squarzoni, C., Galgaro, A., Teza, G., Acosta, C. A. T., Pernito, M. A., Bucceri, N., … Padova, U. (2008).

Terrestrial laser scanner and infrared thermography in rock fall prone slope analysis - Preliminary results Introduction Infrared thermography. *Geophysical Research Abstracts*, *10*(1), 3.

St Clair, J., Moon, S., Holbrook, W. S., Perron, J. T., Riebe, C. S., Martel, S. J., … Richter, D. deB. (2015). Geophysical imaging reveals topographic stress control of bedrock weathering. *Science (New York, N.Y.)*, *350*(6260), 534–8. doi:10.1126/science.aab2210

Stanchits, S., Fortin, J., Gueguen, Y., & Dresen, G. (2009). Initiation and Propagation of Compaction Bands in Dry and Wet Bentheim Sandstone. *Pure and Applied Geophysics*, *166*(5-7), 843–868.

Sturzenegger, M., & Stead, D. (2009). Close-range terrestrial digital photogrammetry and terrestrial laser scanning for discontinuity characterization on rock cuts. *Engineering Geology*, *106*(3-4), 163–182.

Tating, F. F. (2015, September 2). *Tropical sandstone degradation with time : case study in Kota Kinabalu Sabah, Malaysia*. University of Twente, Enschede, The Netherlands. doi/10.3990/1.9789036539517

Tating, F., Hack, D. R., & Jetten, P. dr. V. (2013). Weathering and deterioration as quantitative factors in slope design in humid tropical areas : case study Northern. *Ingeokring Newsletter*, *33*, 22–28.

Tating, F., Hack, R., & Jetten, V. (2014). Weathering effects on discontinuity properties in sandstone in a tropical environment: case study at Kota Kinabalu, Sabah Malaysia. *Bulletin of Engineering Geology and the Environment*, 427–441. doi:10.1007/s10064-014-0625-5

Tonon, F., & Kottenstette, J. (2006). Laser and photogrammetric methods for rock face characterization: A workshop. In *Report on a workshop held in Golden, Colorado* (p. 120).

Torres-Sánchez, J., Peña, J. M., de Castro, A. I., & López-Granados, F. (2014). Multi-temporal mapping of the vegetation fraction in early-season wheat fields using images from UAV. *Computers and Electronics in Agriculture*, *103*, 104–113. doi:10.1016/j.compag.2014.02.009

Traska, M. (2014). *Water transport properties in building materials : traditional methods versus CT-based pore network analysis*. Faculty of Sciences, Universiteit Gent.

Turkington, A. V., & Paradise, T. R. (2005). Sandstone weathering: a century of research and innovation. *Geomorphology*, *67*(1-2), 229–253. doi:10.1016/j.geomorph.2004.09.028

Turkington, A. V., Phillips, J. D., & Campbell, S. W. (2005). Weathering and landscape evolution. *Geomorphology*, *67*(1-2), 1–6. doi:10.1016/j.geomorph.2004.08.013

Usamentiaga, R., Venegas, P., Guerediaga, J., Vega, L., Molleda, J., & Bulnes, F. (2014). Infrared Thermography for Temperature Measurement and Non-Destructive Testing. *Sensors*, *14*(7), 12305–12348.

Vasuki, Y., Holden, E. J., Kovesi, P., & Micklethwaite, S. (2014). Semi-automatic mapping of geological Structures using UAV-based photogrammetric data: An image analysis approach. *Computers and Geosciences*, *69*, 22–32. doi:10.1016/j.cageo.2014.04.012

Warke, P. A., & Smith, B. J. (1998). Effects of direct and indirect heating on the validity of rock weathering simulation studies and durability tests. *Geomorphology*, *22*(3-4), 347–357.

Warke, P. A., Smith, B. J., & Magee, R. W. (1996). Thermal Response Characteristics Of Stone: Implications For Weathering Of Soiled Surfaces In Urban Environments. *Earth Surface Processes and Landforms*, *21*(3), 295–306. doi:10.1002/(SICI)1096-9837(199603)21:3<295::AID-ESP637>3.0.CO;2-8

White, K., Bryant, R., & Drake, N. (1998). Techniques For Measuring Rock Weathering: Application To A Dated Fan Segment Sequence In Southern Tunisia. *Earth Surface Processes and Landforms*, *23*, 1031–1043.

Wu, L., Cui, C., Geng, N., & Wang, J. (2000). Remote sensing rock mechanics (RSRM) and associated experimental studies. *International Journal of Rock Mechanics and Mining Sciences*, *37*(6), 879–888.

Yan, W. Y., Shaker, A., & El-Ashmawy, N. (2015). Urban land cover classification using airborne LiDAR data: A review. *Remote Sensing of Environment*, *158*, 295–310. doi:10.1016/j.rse.2014.11.001

APPENDICES

Appendix 1- The overall research workflow scheme (Flow chart).

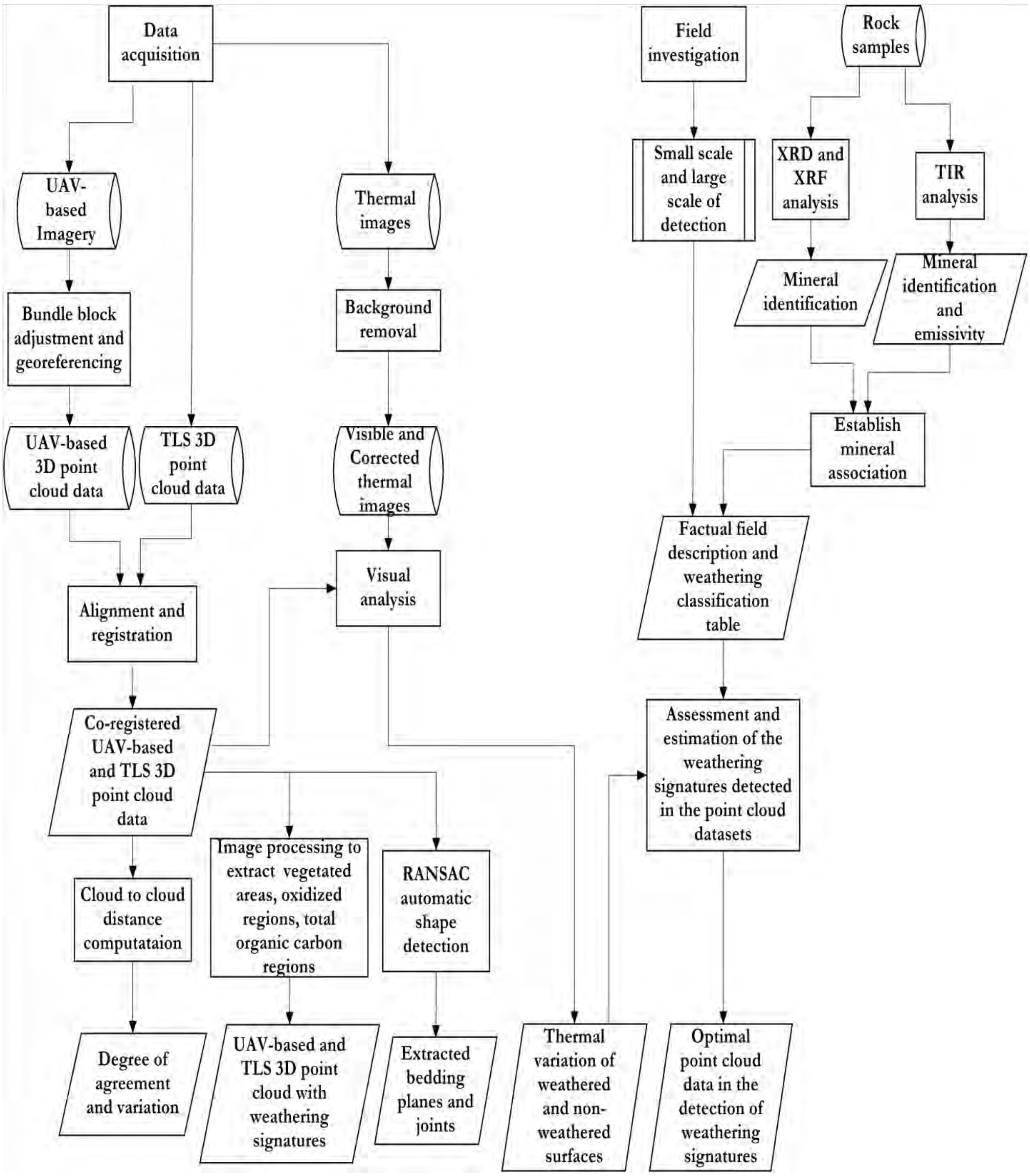

Figure 6-1: Flow chart of the methodology

Appendix 2a- A descriptive classification scheme of the structure referencing the scale in BS BS5930:1999.

Table 6-1: Descriptive terms for the thickness of the structure Source: BS 5930:1999, 1999

Term	Thickness
Very thick	Greater than 2m
Thick	600mm to 2m
Medium	200mm to 600mm
Thin	60mm to 200mm
Very thin	20mm to 60mm
Thickly laminated (Sedimentary Rock) Narrow (Metamorphic and Igneous Rock)	6mm to 20mm
Thinly laminated (Sedimentary Rock) Very narrow (Metamorphic and Igneous Rock)	Less than 6mm

Appendix 2b- A descriptive classification scheme of the grain size for bedded sedimentary rocks, after Table 14 of the BS BS5930:1999.

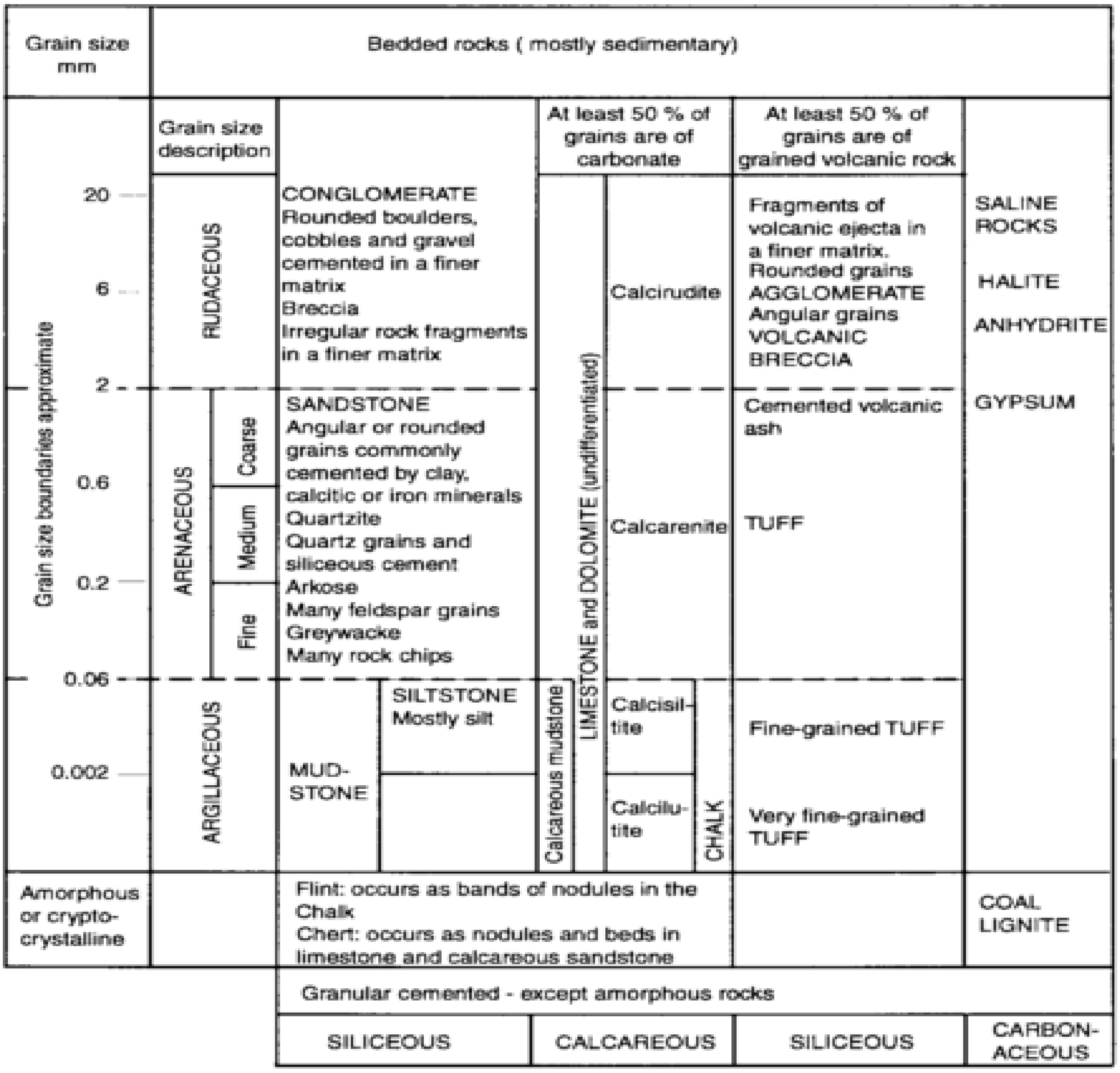

Figure 6-2:Classification scheme of the grain size for bedded sedimentary rocks.

Appendix 2c- The descriptive classification scheme for the simple means method used in the estimation of the intact rock strength referencing the scale in BS BS5930:1999.

Table 6-2: Intact rock strength field classification Source: BS 5930:1999, 1999

Term	**Field definition**	**MPa or MN/m²**
Very weak	Gravel size lumps can be crushed between finger and thumb.	<1.25
Weak	Gravel size lumps can be broken in half by heavy hand pressure.	1.25 to 5
Moderately weak	Only thin slabs, corners or edges can be broken off with heavy hand pressure.	5 to 12.5
Moderately strong	When held in the hand, rock can be broken by hammer blows.	12.5 to 50
Strong	When resting on a solid surface, rock can be broken by hammer blows.	50 to 100
Very strong	Rock chipped by heavy hammer blows.	100 to 200
Extremely strong	Rock rings on hammer blows. Only broken by sledgehammer	> 200

Appendix 2d- The weathering descriptive parameters classification scheme according to the BS5930: 1981 and incorporating the SSPC system.

Table 6-3: Description and classification of a weathered rock mass following BS5930:1981 incorporating the SSPC system

Grade	**(Classifier)**	**Typical Characteristics**	**WE**
I	Fresh	No visible sign of rock material weathering; perhaps slight discoloration on major discontinuity surfaces.	1
II	Slightly weathered	Discoloration indicates weathering of rock material and discontinuity surfaces. All the rock material may be discoloured by weathering.	0.95
III	Moderately weathered	Less than half of the rock material is decomposed or disintegrated to a soil. Fresh or discoloured rock is present either as a continuous framework or as core stones.	
IV	Highly weathered	More than half of the rock material is decomposed or disintegrated to a soil. Fresh or discoloured rock is present either as a discontinuous framework or as core stones.	0.90
V	Completely weathered	All rock material is decomposed and/or disintegrated to soil. The original mass structure is still largely intact.	0.62
VI	Residual soil	All rock material is converted to soil. The mass structure and material fabric are destroyed. There is a large change in volume, but the soil has not been significantly transported.	0.35

Appendix 3- The standard SSPC forms used in studied slope at the quarry Gildehaus.

The weathering and slope stability probability classifications (SSPC) was conducted for each of the geotechnical units (with 1[1] for Unit A, 2[1] for Unit B, and 3[1] for Unit C) on the studied slope in the quarry Gildehaus using the standard form designed for probabilistic classification after Hack (1998) and approaches 1 and 2 of the BS 5930:1999.

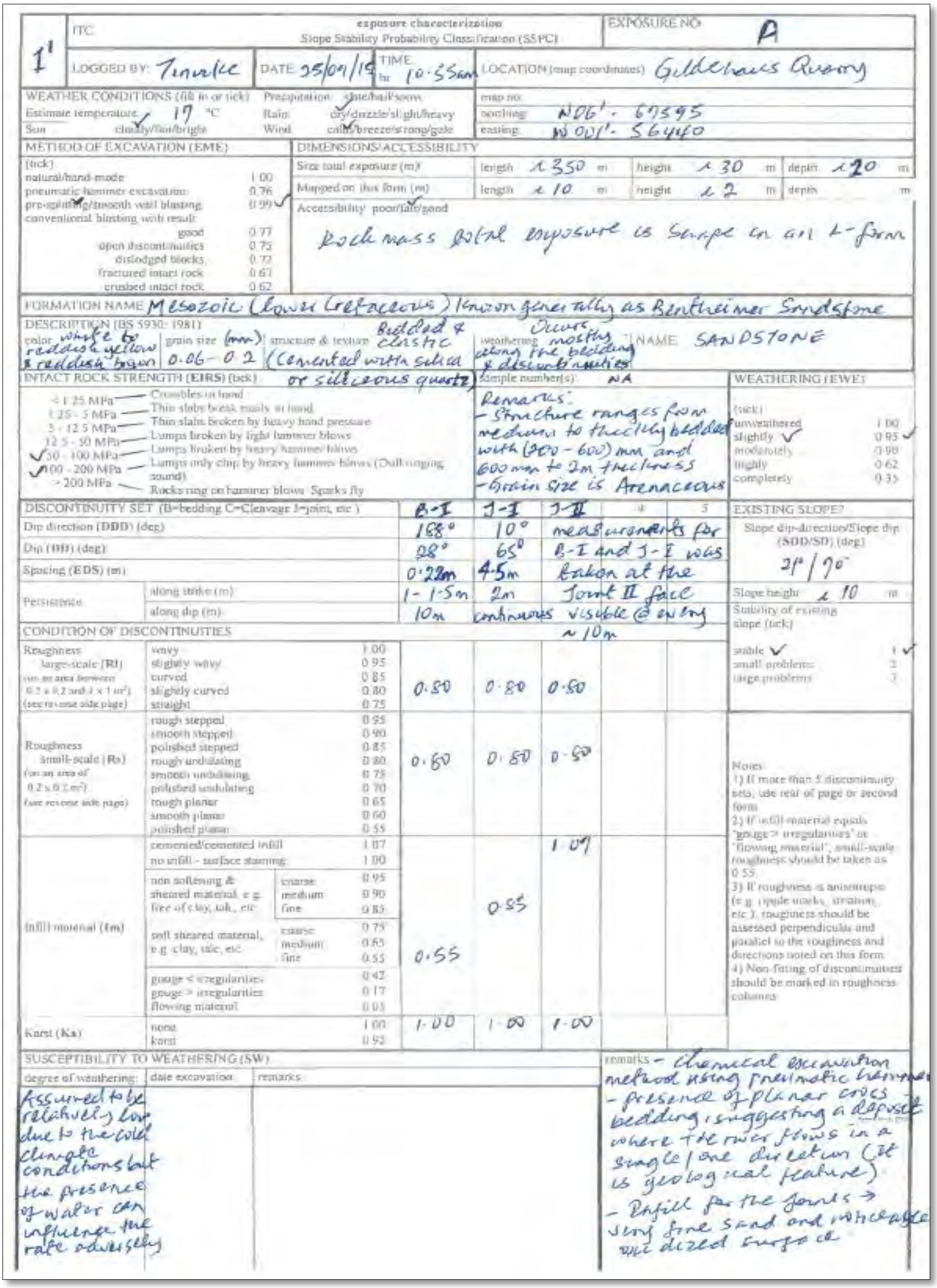

1[1]

ITC — exposure characterization — Slope Stability Probability Classification (SSPC) — EXPOSURE NO: A

LOGGED BY: Tinuke | DATE: 25/04/19 | TIME hr: 10·55am | LOCATION (map coordinates): Gildehaus Quarry

WEATHER CONDITIONS (fill in or tick): Estimate temperature 17 °C; Sun: cloudy/fair/bright; Precipitation: snow/hail/snow; Rain: dry/drizzle/slight/heavy; Wind: calm/breeze/strong/gale

map no: | northing: N06'. 67595 | easting: W001'. 56460

METHOD OF EXCAVATION (EME) (tick): natural/hand-made 1.00; pneumatic hammer excavation 0.76; pre-splitting/smooth wall blasting 0.99 ✓; conventional blasting with result: good 0.77, open discontinuities 0.75, dislodged blocks 0.72, fractured intact rock 0.67, crushed intact rock 0.62

DIMENSIONS/ACCESSIBILITY: Size total exposure (m): length ~350 m, height ~30 m, depth ~20 m; Mapped on this form (m): length ~10 m, height ~2 m, depth m; Accessibility poor/fair/good

Rock mass total exposure is shape in an L-form

FORMATION NAME: Mesozoic (Lower Cretaceous) known generally as Bentheimer Sandstone

DESCRIPTION (BS 5930: 1981): color: white to reddish yellow & reddish brown | grain size (mm): 0.06 - 0.2 | structure & texture: Bedded & clastic (Cemented with silica or siliceous quartz) | weathering: Occurs mostly along the bedding & discontinuities | NAME: SANDSTONE

INTACT ROCK STRENGTH (EIRS) (tick): < 1.25 MPa — Crumbles in hand; 1.25 - 5 MPa — Thin slabs break easily in hand; 5 - 12.5 MPa — Thin slabs broken by heavy hand pressure; 12.5 - 50 MPa — Lumps broken by light hammer blows; ✓ 50 - 100 MPa — Lumps broken by heavy hammer blows; ✓ 100 - 200 MPa — Lumps only chip by heavy hammer blows (Dull ringing sound); > 200 MPa — Rocks ring on hammer blows. Sparks fly

sample number(s): NA

Remarks: - Structure ranges from medium to thickly bedded with (200 - 600) mm and 600 mm to 2m thickness - Grain size is Arenaceous

WEATHERING (EWE) (tick): unweathered 1.00; slightly ✓ 0.95 ✓; moderately 0.90; highly 0.62; completely 0.35

DISCONTINUITY SET (B=bedding C=Cleavage J=joint, etc.)		B-I	J-I	J-II	4	5
Dip direction (DDD) (deg)		188°	10°	measurements for		
Dip (DD) (deg)		28°	65°	B-I and J-I was		
Spacing (EDS) (m)		0·22m	4·5m	taken at the		
Persistence	along strike (m)	1 - 1·5m	2m	Joint II face		
	along dip (m)	10m	continuous visible @ every ~10m			

EXISTING SLOPE? Slope dip-direction/Slope dip (SDD/SD) (deg): 21° / 70°; Slope height ~10 m; Stability of existing slope (tick): stable ✓ 1 ✓; small problems 2; large problems 3

CONDITION OF DISCONTINUITIES			B-I	J-I	J-II	4	5
Roughness large-scale (Rl) (on an area between 0.2 x 0.2 and 1 x 1 m²) (see reverse side page)	wavy 1.00; slightly wavy 0.95; curved 0.85; slightly curved 0.80; straight 0.75		0.80	0·80	0·80		
Roughness small-scale (Rs) (on an area of 0.2 x 0.2 m²) (see reverse side page)	rough stepped 0.95; smooth stepped 0.90; polished stepped 0.85; rough undulating 0.80; smooth undulating 0.75; polished undulating 0.70; rough planar 0.65; smooth planar 0.60; polished planar 0.55		0·80	0·80	0·80		
Infill material (Im)	cemented/cemented infill 1.07; no infill - surface staining 1.00				1·07		
	non softening & sheared material, e.g. free of clay, talc, etc	coarse 0.95; medium 0.90; fine 0.85		0·55			
	soft sheared material, e.g. clay, talc, etc	coarse 0.75; medium 0.65; fine 0.55	0·55				
	gouge < irregularities 0.42; gouge > irregularities 0.17; flowing material 0.05						
Karst (Ka)	none 1.00; karst 0.92		1·00	1·00	1·00		

Notes: 1) If more than 5 discontinuity sets, use rear of page or second form. 2) If infill material equals "gouge > irregularities" or "flowing material", small-scale roughness should be taken as 0.55. 3) If roughness is anisotropic (e.g. ripple marks, striation, etc.), roughness should be assessed perpendicular and parallel to the roughness and directions noted on this form. 4) Non-fitting of discontinuities should be marked in roughness columns.

SUSCEPTIBILITY TO WEATHERING (SW): degree of weathering: Assumed to be relatively low due to the cold climate conditions but the presence of water can influence the rate adversely | date excavation: | remarks:

remarks - Chemical excavation method using pneumatic hammer - presence of planar cross bedding, suggesting a deposit where the river flows in a single/one direction (It is geological feature) - Infill for the joints → very fine sand and oxidized surface

2'

ITC	**exposure characterization** Slope Stability Probability Classification (SSPC)	EXPOSURE NO: B

LOGGED BY: Tenuke | DATE: 07/10/15 | TIME: 11.02 am hr | LOCATION (map coordinates): Geldehaus Quarry

WEATHER CONDITIONS (fill in or tick)
Estimate temperature: 16 °C
Sun: cloudy/fair/bright
Precipitation: slate/hail/snow
Rain: dry/drizzle/slight/heavy
Wind: calm/breeze/strong/gale
map no:
northing:
easting:

METHOD OF EXCAVATION (EME)
(tick)

natural/hand-made:	1.00
pneumatic hammer excavation:	0.76
pre-splitting/smooth wall blasting:	0.99 ✓
conventional blasting with result:	
good:	0.77
open discontinuities:	0.75
dislodged blocks:	0.72
fractured intact rock:	0.67
crushed intact rock:	0.62

DIMENSIONS/ACCESSIBILITY

Size total exposure (m):	length: ~350 m	height: ~30 m	depth: ~20 m
Mapped on this form (m):	length: ~10 m	height: ~2 m	depth: m

Accessibility: poor/fair/good

Rock mass in this region is extremely damp, very slippery

FORMATION NAME: Mesozoic (Lower Cretaceous) - Bontheimer Sand stone

DESCRIPTION (BS 5930: 1981)
color: Dark grey to dark greyish green | grain size: (mm) 0.002 - 0.2 | structure & texture: Bedded & Clastic (Cemented with silica or Siliceous quartz) | weathering: Over the exposed rock unit | NAME: SANDSTONE

INTACT ROCK STRENGTH (EIRS) (tick)

< 1.25 MPa	Crumbles in hand
1.25 - 5 MPa	Thin slabs break easily in hand
5 - 12.5 MPa	Thin slabs broken by heavy hand pressure
✓12.5 - 50 MPa	Lumps broken by light hammer blows
✓50 - 100 MPa	Lumps broken by heavy hammer blows (75 MPa)
100 - 200 MPa	Lumps only chip by heavy hammer blows (Dull ringing sound)
> 200 MPa	Rocks ring on hammer blows. Sparks fly

sample number(s): NA
Remarks:
- Structure ranges from medium to thickly bedded - 200 mm to 600 mm and 600 m to 2 m thickness.
- Grain size is mostly Arenaceous with regions of Argillaceous

WEATHERING (EWE)
(tick)

unweathered	1.00
slightly	0.95
moderately	0.90
highly ✓	0.62 ✓
completely	0.35

DISCONTINUITY SET (B=bedding C=Cleavage J=joint, etc.)		B-I	J-I	J-II	...4	...5
Dip direction (DDD) (deg):		180°	10°	107°		
Dip (DD) (deg):		20°	65°	80°		
Spacing (EDS) (m):		0-25m	~4m	10m		
Persistence:	along strike (m):	0.6m	2m			
	along dip (m):	←	continuous	→		

EXISTING SLOPE?
Slope dip-direction/Slope dip (SDD/SD) (deg): 21°/70°
Slope height: ~10 m
Stability of existing slope (tick):

stable	1
small problems ✓	2
large problems	3

CONDITION OF DISCONTINUITIES

			B-I	J-I	J-II	...4	...5
Roughness large-scale (Rl) (on an area between 0.2 x 0.2 and 1 x 1 m²) (see reverse side page)	wavy	1.00					
	slightly wavy	0.95					
	curved	0.85					
	slightly curved	0.80	0.80	0.80	0.80		
	straight	0.75					
Roughness small-scale (Rs) (on an area of 0.2 x 0.2 m²) (see reverse side page)	rough stepped	0.95					
	smooth stepped	0.90					
	polished stepped	0.85					
	rough undulating	0.80					
	smooth undulating	0.75	0.75	0.75	0.80		
	polished undulating	0.70					
	rough planar	0.65					
	smooth planar	0.60					
	polished planar	0.55					
Infill material (Im)	cemented/cemented infill	1.07					
	no infill - surface staining	1.00					
	non softening & sheared material, e.g. free of clay, talc, etc.: coarse	0.95					
	medium	0.90					
	fine	0.85					
	soft sheared material, e.g. clay, talc, etc.: coarse	0.75					
	medium	0.65					
	fine	0.55	0.55	0.55	0.55		
	gouge < irregularities	0.42					
	gouge > irregularities	0.17					
	flowing material	0.05					
Karst (Ka)	none	1.00	1.00	1.00	1.00		
	karst	0.92					

Notes:
1) If more than 5 discontinuity sets; use rear of page or second form.
2) If infill material equals 'gouge > irregularities' or 'flowing material'; small-scale roughness should be taken as 0.55.
3) If roughness is anisotropic (e.g. ripple marks, striation, etc.); roughness should be assessed perpendicular and parallel to the roughness and directions noted on this form.
4) Non-fitting of discontinuities should be marked in roughness columns.

SUSCEPTIBILITY TO WEATHERING (SW)

degree of weathering:	date excavation:	remarks:
moderate to highly		The influence of water is plainly seen in this region resulting to higher weathering susceptibility than the surrounding units.

remarks:
- Moist rock mass unit
- presence of roots & lichens and grass vegetation

3'

ITC	exposure characterization Slope Stability Probability Classification (SSPC)	EXPOSURE NO: C
LOGGED BY: Tinuke	DATE: 28/10/15 TIME hr: 11·30am	LOCATION (map coordinates): Gildehaus Quarry

WEATHER CONDITIONS (fill in or tick)			
Estimate temperature: 9 °C	Precipitation: slate/hail/snow	map no:	
Sun: cloudy/fair/bright ✓cloudy	Rain: dry/drizzle/slight/heavy ✓	northing:	
	Wind: calm/breeze/strong/gale ✓breeze	easting:	

METHOD OF EXCAVATION (EME) (tick)	
natural/hand-made	1.00
pneumatic hammer excavation	0.76
pre-splitting/smooth wall blasting	0.99 ✓
conventional blasting with result: good	0.77
open discontinuities	0.75
dislodged blocks	0.72
fractured intact rock	0.67
crushed intact rock	0.62

DIMENSIONS/ACCESSIBILITY			
Size total exposure (m):	length: ≈ 350 m	height: ≈ 30 m	depth: ≈20 m
Mapped on this form (m):	length: ≈ 10 m	height: ≈ 2 m	depth: m
Accessibility: poor/fair/good ✓fair			

FORMATION NAME: Mesozoic (Lower Cretaceous) - Bentheimer Sandstone

DESCRIPTION (BS 5930: 1981) color	grain size (mm)	structure & texture	weathering	NAME
light reddish brown to greyish green	0.06 - 0.2	bedded & clastic (cemented with silica / siliceous quartz)	slightly weathered with cemented grains to moderately weathered	SANDSTONE

INTACT ROCK STRENGTH (EIRS) (tick)		
< 1.25 MPa	Crumbles in hand	
1.25 - 5 MPa	Thin slabs break easily in hand	
5 - 12.5 MPa	Thin slabs broken by heavy hand pressure	
12.5 - 50 MPa	Lumps broken by light hammer blows	
✓ 50 - 100 MPa	Lumps broken by heavy hammer blows	75 MPa
100 - 200 MPa	Lumps only chip by heavy hammer blows (Dull ringing sound)	
> 200 MPa	Rocks ring on hammer blows. Sparks fly	

sample number(s): NA

Remarks:
- No recent exposed fresh surface
- Oxidation of exposed rock mass unit
- Presence of moss & lichen

WEATHERING (EWE) (tick)	
unweathered	1.00
slightly	0.95
moderately ✓	0.90 ✓
highly	0.62
completely	0.35

DISCONTINUITY SET (B=bedding C=Cleavage J=joint, etc.)		B-III	J-I	J-II	4	5
Dip direction (DDD) (deg)		294°	107°	measurements		
Dip (DD) (deg)		15°	80°	for B-III and J-II		
Spacing (EDS) (m)		0·25m	10m	was taken at the		
Persistence	along strike (m)			J-I face occurring		
	along dip (m)	→ continuous		at ≈ 4m		

CONDITION OF DISCONTINUITIES			B-III	J-I	J-II	4	5
Roughness large-scale (Rl) (on an area between 0.2 x 0.2 and 1 x 1 m²) (see reverse side page)	wavy	1.00					
	slightly wavy	0.95					
	curved	0.85					
	slightly curved	0.80	0·80	0·80	0·80		
	straight	0.75					
Roughness small-scale (Rs) (on an area of 0.2 x 0.2 m²) (see reverse side page)	rough stepped	0.95					
	smooth stepped	0.90					
	polished stepped	0.85					
	rough undulating	0.80		0·80			
	smooth undulating	0.75	0·75		0·75		
	polished undulating	0.70					
	rough planar	0.65					
	smooth planar	0.60					
	polished planar	0.55					
Infill material (Im)	cemented/cemented infill	1.07	1·07	1·07			
	no infill - surface staining	1.00					
	non softening & sheared material, e.g. free of clay, talc, etc. — coarse	0.95					
	medium	0.90					
	fine	0.85					
	soft sheared material, e.g. clay, talc, etc. — coarse	0.75					
	medium	0.65			0·65		
	fine	0.55					
	gouge < irregularities	0.42					
	gouge > irregularities	0.17					
	flowing material	0.05					
Karst (Ka)	none	1.00	1·00	1·00	1·00		
	karst	0.92					

EXISTING SLOPE?

Slope dip-direction/Slope dip (SDD/SD) (deg): 21°/90°

Slope height: ≈ 10 m

Stability of existing slope (tick)	
stable ✓	1
small problems	2
large problems	3

Notes:
1) If more than 5 discontinuity sets, use rear of page or second form.
2) If infill material equals 'gouge > irregularities' or 'flowing material', small-scale roughness should be taken as 0.55.
3) If roughness is anisotropic (e.g. ripple marks, striation, etc.), roughness should be assessed perpendicular and parallel to the roughness and directions noted on this form.
4) Non-fitting of discontinuities should be marked in roughness columns.

SUSCEPTIBILITY TO WEATHERING (SW)

degree of weathering	date excavation	remarks
Slightly weathered to moderately weathered		Possibility of ongoing chemical weathering as a result of high presence of moss & lichen. Noticeable oxidation of the exposed rock mass unit due to the interaction with oxygen and water.

- Presence of vegetation on the rock mass surface

Appendix 4- Specification of TH9100PMV infrared Thermal camera.

TH9100PMV thermal infrared camera is a non-contact and highly sensitive infrared radiometric camera. It detects radiant energy, in the 8–14 μm wave bands, emitted from the object of interest and converted to an electric signal by the two-dimensional un-cooled focal plane array detector, and the amplified analog temperature signal is converted to a digital signature which is displayed as a thermal image.

<table>
<tr><td colspan="2" rowspan="2">Parameters</td><td colspan="2">TH9100PMVI</td><td colspan="2">TH9100PMVI</td></tr>
<tr><td>Range 1</td><td>Range 2</td><td>Range 1</td><td>Range 2</td></tr>
<tr><td colspan="2">Measuring range (Temp. calibration range)</td><td>-20 to 100^{0}C
0 to 100^{0}C</td><td>0 to 250^{0}C
0 to 250^{0}C</td><td>-40 to 120^{0}C
0 to 120^{0}C</td><td>0 to 500^{0}C
0 to 500^{0}C</td></tr>
<tr><td colspan="2">Temperature setup level</td><td>-20 to 100^{0}C</td><td>0 to 250^{0}C</td><td>-40 to 120^{0}C</td><td>0 to 500^{0}C</td></tr>
<tr><td rowspan="3">Minimum detectable temp. difference (Temperature calibration range)</td><td>60 Frame/sec</td><td>0.06^{0}C@30^{0}C</td><td>0.15^{0}C@30^{0}C</td><td>0.08^{0}C@30^{0}C</td><td>0.30^{0}C@30^{0}C</td></tr>
<tr><td>∑16</td><td>0.03^{0}C@30^{0}C</td><td>0.08^{0}C@30^{0}C</td><td>0.04^{0}C@30^{0}C</td><td>0.15^{0}C@30^{0}C</td></tr>
<tr><td>∑64</td><td>0.02^{0}C@30^{0}C</td><td>0.06^{0}C@30^{0}C</td><td>0.03^{0}C@30^{0}C</td><td>0.12^{0}C@30^{0}C</td></tr>
<tr><td colspan="2">Resolution</td><td colspan="4">1.2 cm at a distance of 10 m</td></tr>
<tr><td colspan="2">Measurement accuracy</td><td colspan="4">+/-2^{0}C or +/-2 % reading whichever is greater.
For ambient temp. 0 to 40^{0}C, the standard lens use and the measurement distance of 50cm</td></tr>
<tr><td colspan="2">Spectral range</td><td colspan="4">8 to 14 μm</td></tr>
<tr><td colspan="2">Detector</td><td colspan="4">Un-cooled focal plane array (micro bolometer)</td></tr>
<tr><td colspan="2">Field of view</td><td colspan="4">21.7^0 (Horizontal) x 16.4^0 (Vertical)</td></tr>
<tr><td colspan="2">I.F.O.V</td><td colspan="4">When the 1.2mrad standard lens is attached</td></tr>
<tr><td colspan="2">Focus range</td><td colspan="4">30cm to infinity</td></tr>
<tr><td colspan="2">Frame time</td><td colspan="4">60 frames/sec</td></tr>
<tr><td colspan="2">Number of pixels</td><td colspan="4">320(H) x 240(V) pixels</td></tr>
<tr><td colspan="2">A/D resolution</td><td colspan="4">14 bits</td></tr>
<tr><td colspan="2">Emissivity correction</td><td colspan="4">0.10 to 1.00 (0.01 step both in the Run and Freeze mode)</td></tr>
<tr><td colspan="2">Measuring function</td><td colspan="4">Run/Freeze</td></tr>
<tr><td colspan="2">Memory system</td><td colspan="4">Infrared image: SIT, BMP
Visible image: SIT, JPEG</td></tr>
<tr><td colspan="2">Data Display</td><td colspan="4">Color bar: Gray scale, Temp. scale</td></tr>
<tr><td colspan="2">Correction of measurement condition</td><td colspan="4">Correction by inputting outside temperature, humidity, distance for the object</td></tr>
</table>

Appendix 5a- Mineral composition results of the rock samples carried out using PXRD

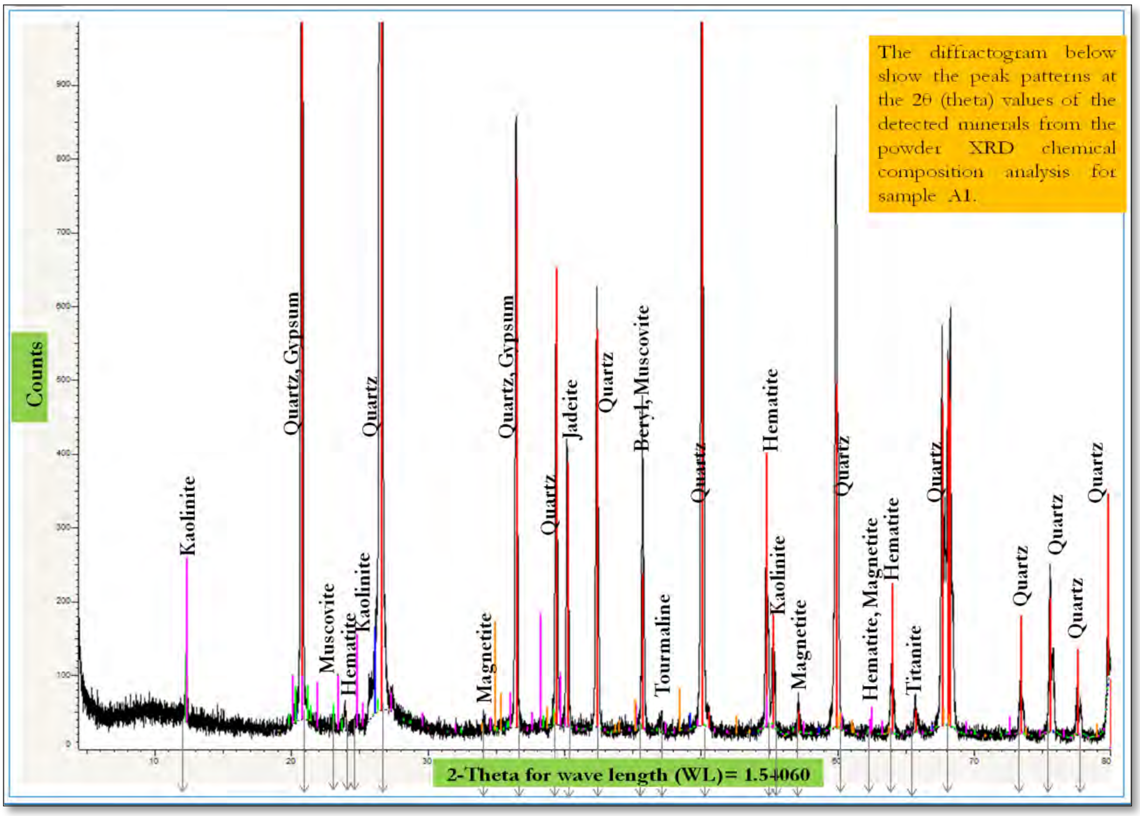

(a)

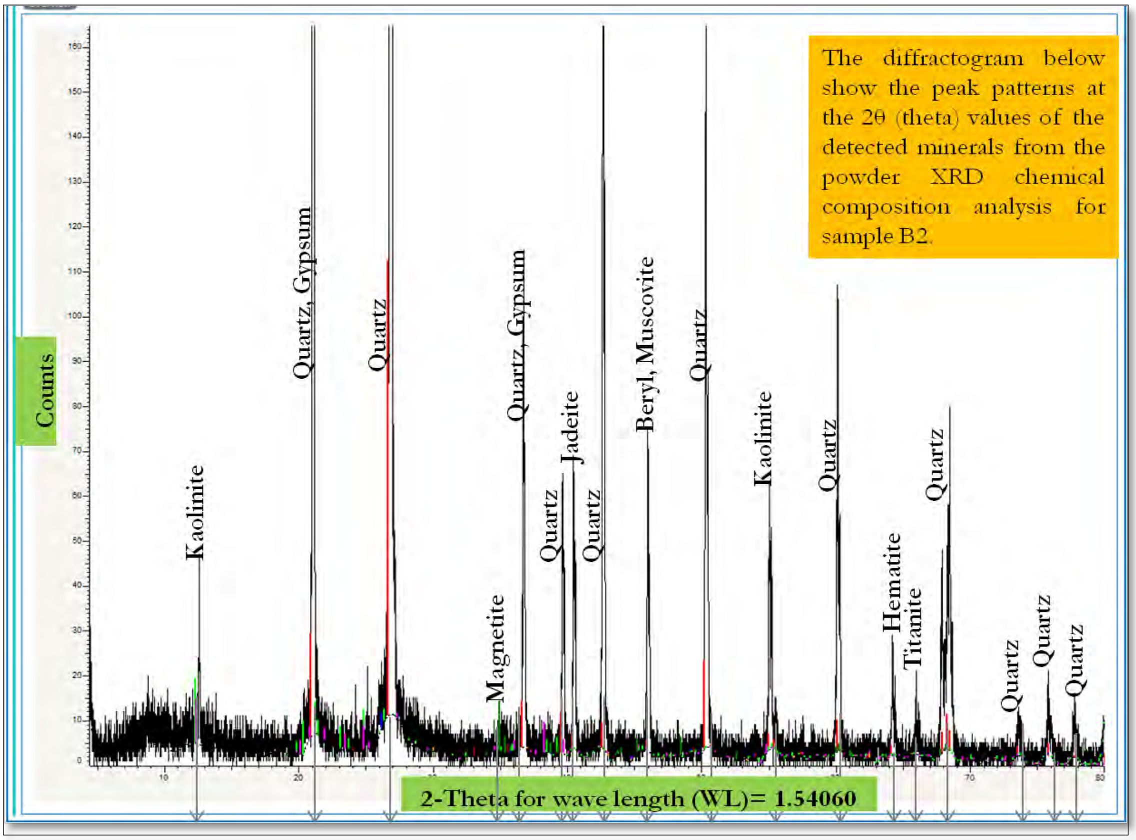

(b)

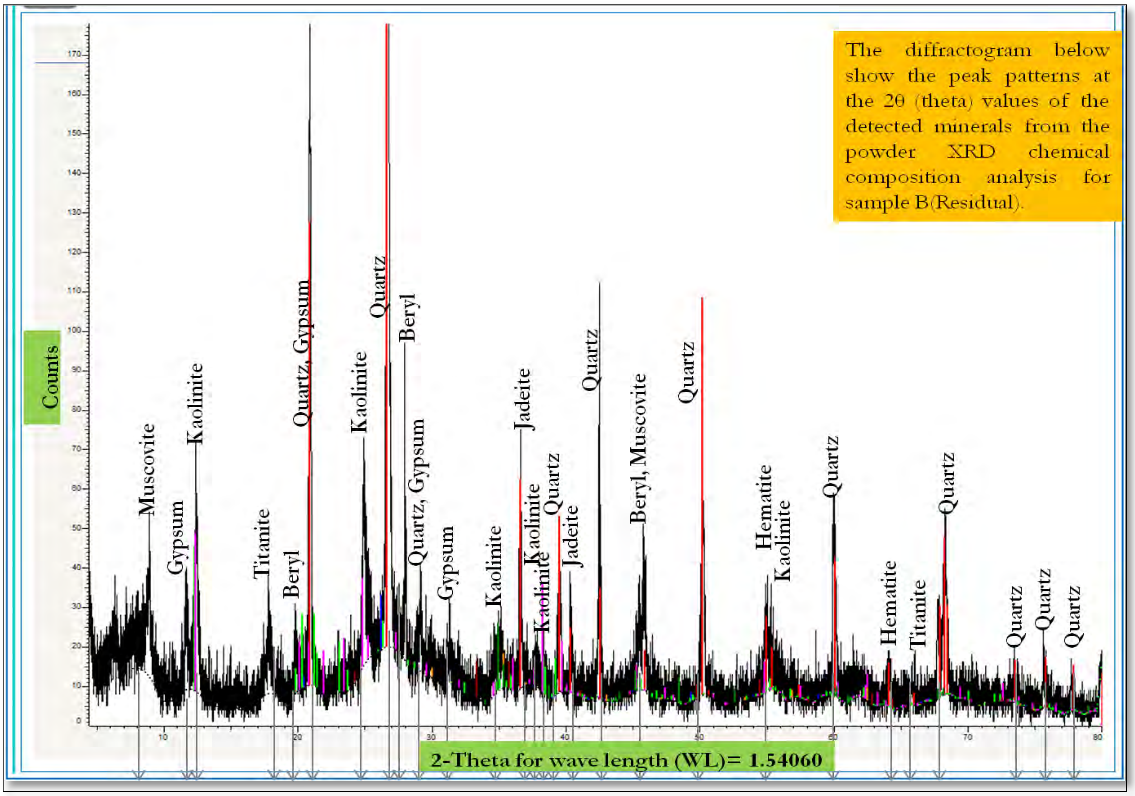

(c)

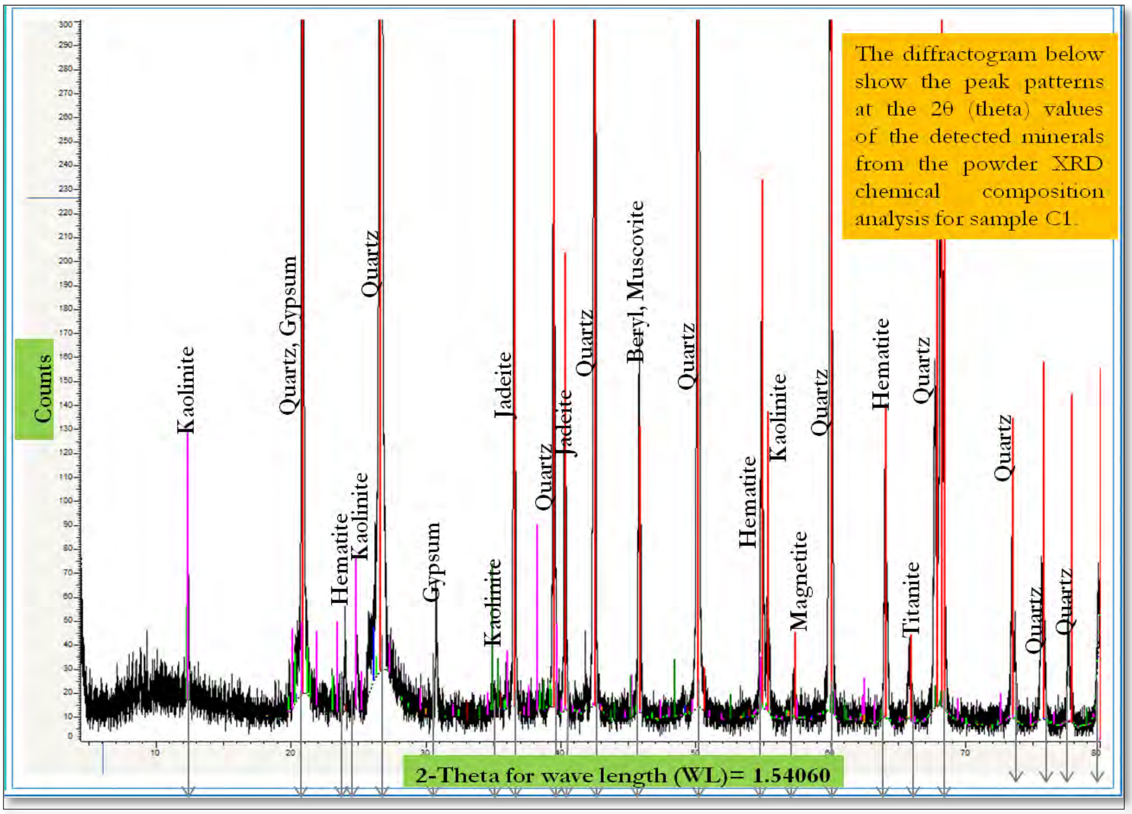

(d)

Figure 6-3: X-ray diffractogram (XRD) for samples taken from each of the geotechnical units of the Gildehaus Slope. (a) represents sample A1 from unit A, (b) represents sample B2 from unit B, (c) represents sample B (residual) from unit B and (d) represents sample C1 from unit C (the arrow lines below the peaks have no meaning and are only for identification).

Appendix 5b- Clay mineralogy results of the rock samples by pipette method analysed using PXRD

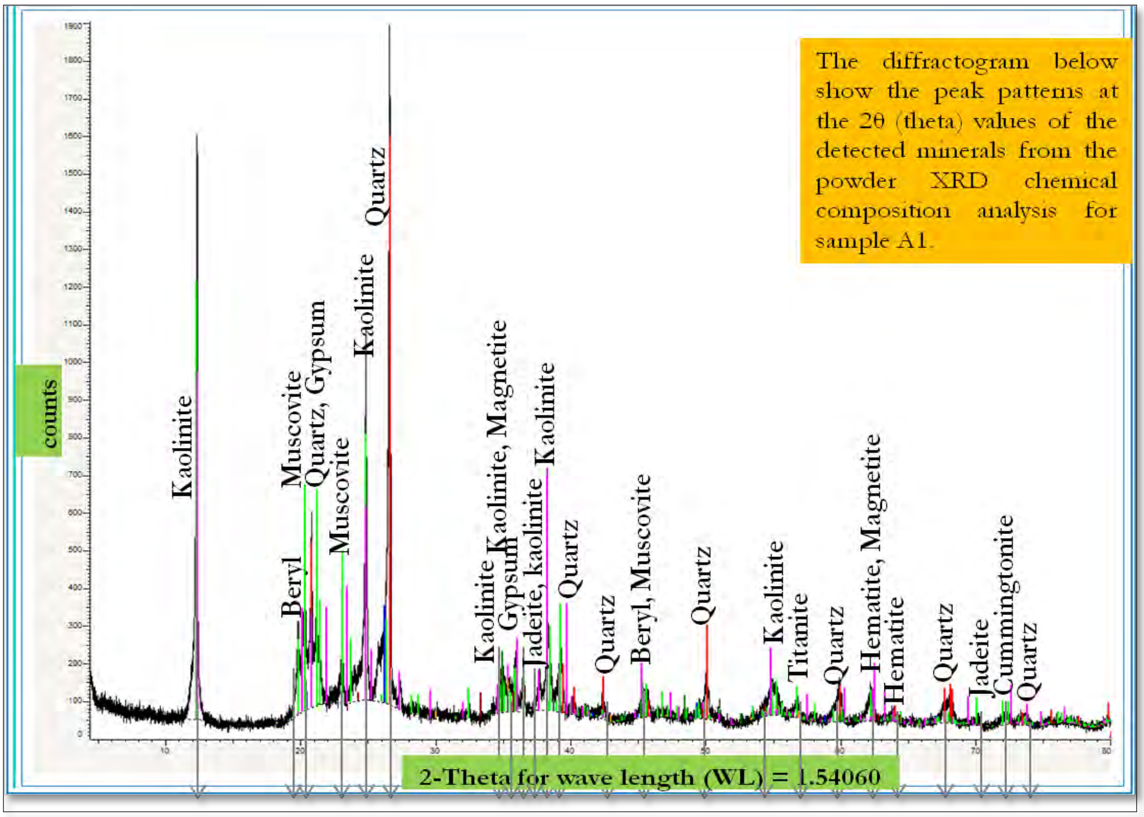

(a)

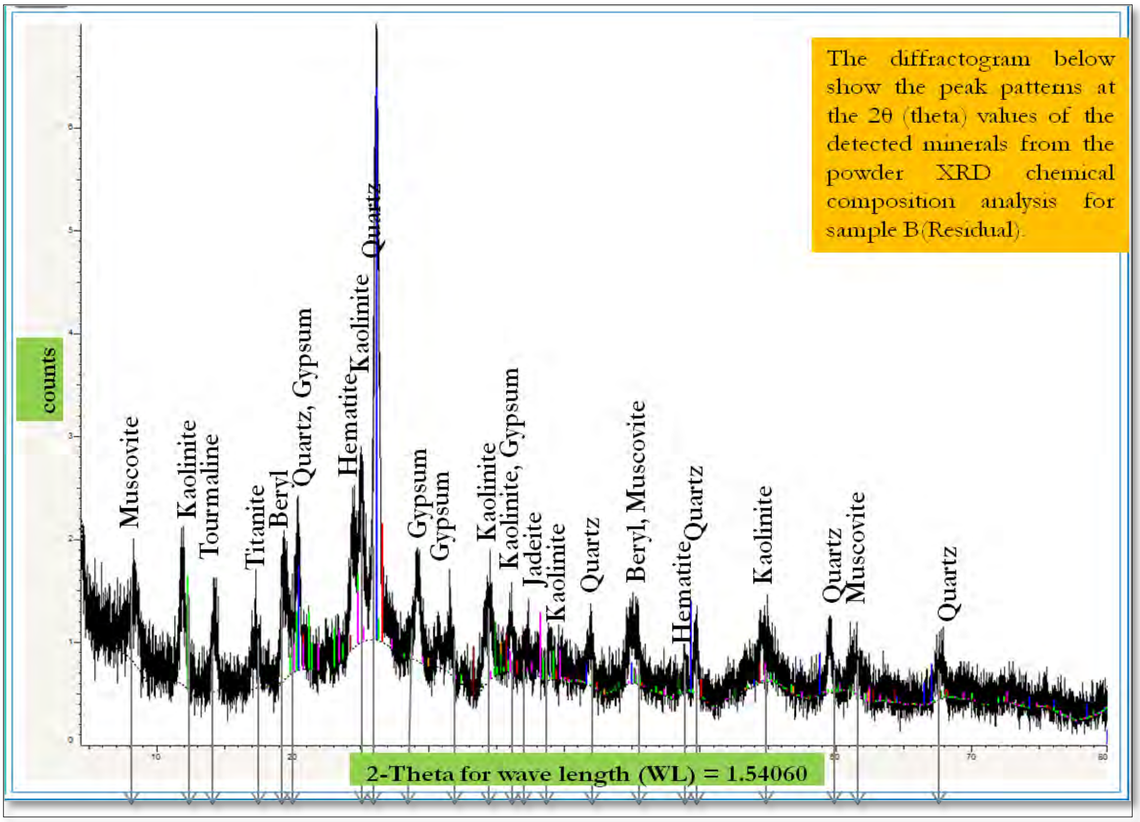

(b)

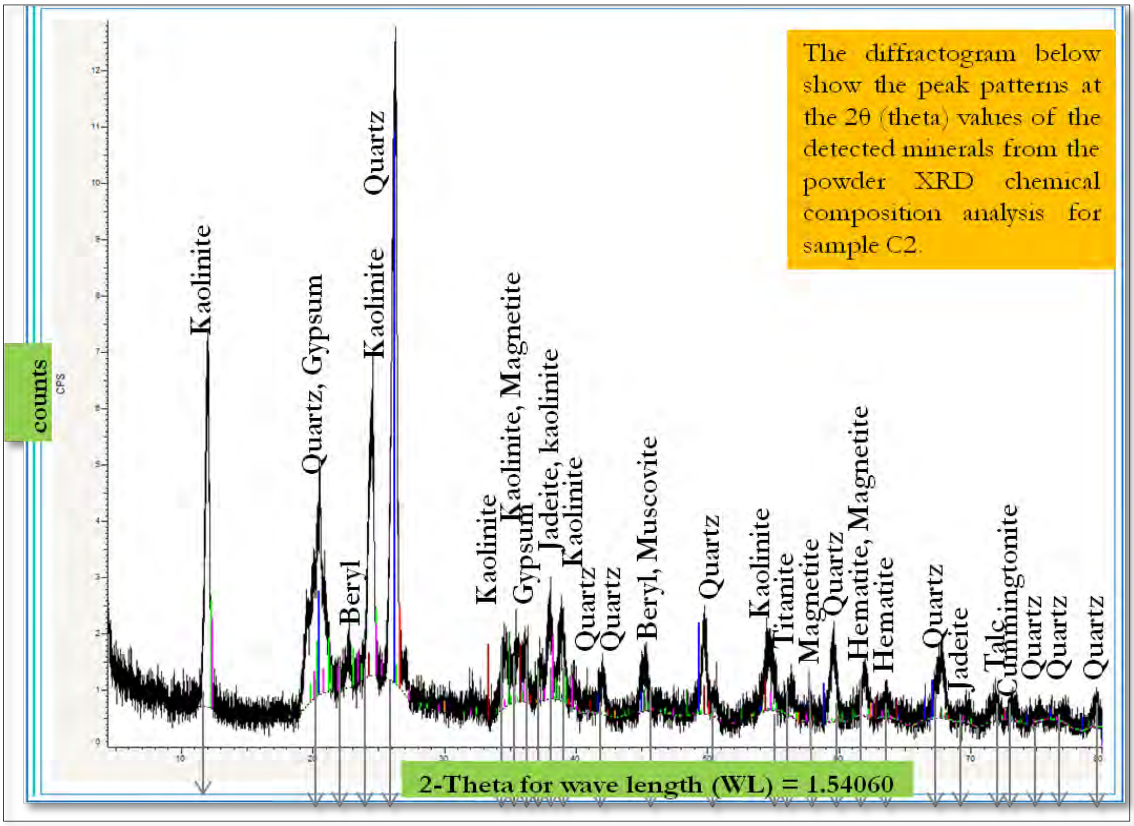

(c)

Figure 6-4: X-ray diffractogram (XRD) from the pipette test method for samples taken from each of the geotechnical units of the Gildehaus Slope. (a) represents sample A1 from unit A, (b) represents sample B(residual) from unit B and (c) represents sample C2 from unit C (the arrow lines below the peaks have no meaning and are only for identification).

Appendix 6- Results from the spectral analysis of the rock samples using portable X-ray Fluorescence (XRF) analyzer.

Index	Reading No	Type	Duration	Units	SAMPLE	Fe	Fe %	Fe Error	Fe %	Ca	Ca %	Ca Error	Ca %	K	K %	K Error	K %
3	117	Soil	92	ppm	NWG-01	81001	**8.10**	485	0.05	**75043**	**7.50**	577	0.06	**9498**	**0.95**	294	0.03
4	118	Soil	91.74	ppm		388	**0.04**	34	0.00	**137**	**0.01**	25	0.00	**4711**	**0.47**	93	0.01
5	119	Soil	91.25	ppm		360	**0.04**	33	0.00	**89**	**0.01**	20	0.00	**3298**	**0.33**	75	0.01
6	120	Soil	91.25	ppm		1652	**0.17**	57	0.01	**87**	**0.01**	33	0.00	**8917**	**0.89**	135	0.01
7	121	Soil	90.61	ppm		58836	**5.88**	363	0.04	**302**	**0.03**	57	0.01	**3487**	**0.35**	155	0.02
8	122	Soil	91.31	ppm		713	**0.07**	41	0.00	**188**	**0.02**	24	0.00	**3943**	**0.39**	83	0.01
9	123	Soil	91.45	ppm		5858	**0.59**	105	0.01	**767**	**0.08**	45	0.00	**8197**	**0.82**	137	0.01
10	124	Soil	91.12	ppm		1507	**0.15**	56	0.01	**347**	**0.03**	33	0.00	**5795**	**0.58**	110	0.01
11	125	Soil	91.52	ppm		1113	**0.11**	49	0.00	**159**	**0.02**	26	0.00	**4794**	**0.48**	95	0.01
12	126	Soil	91.28	ppm		66700	**6.67**	378	0.04	**489**	**0.05**	91	0.01	**4768**	**0.48**	232	0.02

Fe - Iron, Ca - Calcuim, K - Potassium

Ti	Ti Error	Ba	Ba Error	Te	Te Error	Cs	Cs Error	Sb	Sb Error	Zr	Zr Error	Sr	Sr Error	Rb	Rb Error	Pb	Pb Error
12998	200	940	42	74	33	89	11	26	13	258	7	800	11	60	4	< LOD : 6.59	
327	22	299	29	115	25	66	8	41	10	24	2	9	1	8	1	12	3
310	20	343	31	159	27	84	9	53	11	34	2	10	1	7	1	10	3
1391	37	340	28	107	24	70	8	32	9	65	3	20	2	16	2	28	4
730	57	489	33	227	29	123	9	73	11	36	3	10	2	8	2	266	13
329	21	311	29	130	26	67	8	40	10	35	2	10	1	9	1	8	3
1513	40	414	31	176	27	92	9	50	11	50	3	18	2	20	2	39	5
858	31	310	28	103	25	71	8	38	10	29	2	9	1	9	1	18	4
680	27	351	29	145	26	73	8	48	10	37	2	11	1	11	2	17	4
833	81	402	31	212	27	98	9	72	11	53	3	8	1	7	2	133	9

Ti - Titanium, Ba - Barium, Te - Tellurium, Cs - Cesium, Sb - Antimony, Zr - Zirconium, Sr - Strontium, Rb - Rubidium, Pb - Lead

Zn	Zn Error	S	S Error	Sn	Sn Error	Ni	Ni Error	V	V Error	Cd	Cd Error	Mn	Mn Error
91	12	< LOD : 465.85		< LOD : 15.31		289	34	275	56	< LOD : 14.66		1444	100
< LOD : 7.83		< LOD : 100.55		23	8	30	18	13	8	14	8	< LOD : 52.90	
< LOD : 7.64		< LOD : 91.16		41	9	< LOD : 26.24		< LOD : 9.90		21	8	< LOD : 51.18	
30	6	< LOD : 121.68		29	8	36	18	39	12	< LOD : 10.94		65	36
351	17	1909	330	49	9	74	23	105	22	33	9	520	65
16	6	329	82	28	8	< LOD : 26.26		< LOD : 10.84		18	8	83	36
42	7	885	135	36	8	48	19	47	12	18	8	135	40
18	6	263	92	20	8	41	18	20	10	15	8	< LOD : 53.23	
20	6	182	79	28	8	< LOD : 26.43		< LOD : 12.96		16	8	56	36
365	17	857	402	47	8	102	22	232	34	26	8	111	53

Zn - Zinc, S - Sulfur, Sn - Tin, Ni - Nickel, V - Vanadium, Cd - Cadmium, Mn - Manganese

Appendix 7- Results from the distance computation analysis carried out on the UAV-based and TLS 3d point cloud data using cloud to cloud comparison with 6 and 6 neighbouring points.

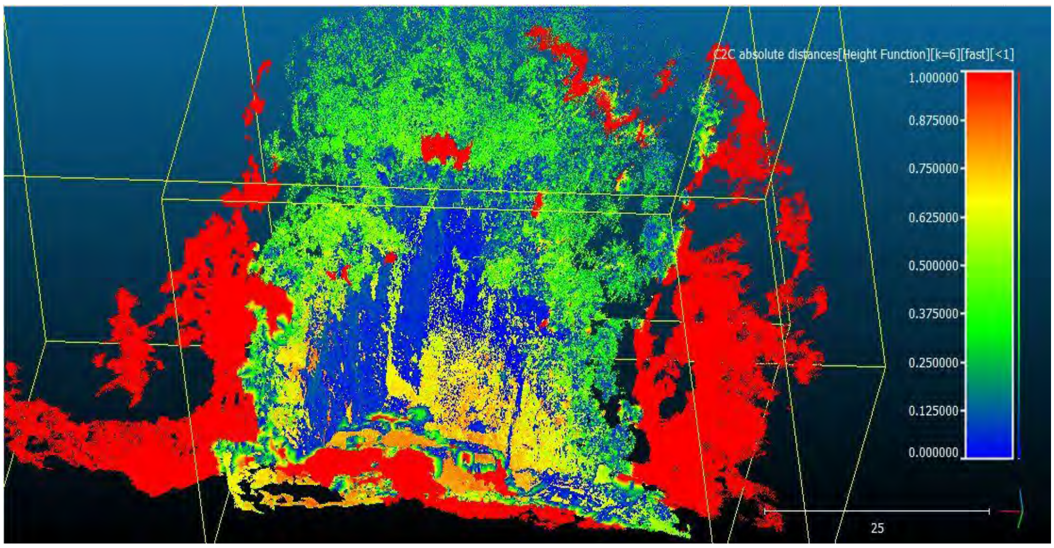

Figure 6-5: Cloud to cloud comparison of the UAV-based and TLS datasets using 6 neighbouring points. Shows the largest variation of the overlapped data at the vegetated areas of the UAV-based point cloud.

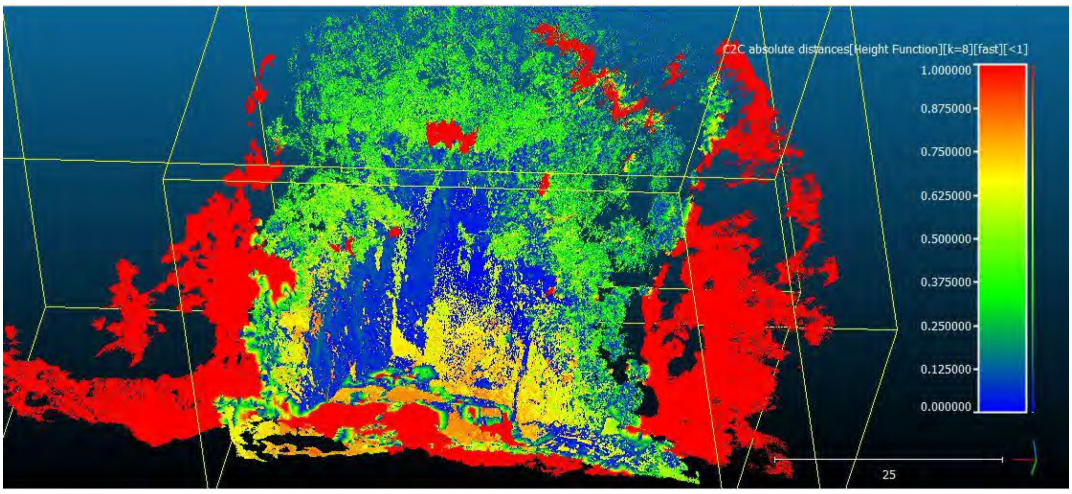

Figure 6-6: Cloud to cloud comparison of the UAV-based and TLS datasets using 8 neighbouring points. Shows the largest variation of the overlapped data at the vegetated areas of the UAV-based point cloud.

Appendix 8 - Thermal Data and Thermal processing results

The thermal imagery captured of the rock mass was analysed to be affected by the gradient in background of the camera, thus influencing the quality of the images. The thermal images were processed to remove the background by subtracting the dark count of the camera background from the thermal images.

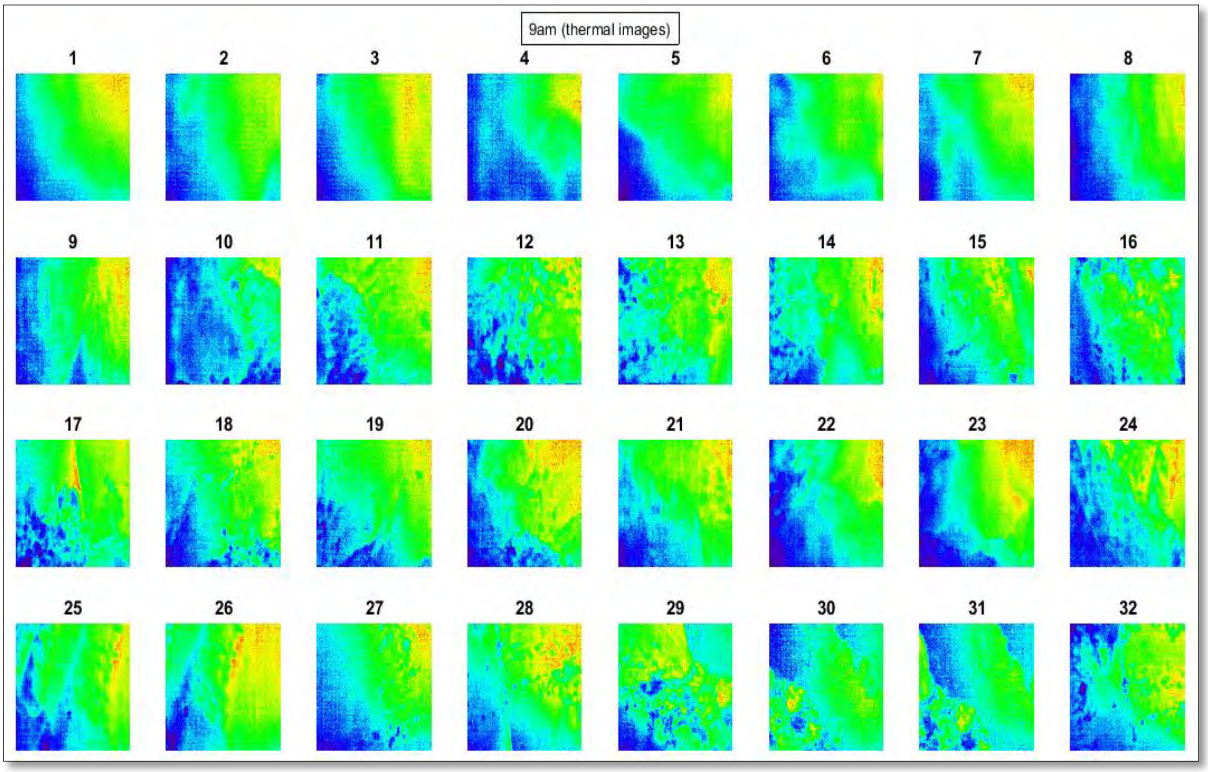

Figure 6-7: Stack of the thermal images of the Gildehaus slope captured at 9am (morning).

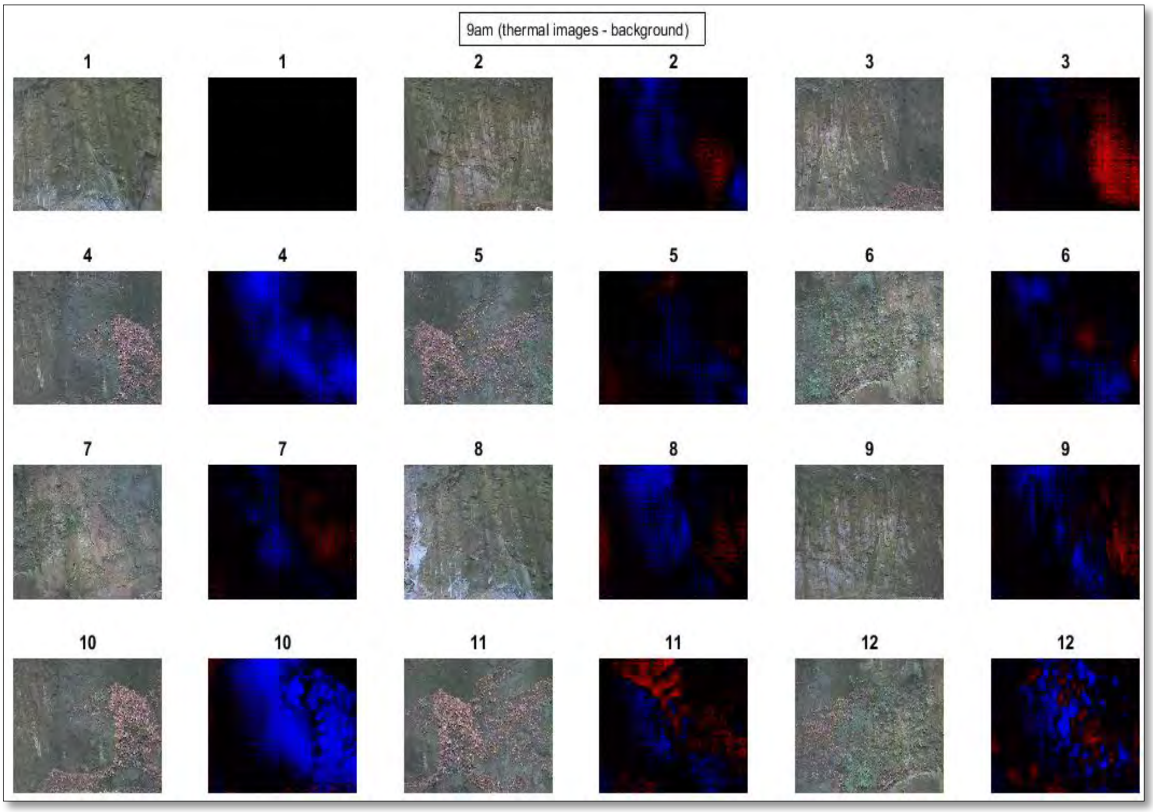

(a)

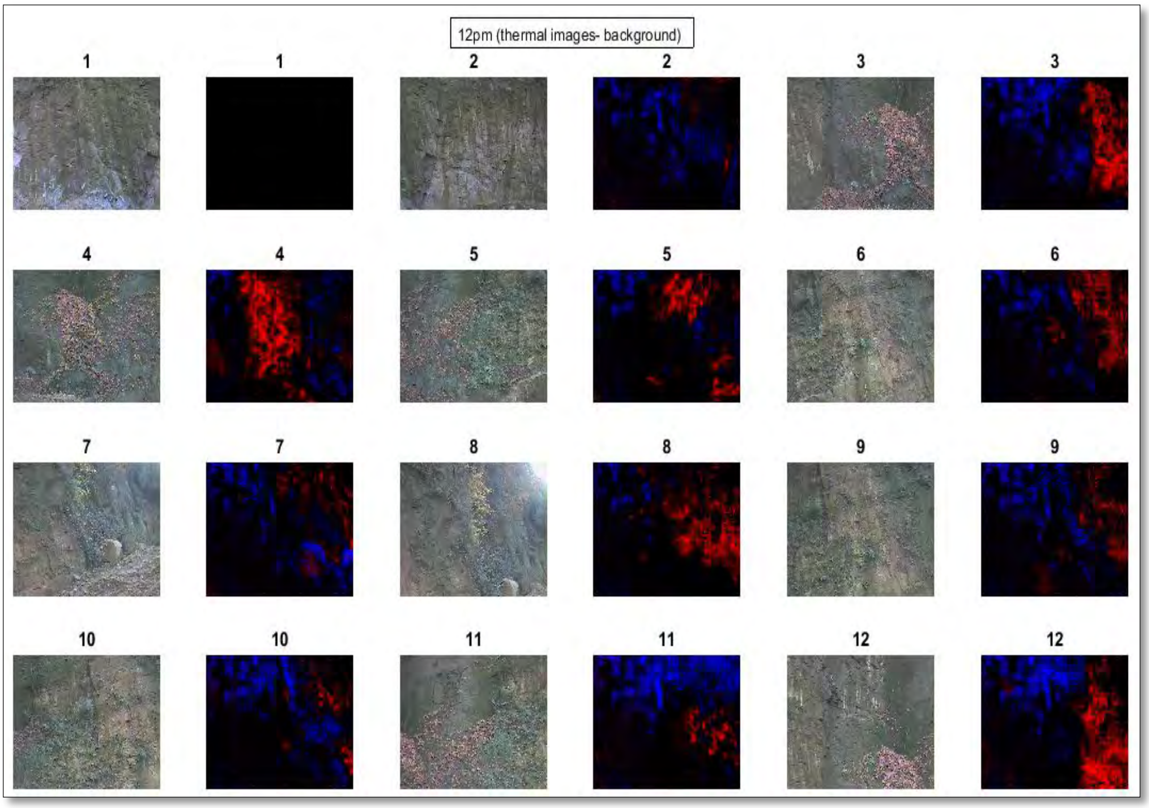

(b)

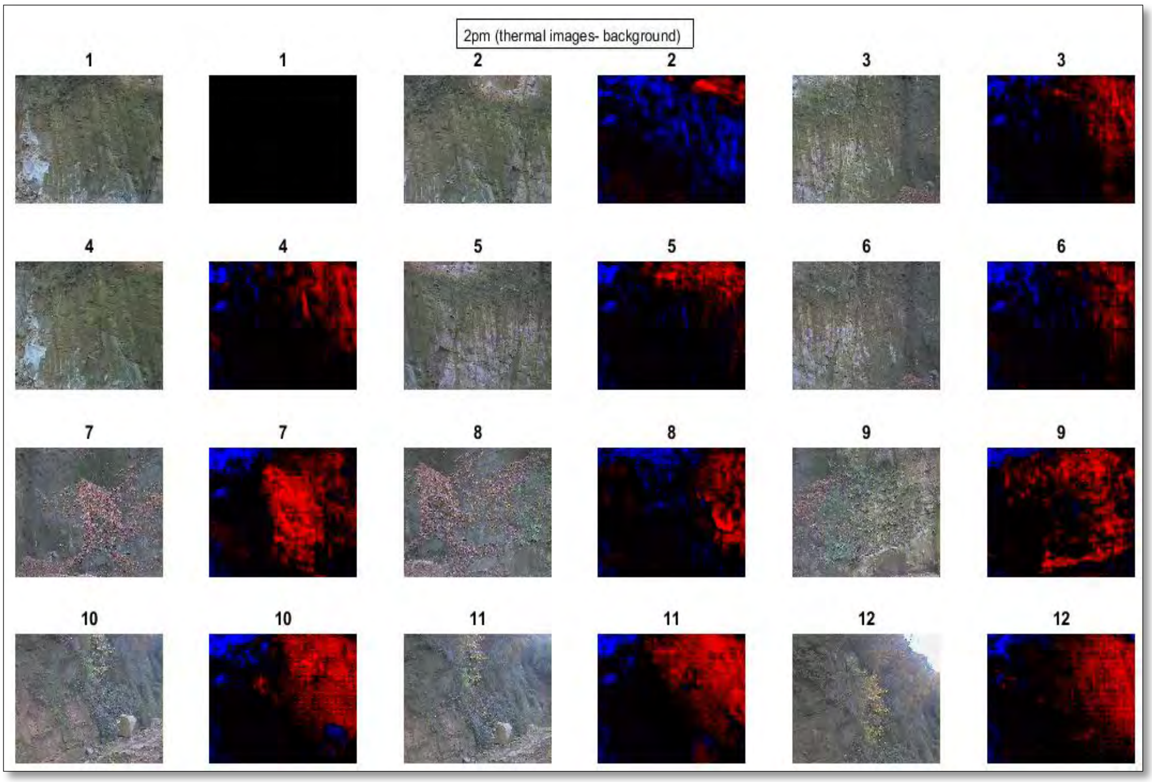

(c)

Figure 6-8: Stack of the thermal images of the Gildehaus slope minus the camera background effect. (a) shows the corrected stack of thermal images captured at 9am (morning), (b) shows the corrected stack of thermal images captured at 12pm (noon), (c) shows the corrected stack of thermal images captured at 2pm (afternoon).

Appendix 9 - The results from the RANSAC shape detection analysis carried out to detect the discontinuities in the rock mass.

The RANSAC algorithm applied to the UAV-based and TLS point cloud data was able to detect the direction of the bedding plane as well as the location and direction of the two joint systems observed on the rock mass during the geological field investigation.

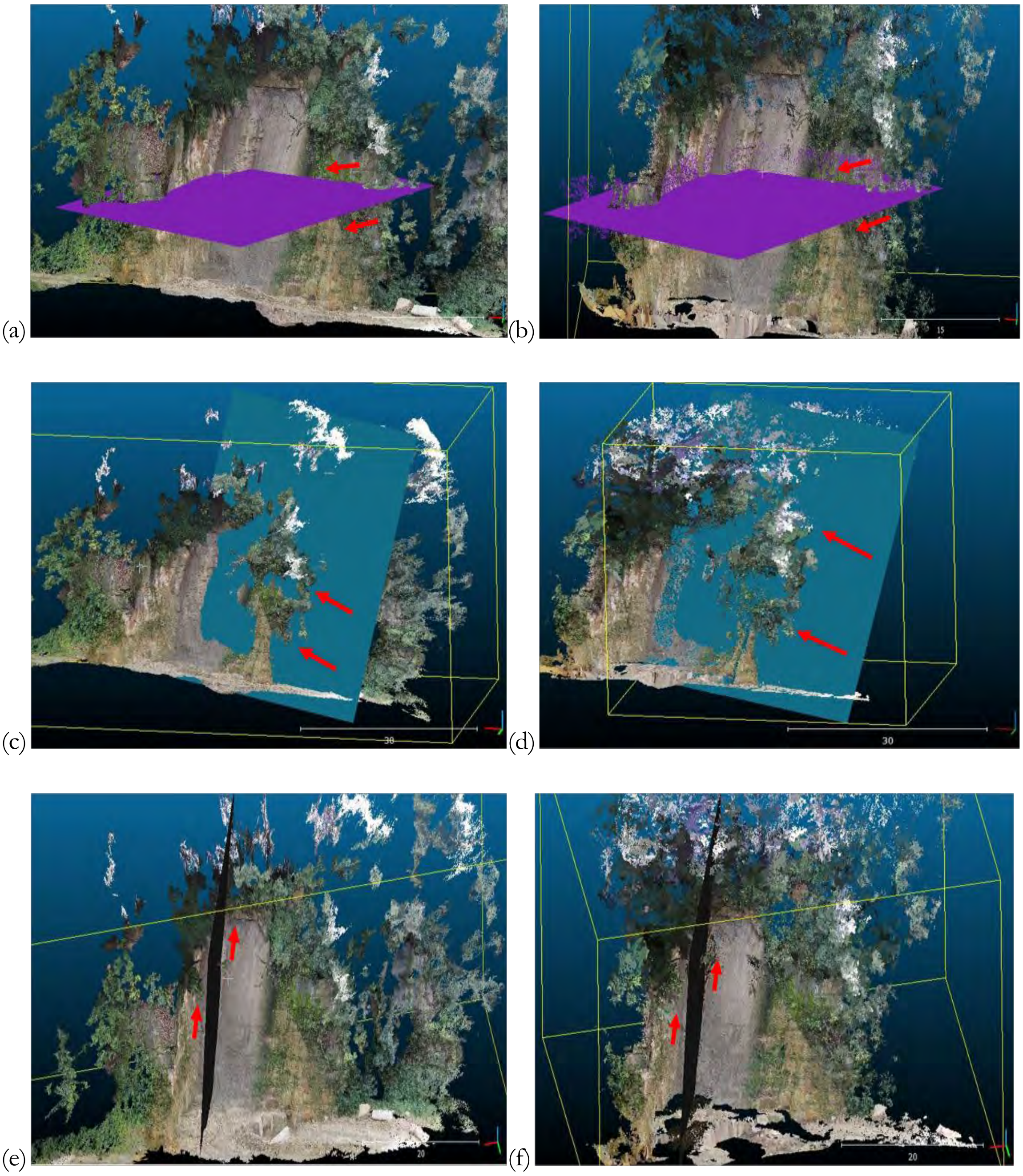

Figure 6-9: The detection of the discontinuities in the rock mass. (a) and (b) represents the bedding plane in the UAV-based and TLS 3D images respectively, (c) and (d) represents J-I while (e) and (f) represents J-II in the UAV-based and TLS 3D images respectively, the red arrow shows the direction of the discontinuity in the rock mass.

Appendix 10 - Results from the assessment analysis showing the percentage of points representing the regions covered by the weathering signatures in relation to the total point cloud of the rock mass.

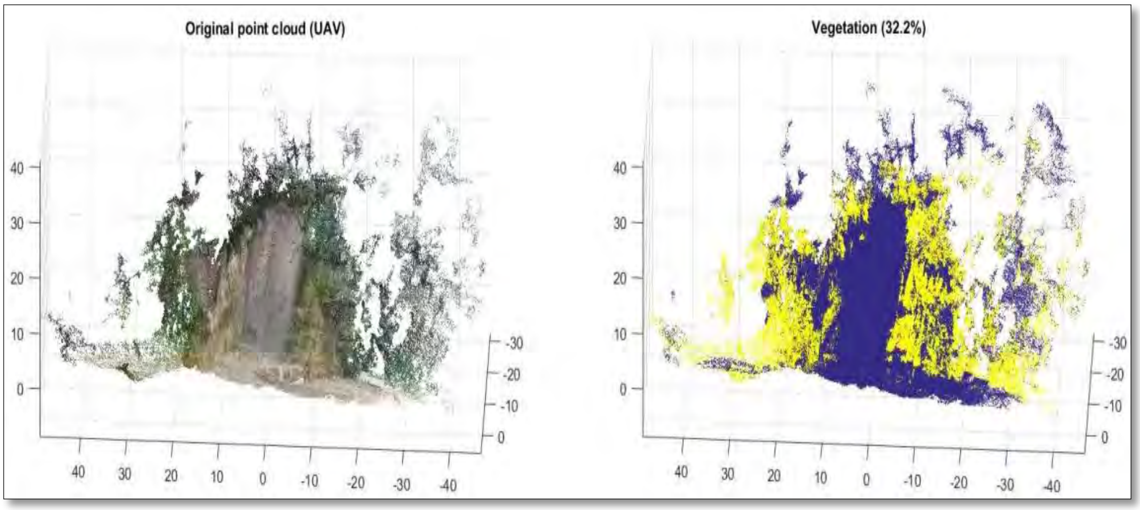

(a)

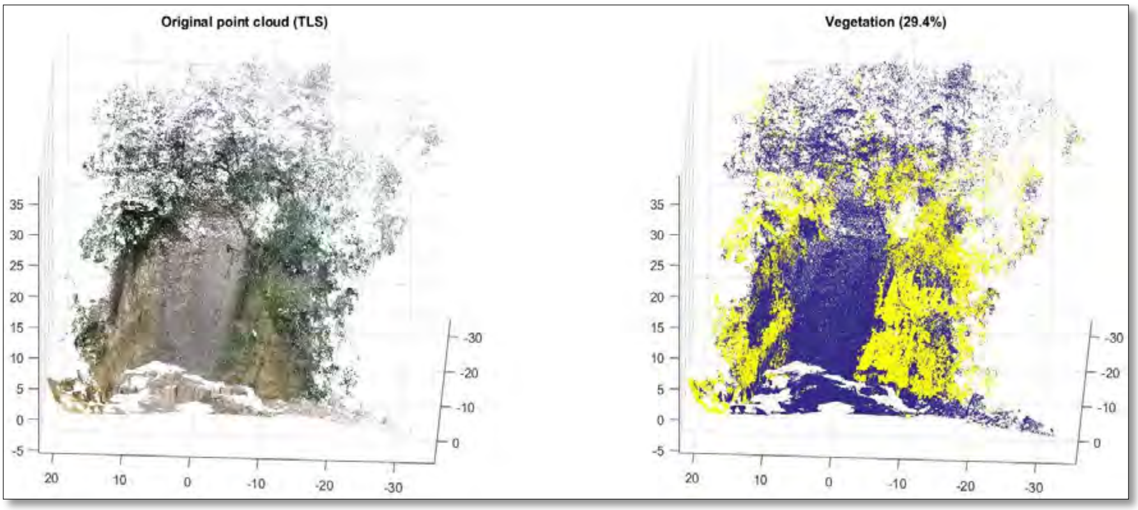

(b)

Figure 6-10: Assessment analysis shows that 32.2% of the points are covered by vegetation in the UAV-based 3D point cloud data(a), while (b) shows 29.4% of the points are covered by vegetation in the TLS 3D point cloud data.

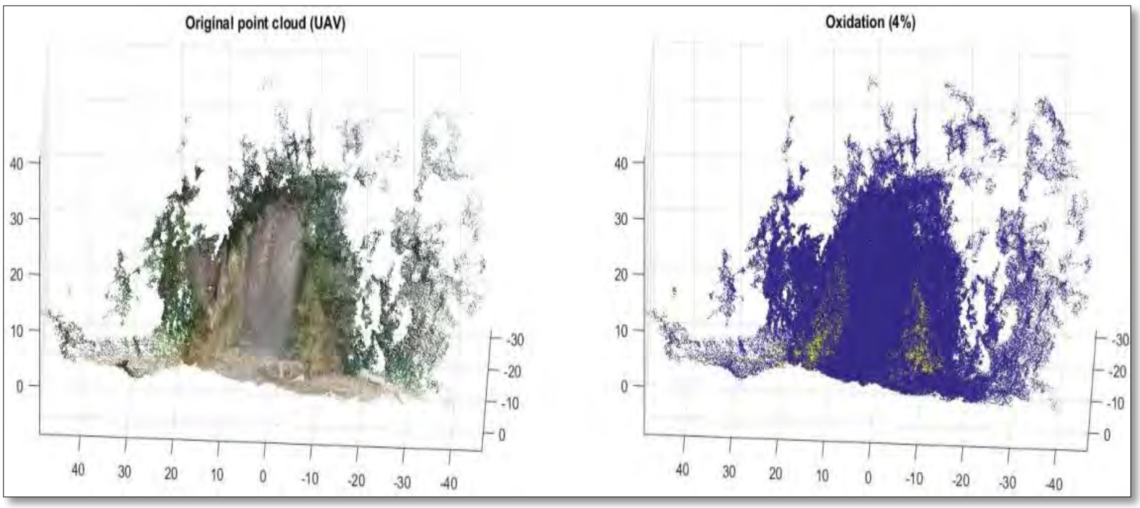

(c)

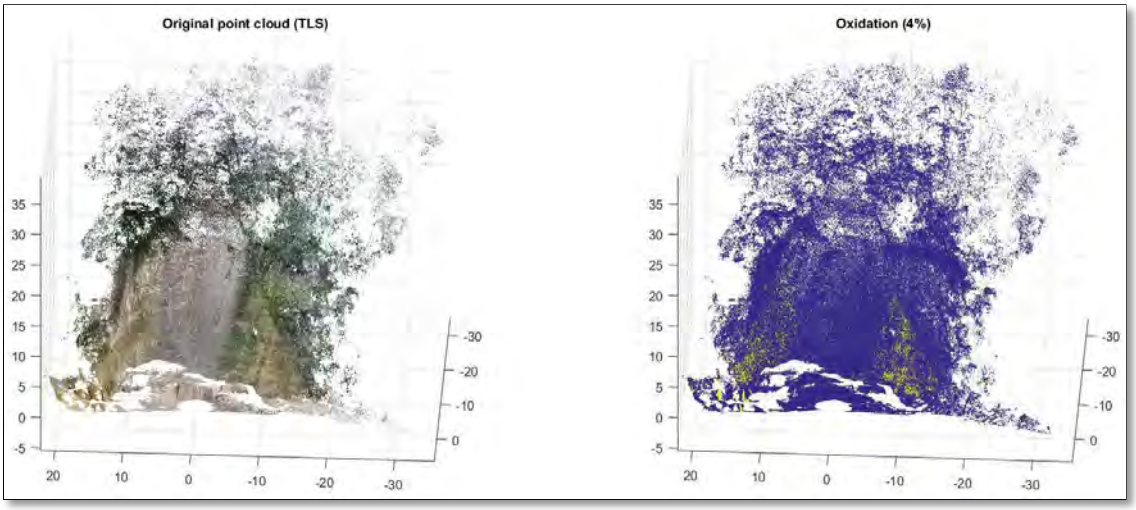

(d)

Figure 6-11: Assessment analysis shows that 4% of the points are covered by oxidation in the UAV-based 3D point cloud data(c), while (d) also shows that 4% of the points are covered by oxidation in the TLS 3D point cloud data.

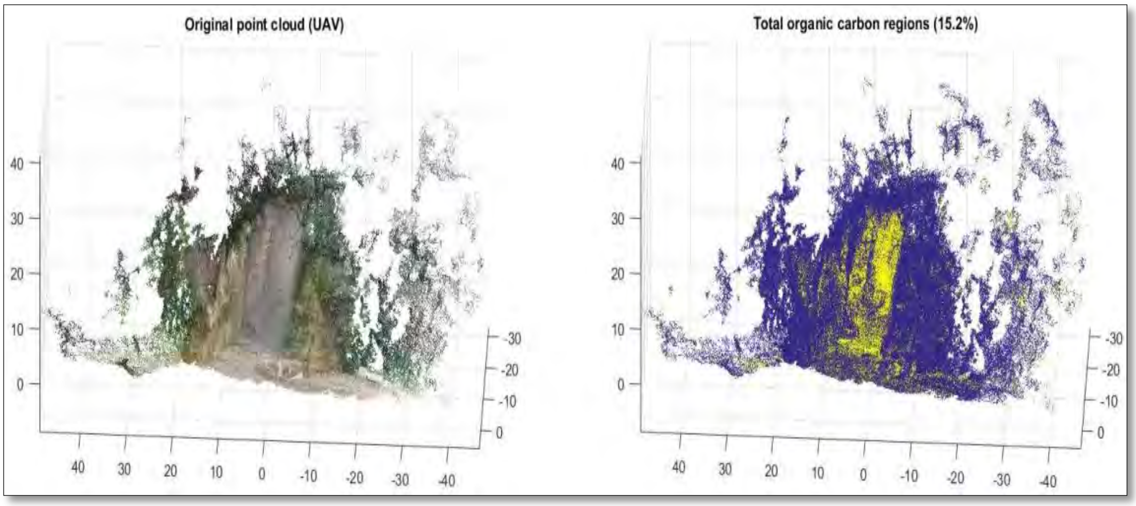

(e)

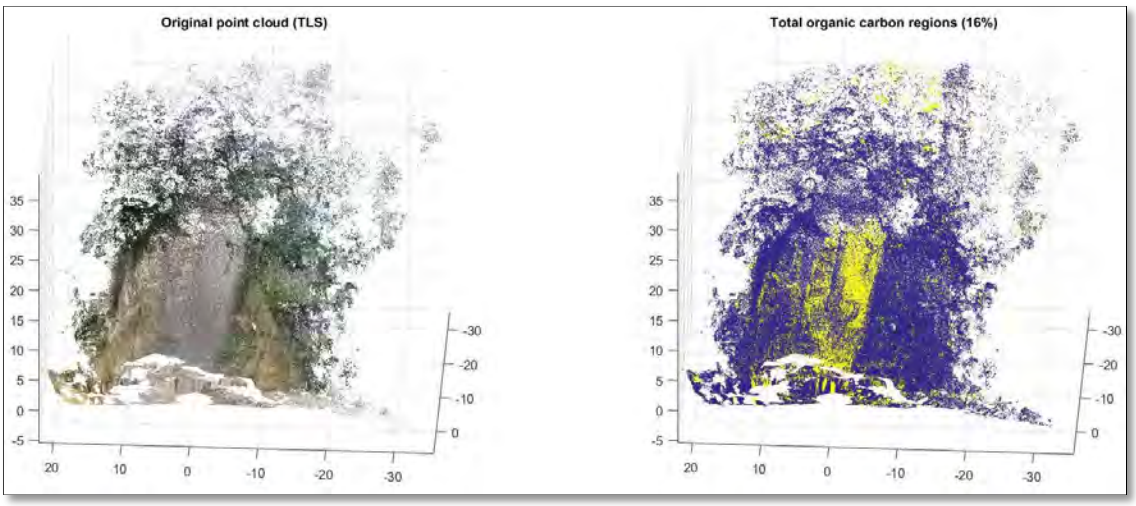

(f)

Figure 6-12: Assessment analysis shows that 15.2% of the points are covered by total organic carbon in the UAV-based 3D point cloud data(e), while (f) shows that 16% of the points are covered by total organic carbon in the TLS 3D point cloud data.

Appendix 11 - Results from the visual comparative analysis carried out using the thermal images and the UAV-based and TLS point cloud datasets.

The oxidized regions indicated by the pink arrows in Figure 6-13 radiated with higher thermal intensity that the vegetated regions indicated by the green arrows in the figure.

(a)

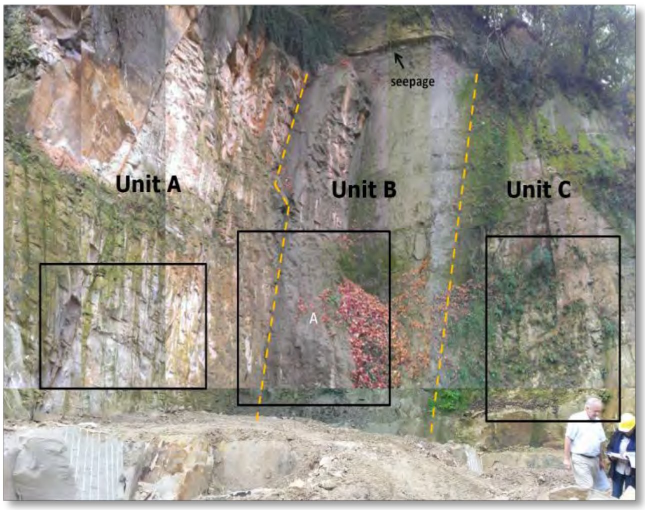

(b)

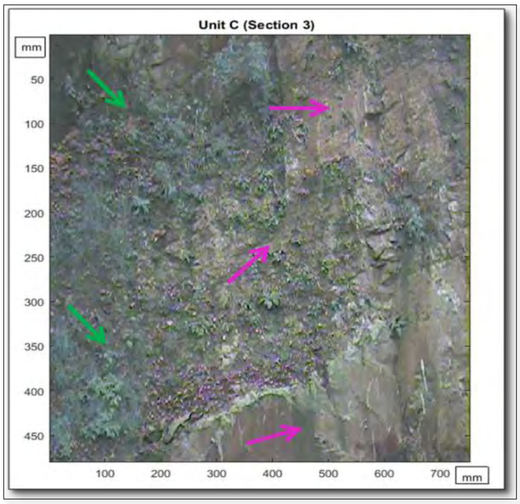

(c)

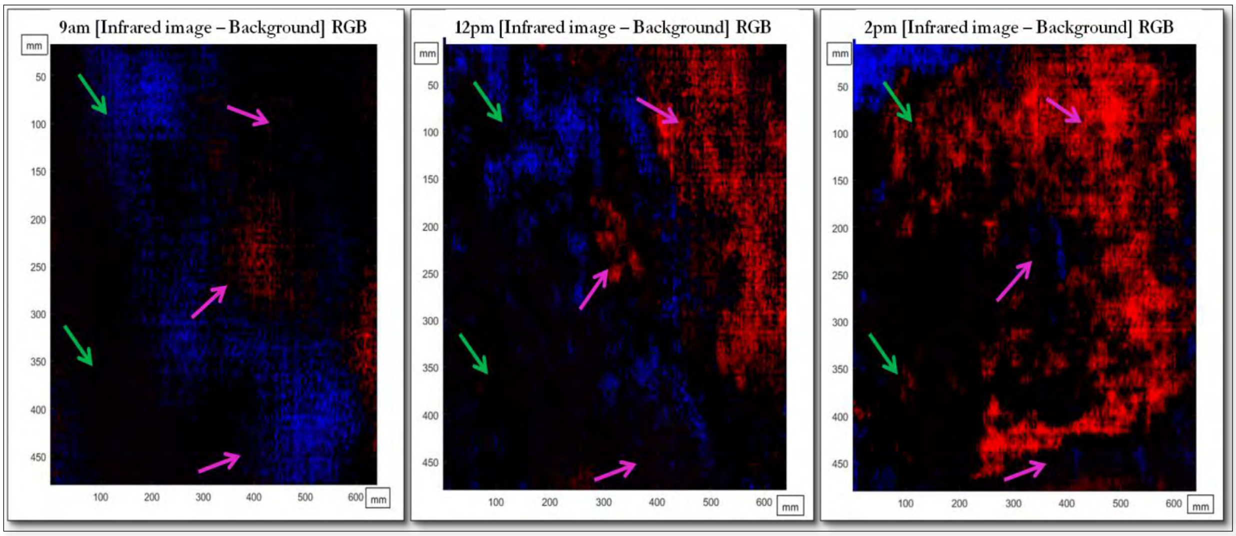

Figure 6-13: The visible and the thermal images of relatively the same location on the rock mass surface. (a) represents the Gildehaus slope highlighting the areas on the geotechnical units used for analysis, (b) shows the visible image of section (700x450mm) from unit C, while (c) shows the thermal images of section (600x450mm) from unit C captured in the morning at 9am, at noon by 12pm and in the afternoon at 2pm. The green arrows indicate the vegetated regions, while the pink arrows indicate the oxidized regions.

Appendix 12a - Results from the weathering signatures extracted from the segmented point clouds from each of the geotechnical units in the UAV-based and TLS point cloud datasets.

(a)

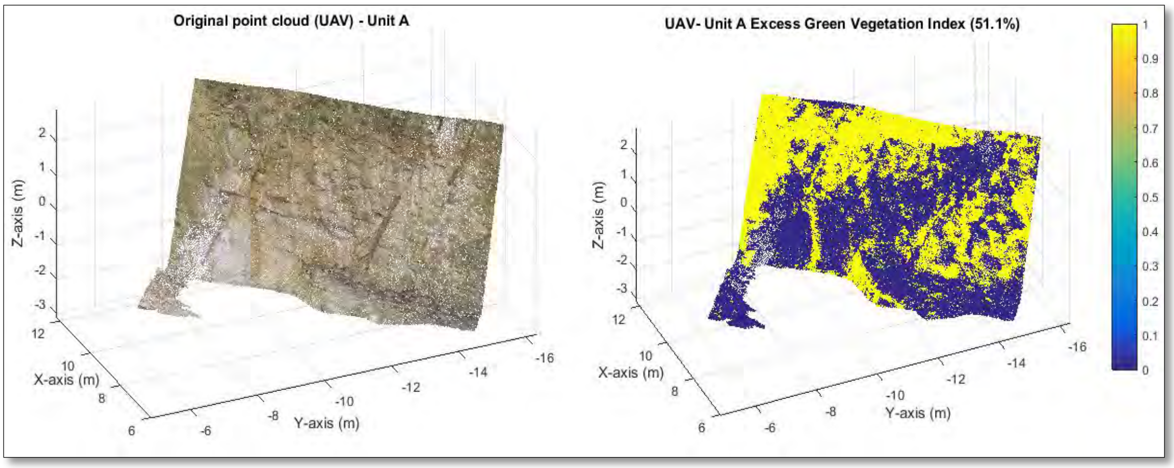

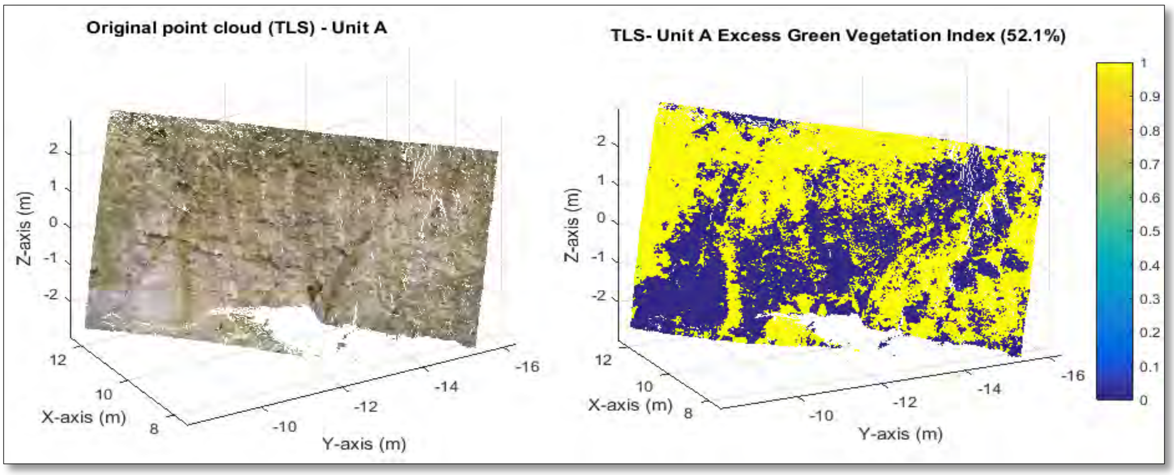

(b)

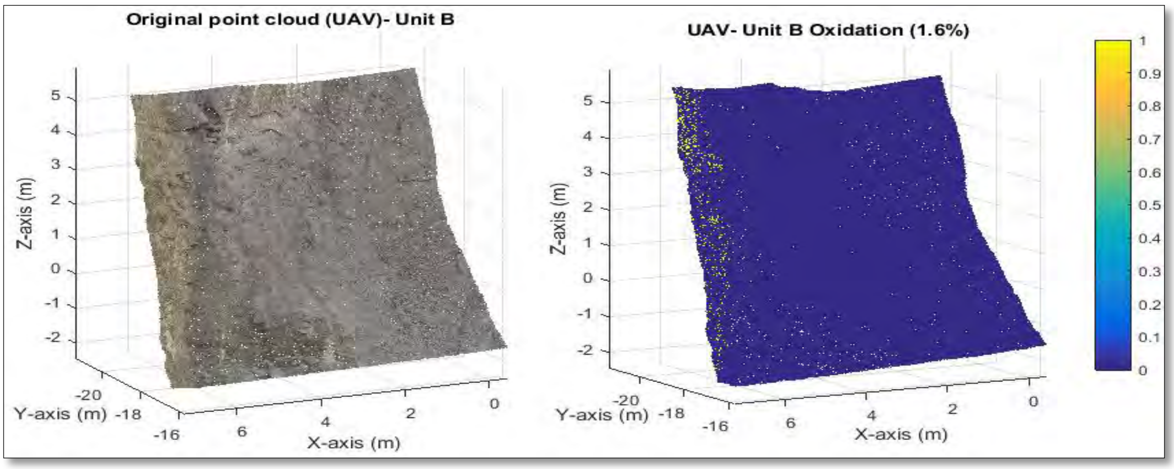

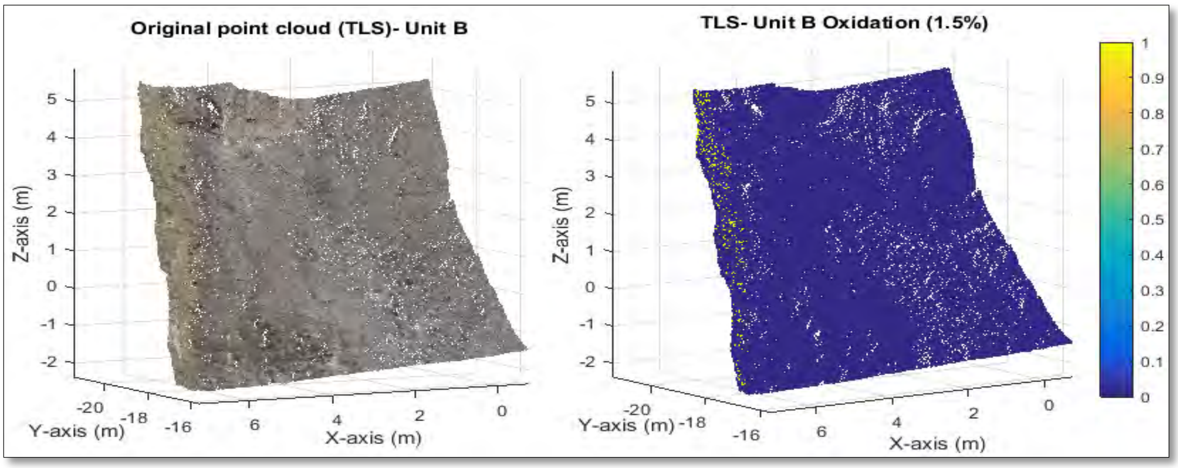

(c)

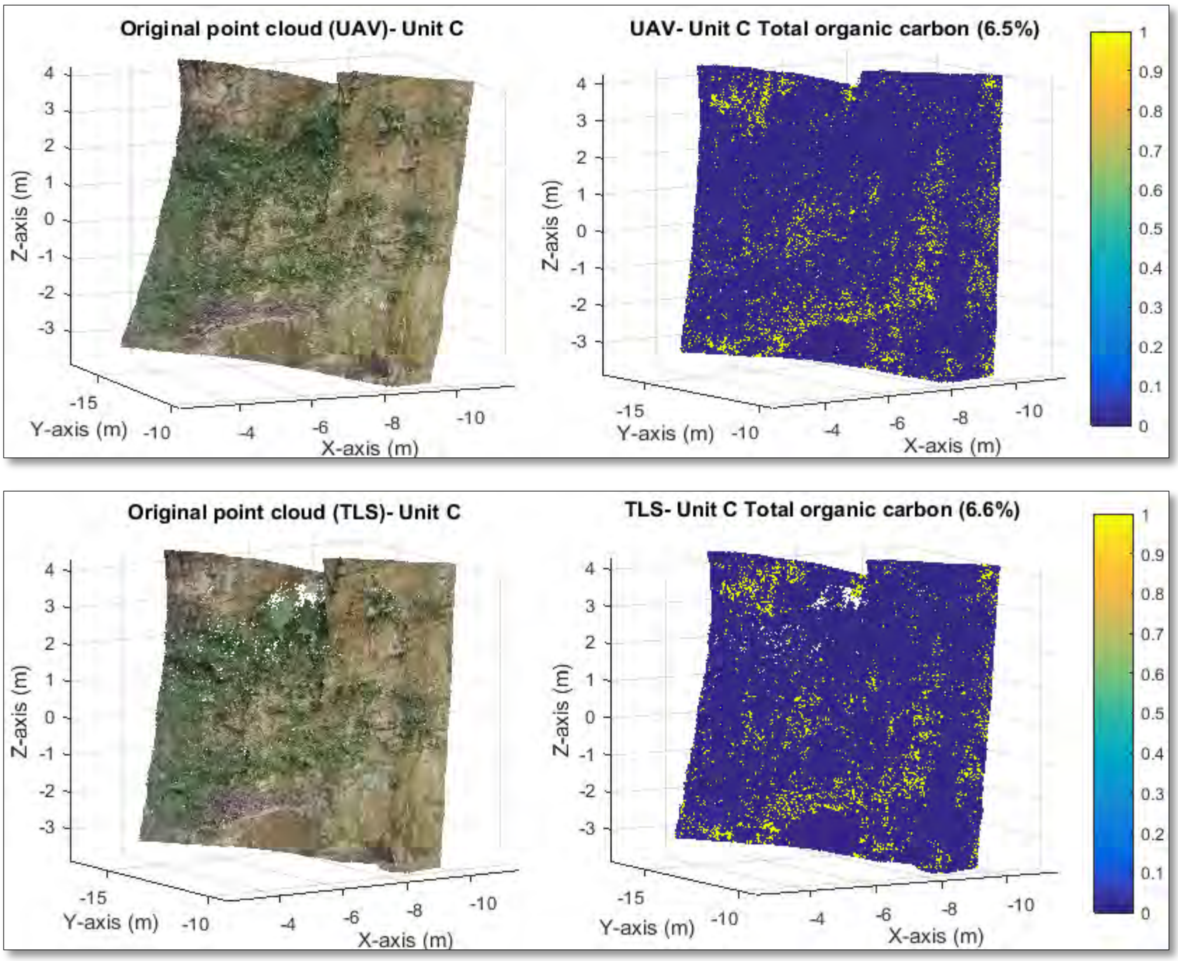

Figure 6-14: Results from the assessment analysis showing the percentage of points covered by the weathering signatures in the segmented point clouds from the UAV-based and TLS point cloud datasets acquired from each of the geotechnical units of the rock mass. (a) represents the segmented point clouds from unit A with the extracted vegetation and organic matter, (b) represents the segmented point clouds from unit B with the extracted oxidized regions while (c) represents the segmented point clouds from unit C with the extracted total organic carbon regions.

Appendix 12b - Results from the weathering signatures extracted from the segmented point clouds from each of the geotechnical units in the UAV-based and TLS point cloud datasets.

(a)

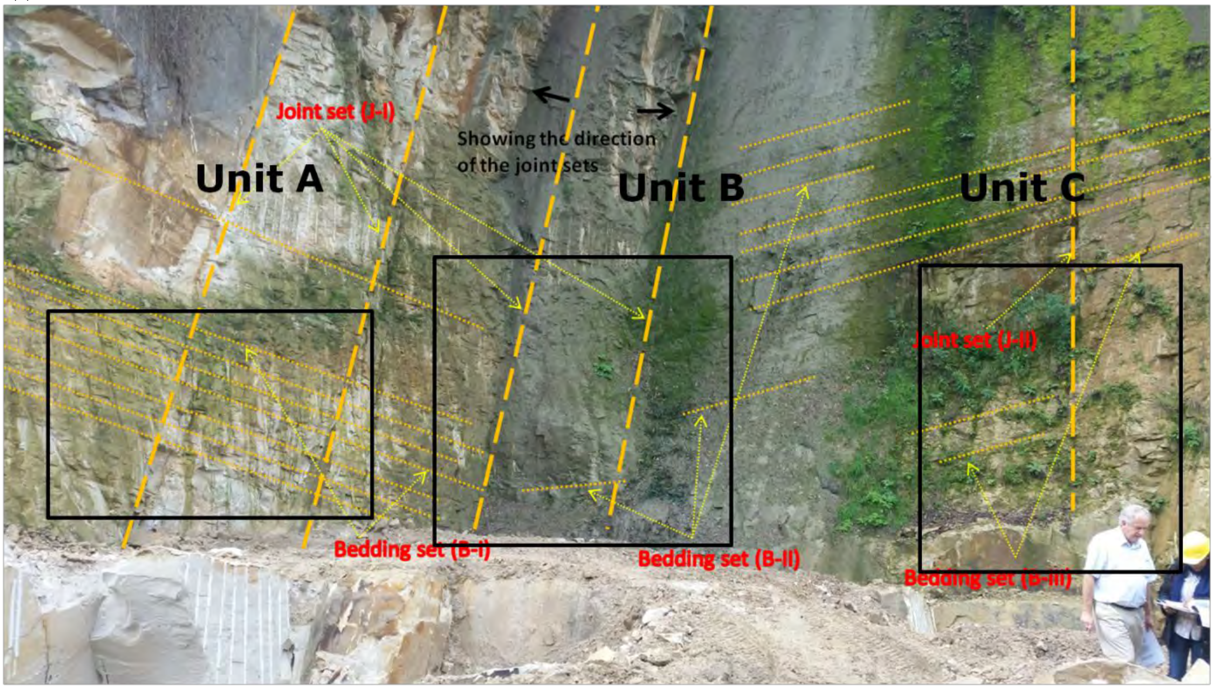

(b)

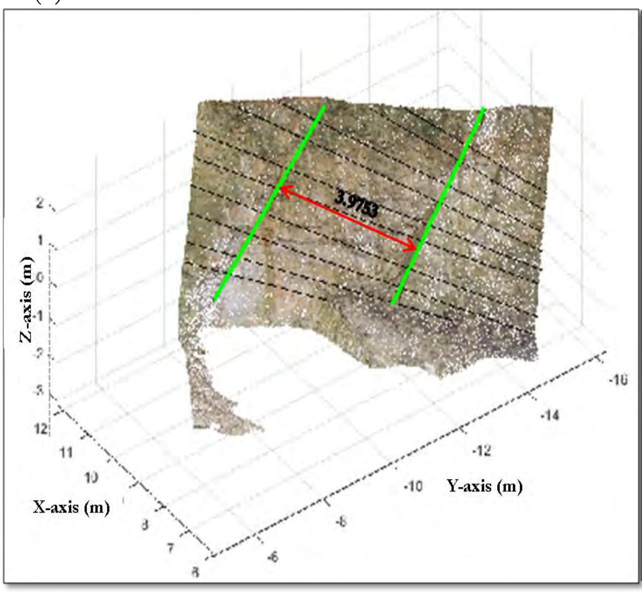

(c)

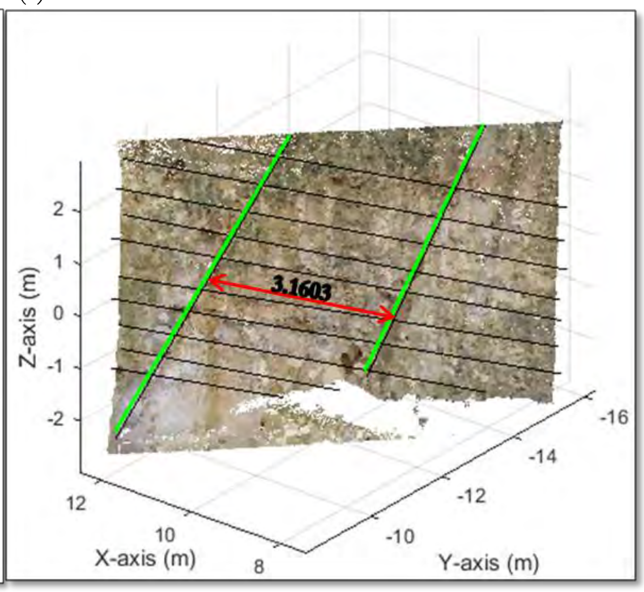

Figure 6-15: (a) shows the overview of the Gildehaus slope highlighting the positions of the discontinuities as observed from the geologic field investigation and also areas on the geotechnical units used for analysis, (b) shows the distance of 3.9753m between the delineated joint set in unit A for the UAV-based point cloud data while, (c) shows the distance of 3.1603m between the delineated joint set in unit A for the TLS point cloud data.